Charge and Energy Interactions between Nanoparticles and Low Pressure Plasmas

A DISSERTATION
SUBMITTED TO THE FACULTY OF THE GRADUATE SCHOOL
OF THE UNIVERSITY OF MINNESOTA
BY

Federico Galli

IN PARTIAL FULFILLMENT OF THE REQUIREMENTS
FOR THE DEGREE OF
DOCTOR OF PHILOSOPHY

Prof. Uwe R. Kortshagen, Adviser

May 2010

Acknowledgments

I would like to thank my adviser, Professor Uwe Kortshagen, for his guidance and mentoring during the years of my graduate career.

To my colleagues and friends in the HTPL group and at the University of Minnesota: thank you for five years of intellectual and personal enrichment.

To all the friends and people that I had the opportunity to meet here in Minnesota: you made me feel like at home.

Last but first in my heart: thank you family, for everything.

Abstract

In this work, the interactions between low-pressure plasmas and nanoparticles are studied with numerical models aimed at understanding the phenomena that affect the nanoparticles charge, charge distribution, heating, and crystallization dinamycs. At the same time other phenomena that affect the plasma properties resulting from the presence of nanoparticles are also studied: they include the power-coupling to the plasmas, the ion energy distribution and the electron energy distribution.

An analytical model predicting the nano-particle charge and temperature distributions in a low pressure plasma is developed. The model includes the effect of collisions between ions and neutrals in proximity of the particles. In agreement with experimental evidence for pressures of a few Torr a charge distribution that is less negative than the prediction from the collisionless orbital motion limited theory is obtained. Under similar plasma conditions an enhanced ion current to the particle is found. Ion-electron recombination at the particle surface, together with other particle heating and cooling mechanisms typical of silane-argon plasmas, is included in a particle heating model which predicts the nano-particle temperature. The effect of plasma parameters on the nano-particle temperature distribution is discussed and the predictive power of the model is demonstrated against experimental evidence of temperature induced crystallization of silicon nano-particles.

The power coupled to the plasma is measured together with the impedance nature

of the plasma, in the case of a pristine and dusty plasma. Nanoparticles are shown to strongly affect the electrical properties of the plasma, resulting in a much more resistive discharge.

A study of the ion energy distribution of ions impinging the sruface of nanoparticles is carried out and shows that ion-neutral collisions in proximity of the surface of the nanoparticle not only affects the particle charge but also the average energy of ions bombarding the particle surface.

Finally the presence of nanaparticle in the plasma and their ability to selectively interact with electrons in a specific energy range is studied to the extent of investigating the effects of the presence of particles on the electron energy distribution of electrons.

Contents

List of Figures

List of Tables

Chapter 1

Introduction

The main focus of this thesis is to study the interactions between low-pressure plasmas and nanoparticles. The objective of these studies is to improve the understanding of nanoparticle synthesis and control for the production of nanostructured materials. This introductory chapter provides an overview of the role of nanodusty plasmas in the growing field of nanotechnology, presents a brief background of the research leading to the current studies, and outlines and contextualizes the significance of the research presented in this thesis. A brief introduction to plasmas, low-pressure plasmas, low-pressure dusty plasmas and nanoparticle applications follows.

1.1 Plasma

Plasma was first identified in a Crookes tube, and so described by Sir William Crookes in a lecture delivered to the British Association for the Advancement of Science at Sheffield, Friday August 22 1879 (he called it "radiant matter"). The nature of the Crookes tube "cathode ray" matter was subsequently identified by British physicist Sir J.J. Thomson in 1897, and dubbed "plasma" by Irving Langmuir in 1928. Langmuir wrote: *"Except near the electrodes, where there are sheaths containing very few electrons, the ionized gas contains ions and electrons in about equal numbers so*

that the resultant space charge is very small. We shall use the name plasma to describe this region containing balanced charges of ions and electrons." [1].

A plasma is essentially a ionized gas. In its "pristine" form it comprises charged species of opposite signs (ions and electrons) as well as neutral species (gas atoms, molecules, radicals).

Plasmas are macroscopically charge-neutral, as even small imbalances of charge would lead to an electric field that would tend to re-establish said charge neutrality. Plasma physicists like to remember how more than 99% of all known matter in the universe is plasma. This is true yet naturally occurring plasmas on Earth are relatively rare. The most common example of "man-made" plasma is probably the fluorescent lamp. These lamps are essentially low-pressure gas discharges that use electricity to excite mercury vapors. The excited mercury atoms produce short-wave ultraviolet light that then causes a phosphor to fluoresce, producing visible light. [1]

The degree of ionization is an indication of what percentage of the species present are ionized: this property, together with temperature, pressure and thermodynamic equilibrium, is used to divide plasmas in different categories.

Temperature divides plasmas into thermal and non-thermal plasmas. Thermal plasmas have temperatures of the order of $10^4 K$, often feature thermodynamic equilibrium between different species and within each one (electrons, ions, neutrals), and are at moderate to atmospheric pressure. In non-thermal plasmas ions and neutrals tend to be at room temperature while electrons are at much larger temperatures ($\approx 10^4 K$). There is no thermodynamic equilibrium between species and electrons are not even in equilibrium with themselves. Electrons interact strongly with other electrons in the outer shells of atoms and molecules favouring processes of excitation and ionization and allowing chemical processes that require high activation energies to take place at room temperature.

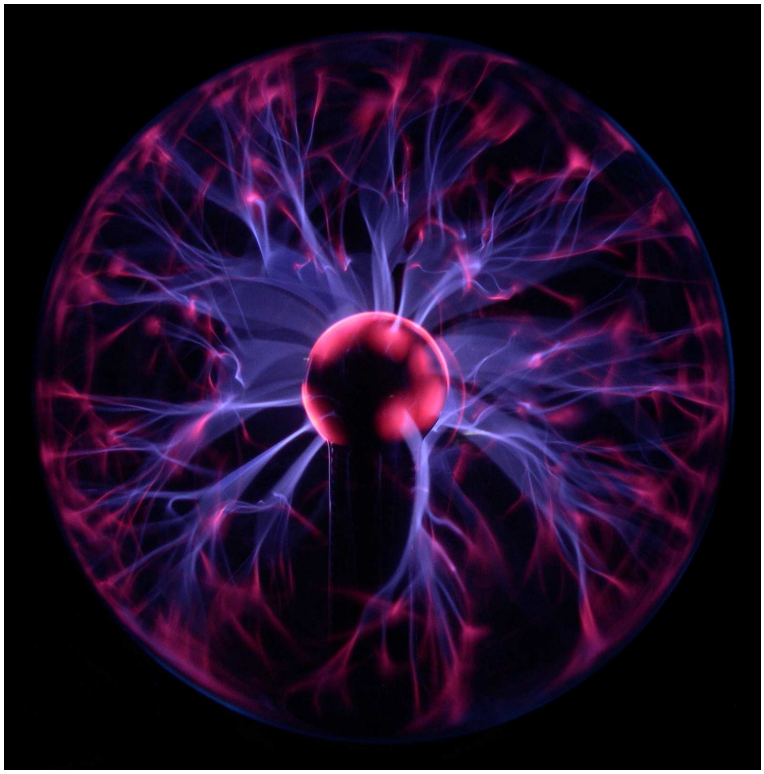

Figure 1.1: "Plasma lamp, illustrating some of the more complex phenomena of a plasma, including filamentation. The colors are a result of relaxation of electrons in excited states to lower energy states after they have recombined with ions. These processes emit light in a spectrum characteristic of the gas being excited." (Source: Wikipedia [1])

The symmetry in the charge and asymmetry in the mass and typical kinetic energy between electrons on one side and ions and neutral species on the other is the single most important feature of non-thermal plasmas as it allows for a number of potential applications at the expenses of an extraordinary complexity.

1.2 Dusty Plasmas

Nanometer to micrometer-size particles are often found in plasmas. Their origin depends on the type of plasma. Sometime they originate from the sputtering of the surfaces bounding the plasma. Other times they are the result of reactions taking place in the plasma. If the plasma precursors not only include inert gases (noble

gases) but also reactive gases, under certain conditions the production of particles is likely if not inevitable. Plasmas containing nanoparticles are often referred to as "dusty plasmas" or "nano-dusty plasmas".

Dusty plasmas are now the object of intense study because of their unique properties and complex physics. In non-thermal plasmas the more mobile electrons tend to be collected more efficiently by the nanoparticles suspended in the plasma than ions. As a result, nanoparticles carry on average a negative charge while in the discharge, a central concept for this thesis. Particles with unipolar (negative) charge establish a repulsive potential; as a result plasmas reduce the particles' agglomeration. Furthermore, dusty plasmas are a suitable medium for studying particle-particle interactions in a prescribed potential. A great deal of work has been done in this field, often using particles in the micrometer size for ease of visualization. The reader interested in this field is invited to read the seminal work of H. Thomas, J. Goree and G.E. Morfill "Plasma Crystal: Coulomb Crystallization in a Dusty Plasma"[5].

Dust particles are also present in astrophysical plasmas and have important effects in the formation of planets and other stellar objects. Saturn's rings for example can be considered astrophysical dusty plasmas [6].

1.3 Plasma synthesis of nanoparticles

Until recently, nanoparticles were only considered as a nuisance in plasmas, an unwanted contamination. They, in fact, continue to be a nuisance in many fields that make extensive use of plasma technologies. For semiconductor companies, for example, nanoparticles in plasmas are an enemy as their presence is detrimental to the quality and the functionality of the electronic devices being developed at a smaller and smaller characteristic size.

Avoiding wafer contamination by nanoparticles constituted the initial driving force for

a better understanding of particle nucleation, growth and transport in low-pressure, silane discharges. A large amount of research and experiments resulted from this, already in the early 90s. A very active group in this field is the group of Boufendi and Bouchoule in France [7, 8, 9, 10]. In the last two decades, however, the plasma community has learned to appreciate the unique properties of nanoparticles produced in low-temperature, low-pressure, non-equilibrium plasmas while, at the same time, semiconductor nanocrystals have raised attention for their potential applications including photovoltaic cells, light-emitting devices, thermoelectric energy generation and luminescent markers in biomedicine [11].

The plasma community discovered in non-thermal plasmas a series of advantages for the production of semiconductor nanocrystals that more traditional aerosol processes do not have [11]: the already mentioned unipolar (negative) charging of nanoparticles strongly reduces nanoparticles agglomeration and coalescence and favours the production of particles with a prescribed size with a very narrow size distribution; this is extremely important as the properties of semiconductor nanocrystals are strongly a function of their size. Furthermore, the ability of the highly mobile electrons to negatively charge surfaces in low-pressure plasmas extend to the surfaces bounding the plasma volume. The negatively charged nanoparticles are repelled by the strong electric fields in the regions in front of the negatively charged walls: nanoparticles are confined in the plasma reactor and diffusion losses to the walls are strongly reduced, improving the efficiency of the synthesis.

Another unique property of low-pressure plasmas and semiconductor nanocrystals interactions is the ability of these plasmas to efficiently transfer energy to the particles, contributing to their crystallization. Energetic surface reactions (electron-ion recombination and surface chemical reactions) are poorly compensated by cooling processes (conduction and radiation) that are relatively inefficient in low-pressure plasmas due

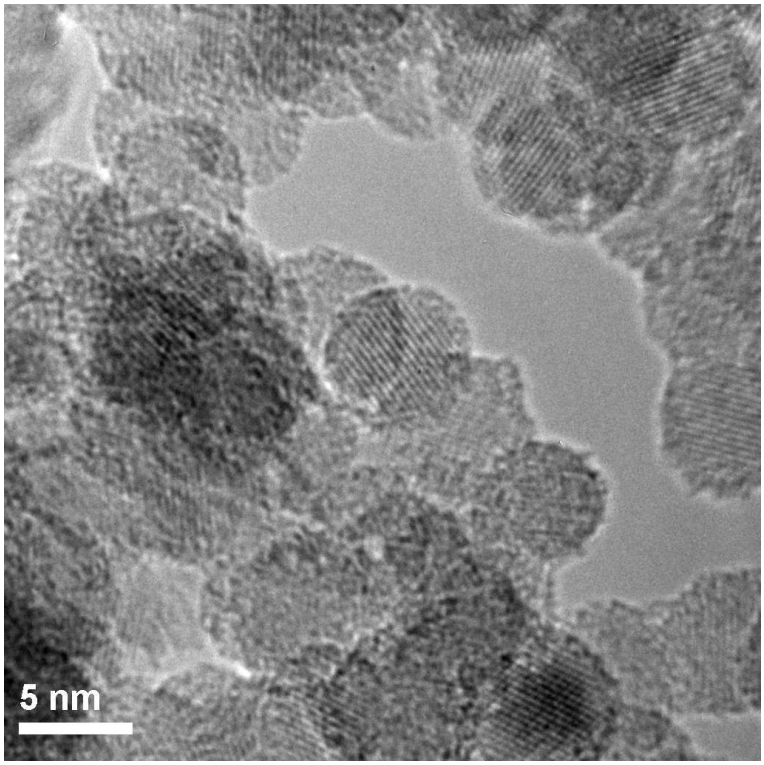

Figure 1.2: Silicon nanocrystals formed in a non-thermal flow-through plasma reactor with a residence time of 6 ms. [2]

to the small density of neutral atoms and the long time scale for radiation. As a result nanoparticles in non-thermal plasmas can be heated to temperatures that exceed the temperature of the surrounding gas by several hundreds of degree Kelvin [12, 13, 14, 15], allowing for the direct production of crystalline nanomaterials at room temperature (Figure 1.2). The crystalline microstructure of nanoparticles is indispensible for all of the novell applications of these materials, since amorphous particles suffer from a higher density of defects and charge carrier trap states, detrimental aspects for the electronic and optical properties of nanomaterials (Figure 1.3).

1.4 Application of plasma-produced nanocrystals

The scientific community discovered the potential for nanocrystals or "quantum dots" in the 1980s [16, 17] when it was realized that zero dimensional structures had more

potential optical properties than two dimensional quantum wells and one dimensional nanowires. Back then, semiconductor nanocrystals were usually synthesized in the liquid phase [18]. Low-pressure silane plasmas, however, are an excellent source of silicon nanoparticles: silane molecules are dissociated by electron impact collisions and increasingly large molecular clusters are formed within the plasma through a series of chemical reactions [19]. These clusters can grow to nanometers, then tens of nanometers in size, and can eventually achieve diameters on the macroscopic scale.

Applications for plasma-produced nanocrystals are still in a nascent stage as there have been, so far, only relatively few device demonstrations.

An early application of nanocrystalline silicon particles was to "seed" amorphous silicon films deposited by PECVD, then used for the production of solar cells. These "polymorphous" films improved without other treatment the solar cell efficiency [20] and represented an important step in the development of the dusty plasma field, because they were the first demonstrations that the nucleation of silicon particles in a silane discharge was not necessarily detrimental to device functionality. Kortshagen's group proved that crystalline nanoparticles embedded in an amorphous film can also act as seeds for successive crystallization of the film upon post-deposition annealing [21].

Other early applications of plasma-produced semiconductor nanocrystals were accomplished by Oda's group [22, 23, 24]. This group demonstrated the use of plasma-produced silicon nanocrystals in single-electron transistors, flash memory devices, and cold electron emitters. Emission efficiencies of up to 5% were shown for these devices. Kortshagen's group, in [25], demonstrated the functionality of a transistor based on cubic silicon nanocrystals. Silicon nanocubes of approximately 30 nm in size were deposited by impaction from a flow-through plasma reactor onto a substrate, for further processing. Typical transistor behaviour (drain-source current control by modulation

of the gate-source voltage) was successfully demonstrated.

Thermoelectric devices for the conversion of low-temperature thermal energy into electricity, are being actively investigates as methods to increase the efficiencies of thermodynamic cycles that discharge in atmosphere large quantity of "waste" energy. Nanostructured materials can play a major role in thermoelectric devices, since they have the potential for reaching high thermoelectric performances, by keeping a high electrical conductivity while limiting the thermal conductivity. In this field, silicon-germanium (SiGe) nano-compounds are good candidates for high-temperature ($> 600°C$) thermoelectric materials [26], and their production using plasma sources is being currently investigated.

Electricity production from photovoltaic conversion is an industry in strong expansion and large amounts of money are invested for research in this field. At the present time electricity produced by direct solar-to-electricity conversion is not, from a strictly economical sense, competitive with electricity produced from coal, oil, gas or nuclear sources. Nevertheless, as a result of governmental subsidized programs, the percentage of solar-produced electricity, particularly in Europe, is increasing. Semiconductor nanocrystals have potential for increasing the efficiencies in solar cells while, hopefully, reducing their manufacturing cost. The cost reduction often relies on depositing films of plasma-produced silicon nanocrystals using low-cost printing techniques prior to performing a final thermal annealing step. Other approaches aim at eliminating the need for post-treatment: proceeding in this direction Kortshagen's group recently built the first hybrid organic-inorganic solar cell based on an organic hole conductor, poly-3-hexylthiophene (P3HT) and electron-conducting plasma-produced silicon nanocrystals. While conversion efficiencies are still low ($\approx 1.2\%$) the manufacturability of these devices with only one vacuum step (the plasma synthesis of nanocrystals) has the potential for producing these devices at a very low cost.

Figure 1.3: Silicon nanoparticles can exhibit wavelength-tunable optical luminescence as a function of their size and can often be fabricated with narrow linewidths [3]. The luminescence is available only when the nanoparticle are crystalline. Crystallization in the plasma is a direct indication that particle experience intense heating mechanism while in the low-pressure plasmas.

Nanocrystals have also been intensely studied for their interesting optical properties [12] (see Figure 1.3 and caption therein).

Further details about the synthesis and applications of plasma-produced semiconductor nanoparticles can be found in the excellent review "Nonthermal plasma synthesis of semiconductor nanocrystals" given by Kortshagen in [11].

1.5 Motivation

In recent years, significant advances have been made on the experimental side of nanoparticle plasma synthesis and processing. Some applications of these nanoparticles have been shown, yet many fundamentals of particle behavior and plasma-particle interactions are still not well understood. A better understanding of the basic physical mechanism affecting the plasma-nanoparticle system would allow to achieve a better control over their production technique, their size, size distribution, morphology, and composition. It is time to develop a proper understanding of the physics of

a nanodusty plasma beyond the empirical needs of experiment design. This thesis is motivated by the need to improve the understanding of plasma-nanoparticles interactions to favour the development of current plasma-based nanoparticle technologies.

A deeper knowledge of the interactions between plasma and nanoparticles allows for a better understanding of the processes and mechanisms that result, in particular, in the formation of crystalline silicon nanoparticles.

The plasma-nanoparticles interactions investigated here are the ones that ultimately affect the resulting particle properties: the particles charge, their coagulation, the heating mechanisms the particles experience and the effects on their crystallinity, the energy with which ions bombard their surface while in the plasma and the effects on their surface morphology. Other interactions studied here have a more substantial effect on the plasma: the effect of nanoparticles on the power coupled to a radio-frequency capacitively-coupled plasma reactor and the effects of particles on the electron energy distribution in low-pressure dusty plasmas.

1.6 Structure of the thesis

The layout of this thesis is as follows: following this introduction, Chapter 2 gives the reader a brief background over the main concepts necessary to understand the content of the thesis, as well as a brief overview of the research done by other groups regarding particles charging, heating, coagulation, nanoparticle effects on plasma power coupling, and about the effect of nanoparticles on ion and electron energy distribution functions in low-pressure plasmas.

Chapter 3 covers the topics of particle charging, charge distributions, particle heating and coagulation, together with the effects that ion-neutral charge exchange collisions have on these.

Next, Chapter 4 supports with some experimental evidence the findings of Chapter 3 by showing how the crystallinity of the nanoparticles is controllable by the plasma properties.

Chapter 5 covers the topic of the effects of charge-exchange collisions on the shape of the energy distribution function for ions bombarding the surface of the nanoparticles.

Chapter 6 presents the results of the measurement of electrical properties of a nano-dusty radio-frequency plasma reactor including measurements of power and impedance.

Chapter 7 presents the results of a self-consistent kinetic model for the effect of nanoparticles on the energy distribution function of electrons in low-pressure argon plasmas.

A summary of the presented work and suggestions for future work is given in Chapter 8. A list of References conclude the thesis.

Chapter 2

Background

This chapter gives the reader a background of the main concepts necessary to understand the content of the thesis, and a brief overview of the research done by other groups regarding particle charging. An introduction about nanoparticle effects on plasma power coupling, and about the effect of nanoparticles on ion and electron energy distribution functions in low-pressure plasmas is also provided.

2.1 Background on particle charging

One of the most important parameters determining the properties of a dusty plasma is the charge of the dust particles. Because of this, in the last two decades great attention was devoted to develop models that would predict the charge carried by particles in an ionized environment over a wide range of operating conditions. One of the best known and widely used model is the orbital motion limited (OML) model. This model is able to estimate with good accuracy, in a very simple way, the potential of a sphere or an infinite cylinder immersed in a plasma in the absence of collisions in proximity of the body. Through the knowledge of the potential, it is possible to estimate the charge carried by a sphere with a simple assumption on the capacity of a sphere in vacuum. Because of the higher mobility of electrons, the collision rate of electrons with neutral

nanoparticles is higher than that of ions. As the nanoparticle gets charged negatively the ion current to its surface increases and the electron current decreases. Therefore, a nanoparticle in a plasma tends to acquire a staedy state negative charge such that ion and electron currents become equal. However, if the nanoparticle is very small, the charge can fluctuate between negative, neutral, and positive due to the discrete nature of charging. This can have a significant impact on particle growth due to an increase in coagulation between oppositely charged nanoparticles.

The maximum charge on a nanoparticle can also be limited by its size because of the repulsion between the electrons on the surface of the nanoparticle. This limit is based on the stability of the electrons in the nanoparticle from tunneling out [27].

Secondary electron emission (SEE) and UV photodetachment (UVPD) are also mechanisms that can affect nanoparticle charging in a plasma [4]. Both SEE and UVPD tend to make a nanoparticle less negatively charged by favouring electron emission from its surface: when energetic ions collide with the discharge electrodes, secondary electrons are emitted and accelerated towards the bulk region by the electric field in the sheath. As these high-energy electrons collide with a nanoparticle they favour the release of electrons from the nanoparticle and decrease the negative charge on the nanoparticle; In UVPD, photons from UV radiation in a plasma can detach electrons from a nanoparticle. Under typical laboratory plasma conditions, however, UV electron photodetachment and secondary electron emission do not have a significant impact on the behavior of nanoparticles in a plasma, and they will not be further considered in this work.

Charging of nanoparticles plays also an important role in the growth, coagulation, and transport of nanoparticles in a plasma and the overall plasma-nanoparticle system behavior [28, 29, 30, 31].

Within the OML framework, the ion current to a negatively charged particle is de-

scribed under the assumption of completely collisionless ion motion and accounting for that only the fraction of ions whose angular momentum, referenced to the particle, is below a certain threshold will be collected [32, 33].

If a particle of radius R_p carries a charge $Z_k = k \times e$ (where $e = 1.602 \times 10^{-19}\ C$ is the elementary charge of an electron in Coulomb and k is a $\pm$ integer number of elementary charges carried), then the potential at the surface of such particle is:

$$V_p = \frac{Z_k}{4\pi\epsilon_0 R_p} \tag{2.1}$$

where $\epsilon_0 = 8.85 \times 10^{-12}\ Fm^{-1}$ is the vacuum dielectric constant. This potential is usually negative because the charge carried by the particle is usually negative. The OML theory evaluates the charge/potential of a sphere by developing equations for the current fluxes to the object for both electrons and ions. In a steady state regime these two contributions need to be equal to avoid a drift of the charge with time. From the dependence of the current expressions on the object potential, the latter is found by the solution of a non-linear equation. For a spherical particle the appropriate equations are:

$$\begin{cases} \nu_i = \frac{1}{4}\ \left(4\pi R_p^2\right)\ n_i\sqrt{\frac{8kT_i}{\pi m_i}}\ \left(1 - \frac{eV_p}{k_B T_i}\right) \\ \\ \nu_e = \frac{1}{4}\ \left(4\pi R_p^2\right)\ n_e\sqrt{\frac{8kT_e}{\pi m_e}}\ \exp\left(\frac{eV_p}{k_B T_e}\right) \\ \\ \frac{dZ_k}{dt} = e(\nu_e - \nu_i) = 0 \rightarrow V_p = V_p(\nu_i = \nu_e) \end{cases} \tag{2.2}$$

where ν_i is the ion charging frequency, ν_e is the electron charging frequency, n_i is the unperturbed ion density, n_e is the unperturbed electron density, T_i is the ion temperature, T_e is the electron temperature, m_i is the ion mass, m_e is the electron mass, and k_b is the Boltzmann's constant. Strong assumptions for the OML theory are the fact that the plasma properties are unperturbed far away from the surface, the

sheath is collisionless and that the object size is small compared to the characteristic plasma length itself. Overall, in order to apply OML theory the following needs to be true:

$$\lambda_{mfp} >> \lambda_{LD} >> R_p \tag{2.3}$$

where λ_{mfp} is the electron/ion mean free path between collisions, λ_{LD} is the linearized Debye length, and R_p is the particle radius. The linearized Debye length is defined as follows:

$$\frac{1}{\lambda_{DL}^2} = \frac{1}{\lambda_{De}^2} + \frac{1}{\lambda_{Di}^2} \tag{2.4}$$

(where:

$$\lambda_{De} = \sqrt{\frac{\epsilon_0 k_B T_e}{e^2 n_e}}; \lambda_{Di} = \sqrt{\frac{\epsilon_0 k_B T_i}{e^2 n_i}} \tag{2.5}$$

are respectively the electron and the ion Debye lengths) and essentially represents a characteristic plasma length scale over which spontaneous deviation from quasineutrality and an effective non-zero charge density are possible. The collisionless assumption for the OML relies on the fact that there are no collisons over such a length scale.

OML expressions are derived, other than from the assumptions stated above, mainly from the conservation of angular momentum in central force fields. Details about the potential around the sphere are not required other than spherical symmetry and the absence of extrema in the potential between the surface and the unperturbed region of the plasma. Its wide use is due to the fact that in its development, as well as for its application to a real case, the details of the shape of the potential are not necessary.

It is important to stress that one of the assumptions that is made for the development of OML theory, *the non-collisionality within the sheath*, is seldom true in common practice and causes the OML theory to underestimate the ion currents and overestimate the amount of charge on the particle.

Furthermore, in OML theory the floating potential of an object immersed in a plasma is a function only of the ratios of the masses and temperatures of ions and electrons, regardless of particle size or pressure, while there is some experimental evidence for a dependence of the floating potential on those parameters[34]. From these observations arose the need to develop models that could account for collisions of ions in proximity of the particle surface and the effect that these have on current and charge to the particle.

In 1959 Bernstein and Rabinowitz [32] realized that ion-neutral collisions in proximity of a Langmuir probe could cause the formation of a cloud of trapped ions revolving in close orbits. This could affect the current to the probe because of the influence it can have on the space potential near the probe.

In 1992, Goree [34] pointed out that charged dust grains in a plasma can trap positive ions in confined orbits, shielding the grain from external electromagnetic fields. The number of the trapped ions was determined by a balance between collisional trapping and detrapping. The method developed involved the use of a Monte Carlo simulation without a self-consistent potential. Goree found that ion trapping can be very significant in laboratory plasmas but negligible in space plasmas.

In 1996, Schweigert and Schweigert [35] used a charging model based on OML theory to describe the influence of particle charging on the coagulation of particles. They found coagulation rates of particles that were signicantly slower than those observed in Bouchoule and Boufendi's experiments [8], casting doubts on the validity of OML theory.

In 2000, Zobnin [36] performed a self-consistent molecular-dynamics calculation of the currents to a particle in presence of ion-neutral collisions. The computational results showed that the potential of a particle depends *non-monotonically* on the pressure and it was also observed that the surface potential is not independent of

the particle size as predicted by the OML theory. Zobnin's contribution is to realize the non-monotonicity of the effect of pressure and that ion-neutrals collisions start to affect the potential of small particles already at pressures of tens of Pa, which correspond to ion mean free paths still much larger than the Debye radius. Also Zobnin's simulations reveal a minimum in the particle surface potential for pressures of 100 Pa in a Neon plasma.

In 2001, analytical work by Lampe and co-workers [37] proved the intuition of Bernstein and Rabinowitz that ion charge-exchange collisions lead to the buildup of trapped ions which dominate the shielding around the particle, even when the mean free path is much larger than the Debye length. In their model, the ion-neutral collision frequency is not energy dependent, which is a simplication motivated only by the fact that otherwise an analytical model would not be possible. Extending this result in 2003, the same group [38] gave a self-consistent analytical model of the ion and electron currents to a particle, as well as the potential and charge carried. Their predicted current is *monotonically* increasing as a function of background pressure, and they include in the model a "probability" of performing a collision within the sheath, r/λ_{mfp}, that is not strictly a probability as it is not derived from gas kinetic theory and can have values larger than 1.

In 2004 an international collaboration between Zobnin's and Morfill's group [39] produced experimental results that in fact demonstrated the *non-monotonic* dependence of charge and current on pressure and particle size. The experimental evidence of the trend is sound but quantitatively the results are strongly affected by the fact that the plasma properties (densities and temperatures) were measured in the absence of particles. It is very complex to measure electron temperature and electron density locally in a dusty plasma because traditional techniques such as Langmuir probes suffer from the effect of particle contamination of the probe tip, making the results

of the measurement unreliable.

The same group in 2005 published a paper [40], following the 2004 letter, in which they reported the results of the experimental measurements together with the molecular-dynamics simulation and an analytical model. Once again, while both experiments and simulations gave a *non-monotonic* behavior for the ion current with pressure, the analytical model predicted a *monotonical* increase with pressure.

In 2006 Morfill published a study [41] about the charge on a dust grain in collisional plasmas where he considered the possibility of collisions for both ions and electrons. The approach is an extension of the typical hydrodynamic formulation considering both the diffusional effect due to the potential and the density gradients in a self-consistent way with the electrostatic potential. The limit of this paper is that it neglects the presence of a collisionless layer close to the particle.

In 2007 the same authors [42] published a work that includes a collisionless layer in proximity of the particle surface by fixing the boundary condition for the density profile not at the particle radius but at a distance equal to the particle radius plus one mean free path. For the first time a minimum in the potential is predicted by an analytical theory that extends from the collisionless case to the hydrodynamic case.

The model used in *this* work instead starts from the work done by Gatti in 2007 [43] and is introduced in the following section.

2.2 Particle Charging accounting for ion-neutral charge-exchange and momentum transfer collisions

2.2.1 Electron charging frequency

For the range of pressures commonly used in the laboratory, electrons do not undergo collisions with neutrals within the sheath. The electron-neutral collision cross

section is much smaller than the ion-neutral one and even if they were to perform a few collisions within the sheath the ability to change their energy upon collisions is proportional to m_e/m_i, where $m_{e(i)}$ is the mass of the electron (ion), making elastic collisions for electrons a poor way to lose energy. As a result of this consideration for the electron current, it is appropriate to use the OML expression. In a repulsive field according to OML the cross section for collection is the geometric cross section of the collector and the density of electrons at the surface is equal to the electron density in the unperturbed plasma reduced by the Boltzmann factor, assuming the equilibrium (Maxwell-Boltzmann) distribution. As a result the electron charging frequency (ν_e) is then the same as in Eqs. 2.2.

Chapters 5 and 7 remove the assumption of a Maxwellian distribution for electrons. At that point, a different expression for the charging from electrons that takes into account the fact that electrons are not in thermodynamic equilibrium will be developed and introduced.

2.2.2 Ion charging frequency

Differently from OML, the ion charging frequency, ν_i, takes a different form because the ion current to the particle depends on the collisionality of ions with neutrals in the proximity of the particle surface and hence its expression requires some work.

It is necessary to evaluate the contribution to the ion current of ions that are collected only because they perform a collision in proximity of the particle and for the combination of energy and angular momentum would otherwise miss the particle. We will refer to this contribution as I_{CEC}, collision enhanced current. Also, to ensure a smooth transition to pressures typically appropriate for the hydrodynamic approach, the fraction of ions that collide many times within the sheath will contribute to the ion current according to the hydrodynamic expression (Equation 2.15).

All what is left at this point is to develop an exact expression for the probability of performing none, one or more than one collision within a certain distance.

The potential distribution around the particle follows fairly accurately a Debye-Hückel potential [44]:

$$V(r) = V_p \frac{R_p}{r} exp\left(-\frac{r - R_p}{\lambda_{DL}}\right) \tag{2.6}$$

where V_p is the potential at the particle surface and r is the radial coordinate.

With this assumption of the potential around the particle it is now possible to define a characteristic length R_0 ("capture radius"). It is postulated here, as it represents the heart of this model, that if an ion, that otherwise would miss the particle, performs exactly one collision within the capture radius, it will be collected by the particle, regardless of its angular momentum, hence enhancing the ion current to the particle. The capture radius is defined as the *locus where the neutral kinetic energy equals the ion potential energy, due to the Debye-Hückel potential [43]*:

$$R_0 = R_0|_{|EK(neutral)^*|=|eV(R_0)|} \tag{2.7}$$

The neutral kinetic energy is a function of the background gas temperature:

$$EK(neutral)^* = \frac{3}{2} k_B T_n$$

then:

$$\frac{3}{2} k_B T_n + eV_p \frac{R_p}{R_0} exp\left(-\frac{R_0 - R_p}{\lambda_{DL}}\right) \approx \frac{3}{2} k_B T_n + eV_p \frac{R_p}{R_0}\left(1 - \frac{R_0 - R_p}{\lambda_{DL}}\right) = 0 \tag{2.8}$$

A linearization is needed to provide a closed expression for R_0 and from molecular

dynamics simulations [43] appears to be accurate enough for this purpose:

$$R_0 = \frac{e|V_p|R_p\left(1+\frac{R_p}{\lambda_{DL}}\right)}{\frac{3}{2}k_B T_n + e|V_p|\frac{R_p}{\lambda_{DL}}} \tag{2.9}$$

Clearly the capture radius is also a function of the charge on the particle. It is now possible to investigate the collisionality of ions in proximity of the particle surface in terms of the probability that an ion undergoes none, one or more than one collision within the capture radius.

For the fraction of ions that perform no collision within the capture sphere, the expression used for the ion current is essentially based on the OML theory (Equation 2.13).

For the ions that undergo exactly one collision within the capture sphere, the appropriate expression for the ion current is equal to the thermal ion current through the capture sphere surface (Equation 2.14).

For the fraction of ions that undergo more than one collision within the capture sphere the appropriate expression for the ion current is based on a continuum approach (Equation 2.15). The probability of performing none, one or more than one collision are results of gas kinetic theory by Varney [45] and defined as follows:

$$\begin{cases} P_{c=0} &= \exp\left(-\frac{\alpha R_0}{\lambda_i}\right) \\ P_{c=1} &= \left(\frac{\alpha R_0}{\lambda_i}\right)\exp\left(-\frac{\alpha R_0}{\lambda_i}\right) \\ P_{c>1} &= 1 - P_{c=0} - P_{c=1} \end{cases} \tag{2.10}$$

here α is a correction factor and λ_i is the ion mean free path between collisions:

- $\alpha = 2.44$ accounts for the fact that the ion traveling inside the capture radius will follow a path that depends on R_0 but it is not equal to it. α is derived as

follows: upon collisions the majority of ions will have an energy lower than the average kinetic energy (this is due to the difference between mean and median energy); therefore the majority of ions will experience a larger capture radius. If we assume the ions to have a Maxwellian distribution:

$$\alpha' = \frac{\int_0^\infty R_o(E) f(E) dE}{R_0|_{E=\frac{3}{2}k_B T_i}} = 1.22 \tag{2.11}$$

And since the ion can perform a collision approaching the particle or moving away from it, $\alpha = 2 \times \alpha' = 2.44$.

- λ_i is the average ion mean free path and it is defined as follows:

$$\lambda_i = \frac{1}{\sigma_i n} = \frac{k_B T_i}{p \sigma_i} \tag{2.12}$$

here σ_i (for Argon= $40.9 \times 10^{-20} m^2$) is the average ion-neutral collision cross-section and p is the pressure.

The ion charging frequencies are defined as:

$$\nu_{i,OML} = \frac{1}{4} n_i (4\pi R_p^2) \sqrt{\frac{8 k_B T_i}{\pi m_i}} \left(1 - \frac{e V_p}{k_B T_i}\right) \tag{2.13}$$

$$\nu_{i,CEC} = \frac{1}{4} n_i (4\pi R_0^2) \sqrt{\frac{8 k_B T_i}{\pi m_i}} \tag{2.14}$$

$$\nu_{i,CONT} = 4\pi R_p n_i \mu_i |V_p| \tag{2.15}$$

μ_i is the ion mobility defined as:

$$\mu_i = \frac{e D_i}{k_B T_i} \tag{2.16}$$

where D_i is the Einstein diffusion coefficient which is:

$$D_i = \frac{3\pi}{16\sqrt{2}}\sqrt{\frac{8k_BT_i}{\pi m_i}}\lambda_i \tag{2.17}$$

2.2.3 Charging model solution

The model essentially evaluates the amount of charge on the particle by solving the following non-linear equation based on matching the electron and ion charging frequencies to the particle:

$$\nu_e(V_p) = P_{c=0}\ \nu_{i,OML}(V_p) + P_{c=1}\ \nu_{i,CEC}(R_0(V_p)) + P_{c>1}\ \nu_{i,CONT}(V_p) \tag{2.18}$$

Results of this charging model are presented in Chapter 3 and show a reduction of the negative average charge carried by particles, a charge that is pressure dependent and an enhancement of the current fluxes to the surface of the nanoparticles.

2.3 Background on Power Measurements

The presence of nanoparticles in plasmas also has a macroscopic effect on the electrical properties of the plasma. Chapter 6 studies these effects in terms of how nanoparticles affect the power coupling in capacitively-coupled plasmas (CCPs) . Bouchoule and Boufendi [8] and Bohm and Perrin [46] conducted experiments for larger size particles to study their effect in dusty plasmas. They observed that the resistivity and power dissipation is higher in a dusty plasma than that in a "pristine" plasma. The physical reason behind this behaviour can be linked to the enhanced collisions between electrons and nanoparticles. Both elastic and inelastic collisions contribute to change the dynamics for the electrons in a way that on a macroscopic scale manifests itself as a more resistive behavior for the impedance of the plasma. Any resistive

behavior in a radio-frequency plasma is the result of collisions between electrons and "some other" collision partner. It is easy to see, in fact, that in the total absence of collisions, electrons in a time varying electric field would reach the maximum speed at the time of a zero electric field. In a purely collisionless case, electron velocity ($\approx$ current) and electric field would be out of phase from each other by $\frac{\pi}{2}$, providing a purely capacitive behaviour and preventing any power to be coupled to the plasma.

For a radio-frequency plasma, without nanoparticles in it, an analytic expression for the conductivity of the medium is possible [47]; the complex conductivity σ' relates the total density of current (including the displacement current) to the electric field:

$$j = \sigma' E = (\sigma + i\omega\epsilon)\, E \tag{2.19}$$

Here σ is the plasma conductivity, while ϵ is the dielectric permittivity in the oscillating field:

$$\begin{aligned} \sigma &= \frac{e^2 n_e \nu_m}{m_e(\omega^2+\nu_m^2)} \\ \epsilon &= 1 - \frac{e^2 n_e}{m_e(\omega^2+\nu_m^2)} \end{aligned} \tag{2.20}$$

here ν_m is the electron-neutral collision frequency while ω is the angular frequency for plasma excitation ($2\pi \times 13.56$ MHz). Such expression for the case of the dusty-plasmas is not yet available and, while an estimate of the collision cross-sections for electron and nanoparticles is possible, collision frequencies depend on the nanoparticle density as well, a parameter that, at small nanoparticle sizes, is very difficult to measure. From a qualitative point of view a similar behavior is expected in dusty plasma, where an enhancement of collisions should lead to a more resistive behavior.

Power measurements in radio-frequency plasmas are based on the measurement of the waveforms for the current, the voltage, and are accurate to the point of the evaluation

of the phase difference between the two. A good approximation for the power is:

$$P = 1/2|V_\omega| \times |I_\omega| \times cos(\phi) \tag{2.21}$$

where V_ω and I_ω are the amplitudes of the principal component (first harmonic) of voltage and current and ϕ is the phase between them.

Chapter 6 presents results of power measurements performed in pristine and dusty plasmas that are in very good agreement with the findings in [8].

2.4 Background on Ion Energy Distributions

As the morphology and surface states of plasma-produced nanocrystals strongly affect their properties, it is important to investigate the effects that can affect the morphology of the surface of nanoparticles in plasmas as a result of interactions with other plasma species. As electrons charge nanoparticles negatively, a steady-state electric field that accelerates positive ions towards the surface of the nanoparticles is established. Chapter 5 studies the effects of this self-sustained electric field on the resulting ion energy distribution of ions reaching the surface. Ion-neutral charge exchange collisions are shown to play a major role in the final shape of the IEDF (ion energy distribution function). A change in the plasma pressure leads to variation of the ion energy profiles that can prevent ion-induced damage and favour crystallization of the surface.

The results obtained are being used as starting point for molecular dynamic computations directly analyzing the effects of different ion energy profiles on the binding state and morphology of surface species in silicon nanoparticles.

2.5 Background on Electron Energy Distributions

For electrons in a plasma it is possible to define a *distribution function* $f(\vec{r}, \vec{v}, t)$ in the six dimensional *phase space* of positions and velocities. This distribution:

$$f(\vec{r}, \vec{v}, t) d^3r d^3v \tag{2.22}$$

indicates the fraction of electrons inside the six-dimensional infinitesimal volume $d^3r d^3v$ at time t. The *Boltzmann equation* is the "continuity" equation that keeps track of the changes of the electron distribution as a result of the forces acting on electrons and of collisions among them and with other charged or neutral species [48]:

$$\frac{\partial f}{\partial t} + \vec{v} \cdot \nabla_r f + \frac{\vec{F}}{m_e} \cdot \nabla_v f = \left. \frac{\partial f}{\partial t} \right|_c \tag{2.23}$$

The term on the RHS (right hand side) keeps track of those changes in f that take place on a time scale much shorter than the typical time scale over which f evolves. These events are collisions that *instantaneously* remove electrons from a certain position in velocity space and put them in a different one.

The solution of the Boltzmann equation in low-pressure plasma is very important because it is able to capture the variation from thermodynamic equilibrium of the electron distribution in energy space. Many processes in plasma are stronlgy affected and affect the so-called "high energy-tail" of the electron energy distribution. Excitation and ionization processes in argon for example, when taking place in a single step, require electrons with energies of respectively 11.5 and 15.76 eV. The rate of excitation and ionization and the density of electrons with sufficient energy to perform those processes are strongly correlated.

In a plasma in steady-state, ion-electron losses have to match exactly the creation of new electron-ion pairs by ionizing collisions. Nanoparticles in plasma collect ions

and electrons. This not only affects the charging of the nanoparticles but also alters the properties of the plasma. Because of the presence of the nanoparticles in plasma, the loss of electrons and ions to recombination on the nanoparticle surface increases. This topic will be discussed in detail in Chapter 7 but it is quite intuitive and true that, because of the increased losses, there needs to be an increase in the ionization rate to maintain the plasma. This extra ionization effort usually comes at the cost of a reduced ion density available in the plasma, for a constant input power to the discharge.

Chapter 7 develops equations suitable for describing the elastic and inelastic collisions between electrons and nanoparticles in the Boltzmann equation. Such equation is then solved, in a "two-terms" approximation, to study the effects of the presence of nanoparticles on the distribution of electron energies.

Chapter 3

Charging, heating, and coagulation plasma model

3.1 Introduction

In this chapter we develop a model for nanoparticle charging, heating, and coagulation in low-pressure argon plasma. The charging model is essentially based on the work of Gatti and Kortshagen [49]. In that paper Gatti demonstrated that based on the capture radius concept, an elegant and accurate model can be developed to describe the explicit dependence of the particle charge on the particle size.

Both the charging and the heating mechanisms presented in this chapter rely on the assumption that particles are free-standing in the plasma so it is necessary to make sure that, even if particles are on average less charged than the OML prediction, the residual unipolarity of the nanoparticle population is still sufficient to prevent coagulation. Section 3.2.4 presents the results of a simple coagulation model that proves this point. The assumptions made in that model, however, do not take into account the effect of *image charges* between large negatively charged particles and small neutral particles that in [28] where shown to play an important role in enhancing coagulation.

In the field of dusty plasma applications for nanoparticle synthesis particle temperature is as important a parameter as particle charge is for the physics of dusty plasmas. The ability to heat nanoparticles to temperatures above their crystallization point while keeping them suspended in a plasma at room temperature is an interesting example of non-equilibrium interaction [14]. In principle one could think of a nano-dusty plasma in terms of a three temperatures fluid where $T_e > T_p > T_i \approx T_n$ (respectively electron, dust and ion/neutral temperatures). In many experiments it was observed that the nanoparticles formed in the plasma are crystalline in nature [50, 51, 12, 52, 53, 54], which, depending on the nanoparticle material, suggests a rather high temperature during the particle formation. For particles in the nanometer range it is expected to see a reduction of the melting and crystallization temperatures with decresing size [55]. Hirasawa et al., [56] (see Figure 3.1) reported that the crystallization temperature of silicon particles with diameters between 4 and 10 nm are between 773 and 1173 K, temperatures substantially lower than bulk silicon's.

In this chapter, we integrate the concepts of capture radius and enhanced ion current to the nanoparticle surface in a comprehensive numerical model for the heating that also includes the effects of hydrogen radicals to calculate the temperature of small silicon nanoparticles in plasmas. We show that under typical laboratory plasma conditions, silicon nanoparticles experience temperatures that can favour their crystallization.

The chapter is organized as follows: the numerical models are introduced in section 3.2. Section 3.3 discusses some experimental results that correlate well with the model and conclusions are summarized in Sec. 3.4.

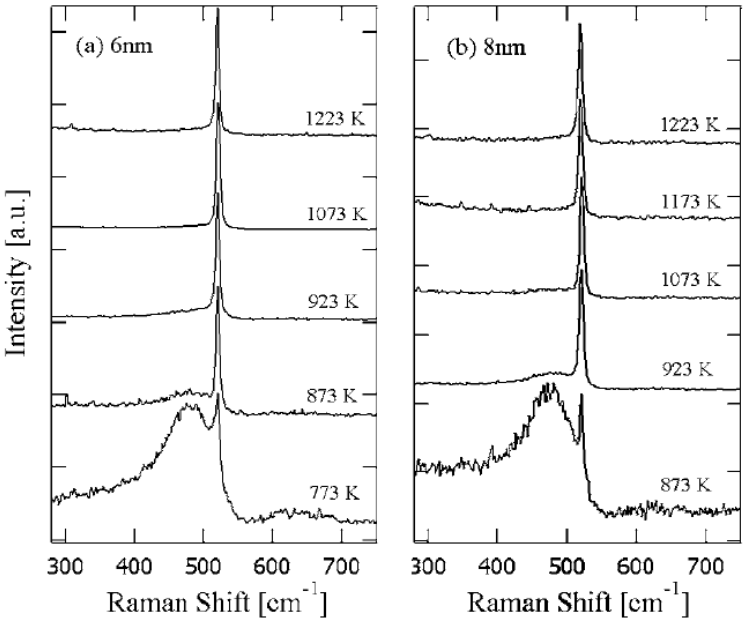

Figure 3.1: Crystallization temperature dependence on the size of Si nanoparticles synthesized by pulsed laser ablation was studied using Raman scattering spectroscopy. The crystallization temperature values for 10, 8, 6 and 4 nm particles were 1273, 1173, 1073, and 773 K, while bulk melting temperature is 1683 K.

3.2 Model

3.2.1 Charging

The particle potential is calculated by equalizing the ion and electron currents from the solution of the non-linear equation, that we presented in the previous chapter:

$$I_e(V_p) = P_{C=0} I_i^{OML}(V_p) + P_{C=1} I_i^{CE}(R_c(V_p)) + P_{C>1} I_i^{HY}(V_p) \tag{3.1}$$

each term is weighted according to the probability that an ion performs none, one and many collisions within the capture radius. Varney [45] calculated these quantities as:

$$P_0 = \exp\left(-\frac{\alpha R_c}{\lambda_i}\right) \tag{3.2}$$

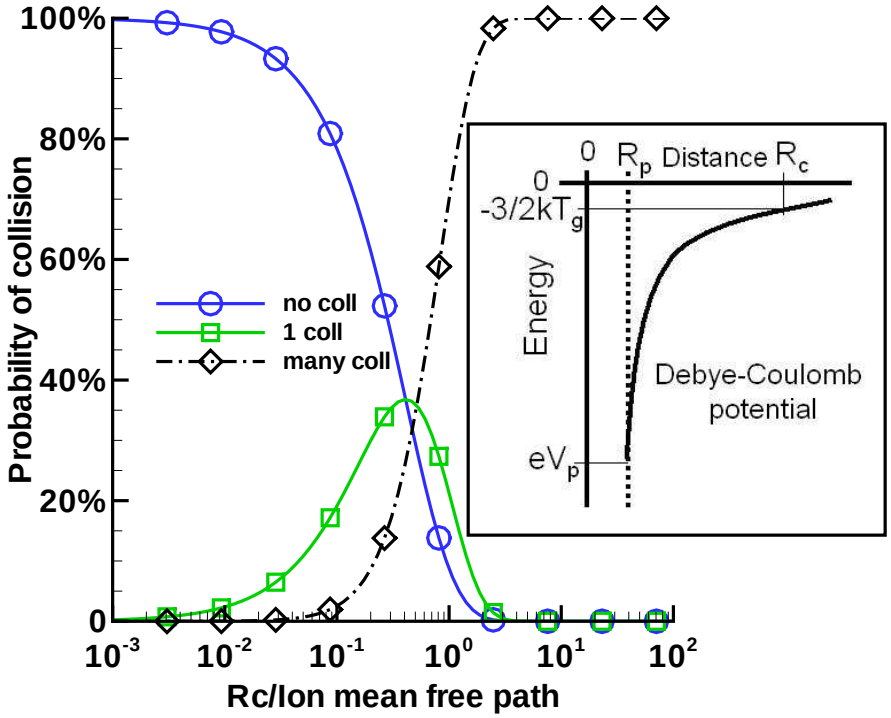

Figure 3.2: Probability of an ion to undergo none, one or many collisions within the capture radius, defined as in the insert.

$$P_1 = \left(\frac{\alpha R_o}{\lambda_i}\right) \exp\left(-\frac{\alpha R_o}{\lambda_i}\right) \tag{3.3}$$

$$P_{>1} = 1 - P_0 - P_1 \tag{3.4}$$

where λ_i is the ion mean free path. P_0 P_1 and $P_{>1}$ are strong functions of pressure. Figure 3.2 reports the probabilities of an ion undergoing none, one or many collisions within the capture radius. A visual representation of the capture radius is also presented in the insert. Since I_i^{CE} is usually larger than I_i^{OML}, close to the maximum in P_1 the ion current is strongly enhanced resulting in a less-negative particle potential and in a larger energy flux to the particle due to ion-electron recombinations.

In this computation the electron temperature is also self-consistently evaluated from a simple ionization-balance model. Assuming a Maxwellian distribution of electron

energies, ion losses to the walls and to the particle surfaces have to be compensated by ions produced by electron-neutral ionization events. In this balance:

$$n_i \frac{D_a}{l} A + n_i \nu_{ip} V = n_e \nu_i(T_e) V \tag{3.5}$$

- A represent the area bounding the plasma volume (V) in a reactor of diameter 13 cm and height 10 cm.
- l is a characteristic diffusion length, estimated to be 5 mm in this case,
- D_a is the ambipolar diffusion coefficient. Ultimately it is proportional to electron temperature and inversely proportional to neutral pressure. In case where pressure is parametrically investigated this is important since for larger pressures we expect a reduction of diffusion, reduced diffusional losses to the surfaces of the reactor, a plasma "sustainable" at a lower electron temperature, and as a result, even smaller diffusional losses. ($D_a = \mu_i T_e \approx T_e/p$).
- ν_{ip} is the ion loss frequency to the particles, $\approx I_i/e \times n_p/n_i$, ($n_p$ is the nanoparticle density) and finally
- $\nu_i(T_e)$ is the average ionization frequency. The average ionization frequency can be expressed analytically if a linear approximation for the ionization cross-section is used:

  $$\sigma_x = \beta_i(u - u_i) \tag{3.6}$$

  For argon a value of $\beta_i = 2 \times 10^{-21}\ m^2 eV^{-1}$ has been proposed [57] and an ionization threshold of 15.76 eV is used. As a result one can express ν_i in terms of the incomplete gamma function [58]: $\Gamma(a,x) = \int_x^\infty t^{a-1}e^{-t}dt$, leading to:

  $$\nu_i = n\sqrt{\frac{8T_e}{\pi m_e}}\beta_i \left(T_e \Gamma\left(3, \frac{u_i}{T_e}\right) - u_i \Gamma\left(2, \frac{u_i}{T_e}\right)\right) \tag{3.7}$$

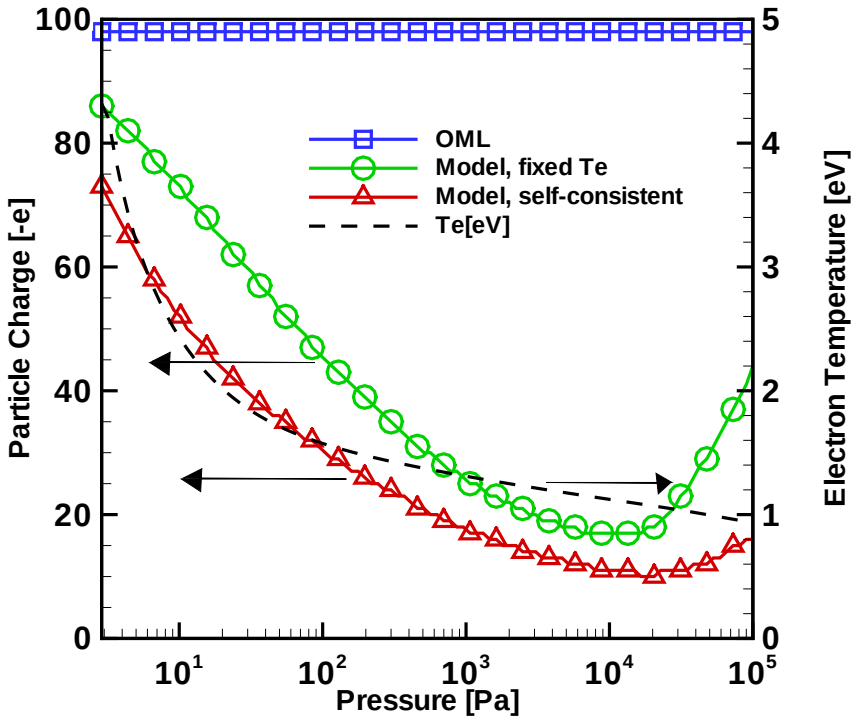

Figure 3.3: Charge carried by a 40 nm diameter particle against pressure in an Argon plasma, $T_i = 400$ K, $n_i = 1 \times 10^{16}$ m^{-3}, $n_p = 1 \times 10^{14}$ m^{-3}; $T_e = 3$ eV when not self-consistently evaluated.

The main contribution of this additional part of the charging model is to take into account that electron temperature should not be fixed at a value for all pressures investigated. T_e is not an input parameter for the plasma, but results from a complex combination of factors, including pressure, reactor geometry, and gas composition.

Figures 3.3 and 3.4 show the charge carried by 40 nm and 1 μm size particles, respectively, over a range of plasma pressures, according to this model and to the OML theory. From those results it is clear that the particle charge is much reduced by the effect of charge-exchange collisions as charging is now a strong function of pressure. The effect of pressure on the electron temperature necessary to maintain a constant ion density is to have lower electron temperatures for higher pressures, confirming our earlier intuition.

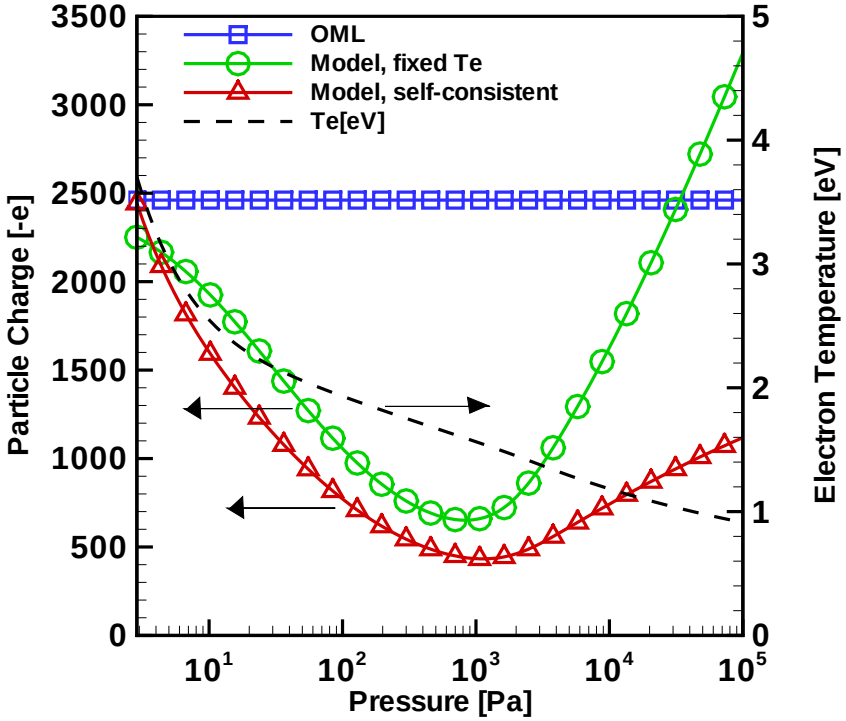

Figure 3.4: Charge carried by a 1 μm diameter particle against pressure in an Argon plasma, $T_i = 300$ K, $n_i = 1 \times 10^{16}$ m^{-3}, $n_p = 1 \times 10^{14}$ m^{-3}; $T_e = 3$ eV when not self-consistently evaluated.

3.2.2 Charge distribution

For nanometer-sized particles the knowledge of the average charge alone may not be sufficient, since particles a few nanometres in diameter can carry only a small number of elementary charges. For such small particles, it is more instructive to look at the charge distribution, as charging is stochastic in nature and particles can hold only an integer number of elementary charges. With a little effort it is possible to evaluate not only the average charge that a particle will carry in a plasma of certain characteristics but also the charge distribution. Even assuming a monodisperse aerosol, that is a collection of particles of the same size, it is easy to realize that there is a finite probability that a particle carries a charge at a point in time that is slightly different from the average value. The charge distribution of particles of a given radius R_p is

described by the fraction of particles F_k carrying a charge ke. Overall this distribution is normalized by $\sum_k F_k = 1$. The rate equation for a charge state k can be written as [4]:

$$\frac{dF_k}{dt} = \nu_e^{k+1} F_{k+1} - \nu_e^k F_k - \nu_i^k F_k + \nu_i^{k-1} F_{k-1} \tag{3.8}$$

where the increase in the fraction of particles with charge ke is due to electrons charging particles with $(k+1)e$ and ions recombining on particles carrying $(k-1)e$ while it is decreased by any charging event, ion or electron, happening within the same F_k class.

Under most circumstances, the charging of particles is much faster than coagulation so the charge distribution can be considered in steady state. We can prove that by assuming an aerosol of *monodisperse* particles, and assuming the size to be between 10 nm and 1 μm at a particle density of $1 \times 10^{12} cm^{-3}$. Monodispersity and such density values are fairly common in plasma production of nanoparticles. Assuming a constant coagulation coefficient $\beta_{ij} = K_{coag} = 1 \times 10^{-9} cm^3/s$, the Smokulowski coagulation equation and its time integration are:

$$\frac{dn}{dt} = -\frac{1}{2} K_{coag} n^2 \tag{3.9}$$

$$n(t) = \frac{n_0}{1 + t/\tau_{coag}} \tag{3.10}$$

where $\tau_{coag} = 2/K_{coag} n_0$. Coagulation times of the other of a few ms result. For charging [44]:

$$\tau_{charg} = \frac{4\frac{\epsilon_0}{e}\sqrt{\frac{\pi M_i}{8e}}\sqrt{\frac{kT_i}{e}}}{R_p n_i \left(1 - \eta(k)\right)} \tag{3.11}$$

Where $\eta(k)$ is:

$$\eta(k) = \frac{ke^2}{4\pi\epsilon_0 R_p k_B T_e} \tag{3.12}$$

So $\tau_{charg} \approx 1.5^{-6} s \div 1.2 \times 10^{-4}\ s$, making charging faster than coagulation.

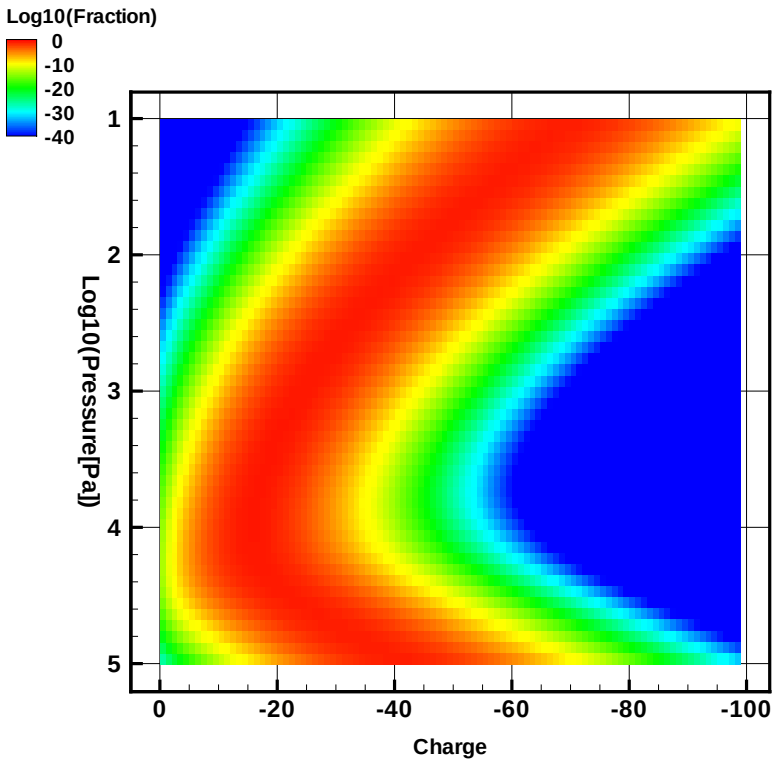

Figure 3.5: Charge distribution against pressure, Argon plasma, $T_e = 3$ eV, $T_i = 300$ K, $n_e = n_i = 1 \times 10^{16}$ m^{-3}, $R_p = 20$ nm

The detailed balancing between ion charging events and electron charging events allows the calculation of the charge distribution using recursive relations:

$$F_{k+1} = F_k \frac{\nu_i^k}{\nu_e^{k+1}} \tag{3.13}$$

An arbitrary value of 1 is temporarily given to $F_{k=min}$ as the values of the distribution function for larger k is computed. Once all of the F_k values are known the whole distribution is normalized so that $\sum_k F_k = 1$.

Figures 3.6, 3.7, 3.8 give examples of charge distributions for particles of 10, 40 and 1,000 nm in a plasma with the following properties: ion density of 1×10^{16}m^{-3}, electron temperature of 3 eV, ion temperature of 400 K and pressure of 1 Torr. These

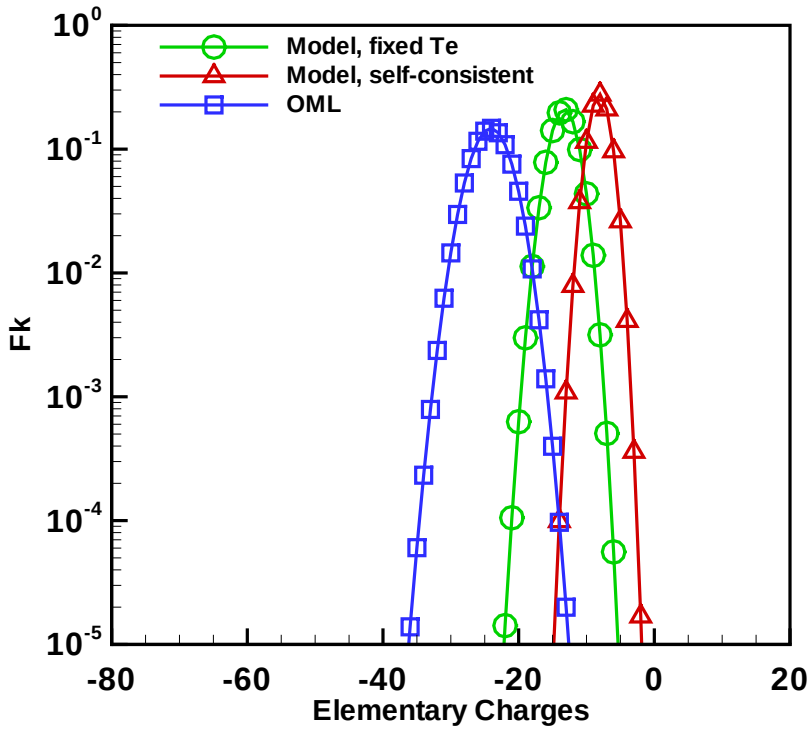

Figure 3.6: Particle charge distribution for a 10 nm diameter particle, in an Argon plasma, $T_i = 400$ K, $n_i = 1 \times 10^{16}$ m^{-3}, $n_p = 1 \times 10^{14}$ m^{-3}, p = 1 Torr; $T_e = 3$ eV when not self-consistently evaluated.

values are fairly common in laboratory plasma applications.

Figure 3.5 instead presents the charge distribution for a nanoparticle of 40 nm in diameter versus pressure, for a plasma with properties as reported in the caption.

As it is evident from the charge distribution for small particles, there is a finite fraction of particles with a charge that is close to zero. This may have consequences on the coagulation of nanoparticles and it is studied in a following section.

3.2.3 Other results of the charging model

In Figure 3.9 it is shown how the difference in the charge of the particles for the model and OML increases with particle size.

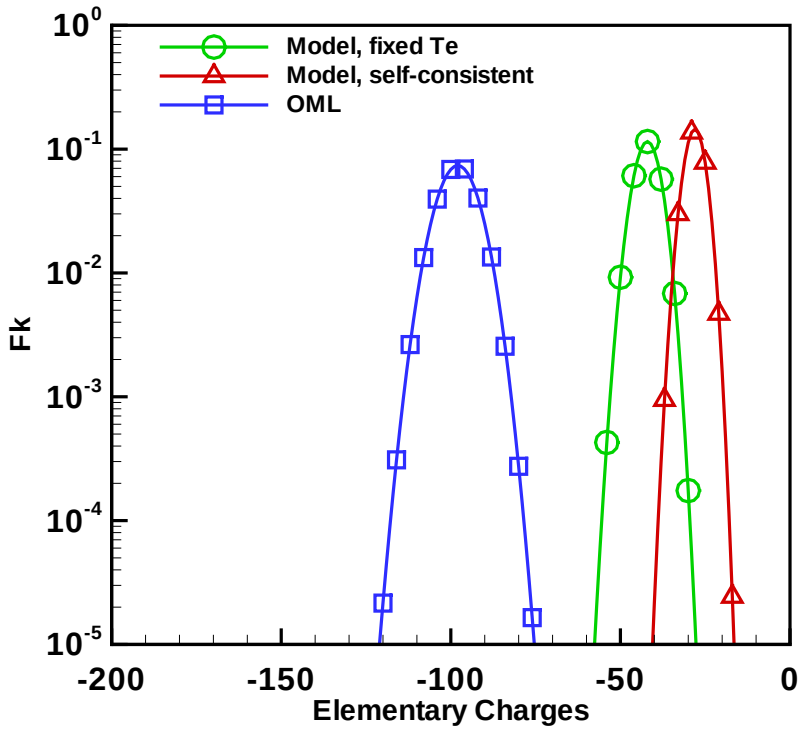

Figure 3.7: Particle charge distribution for a 40 nm diameter particle, in an Argon plasma, $T_i = 400$ K, $n_i = 1 \times 10^{16}$ m^{-3}, $n_p = 1 \times 10^{14}$ m^{-3}, p = 1 Torr; $T_e = 3$ eV when not self-consistently evaluated.

In Figure 3.10 the behavior of the charge with respect to the electron temperature of the plasma is reported (for a 40 nm particle). Interestingly, the charge depends much less on the electron temperature, than in the OML case. This is due to the fact that while a large electron energy contributes to a larger electron current, a larger sheath contributes to a larger capture radius, partially compensating the effects of electron charging.

The effect of neutral/ion temperature is investigated in Figure 3.11, where it can be seen that at larger neutral temperatures the particle are more negatively charged. A larger average ion energy means a smaller capture radius, a smaller collection of ions and relatively more negative net charge.

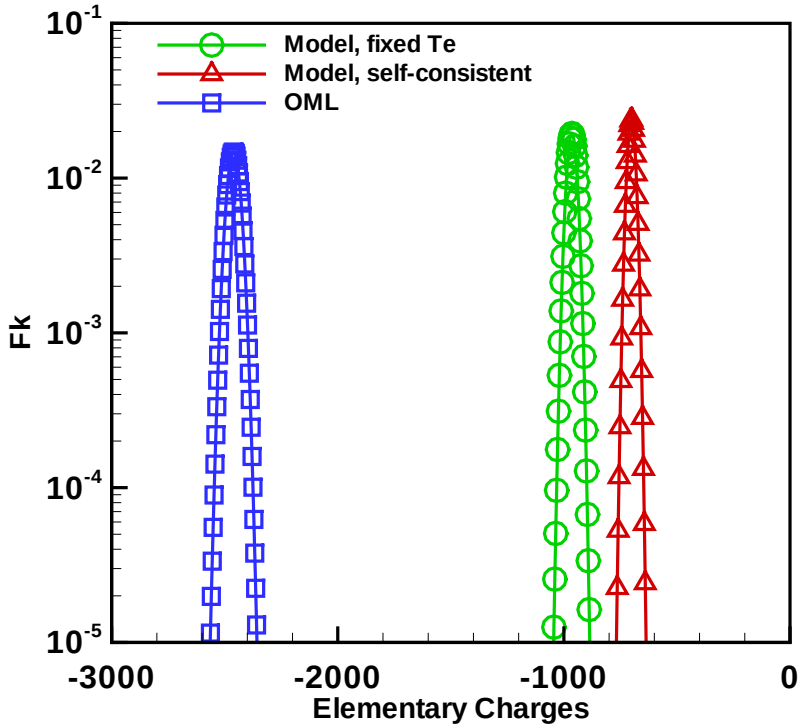

Figure 3.8: Particle charge distribution for a 1 μm diameter particle, in an Argon plasma, $T_i = 400$ K, $n_i = 1 \times 10^{16}$ m^{-3}, $n_p = 1 \times 10^{14}$ m^{-3}, p = 1 Torr; $T_e = 3$ eV when not self-consistently evaluated.

3.2.4 Coagulation

Courteille *et al.* [59] conducted experiments on coagulation of nanoparticles in plasmas and developed a model to explain the results from their experiments. In their model, the particles were considered to be neutral and to undergo Brownian free-molecular coagulation. The results from the model match closely with their experimental results, however, the average charge of the particles at this stage should be negative because of the difference in mobilities of ions and electrons in plasma. Because of the repulsive interactions between the unipolarly charged particles, one would expect the coagulation rate of the particles to be lower than that of the neutral particles.

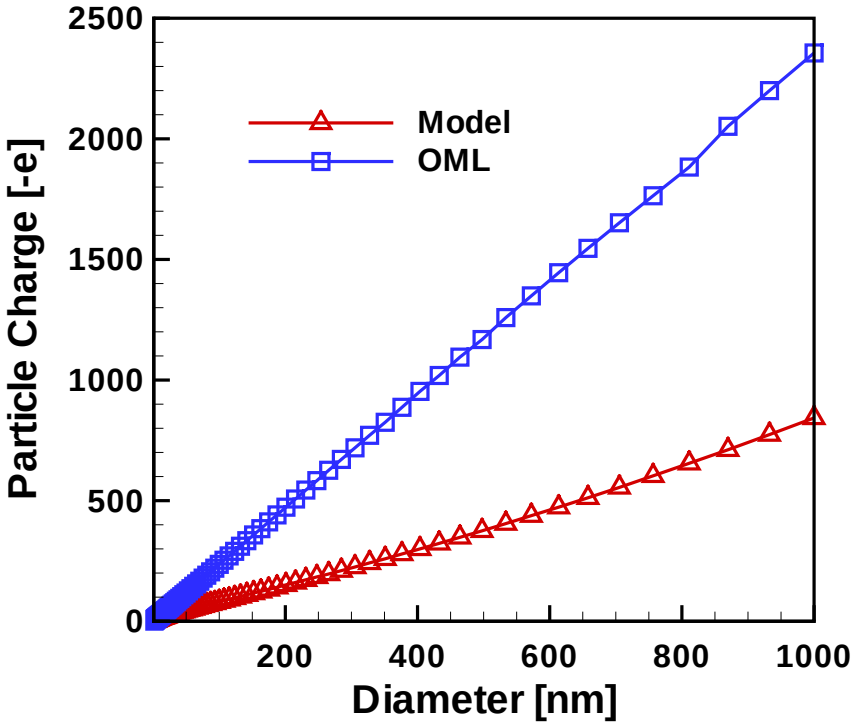

Figure 3.9: Charge against particle diameter for model and OML, Argon plasma, T_e = 3 eV, T_i = 300 K, $n_e = n_i = 1 \times 10^{16}$ m^{-3}, p = 1 Torr

Furthermore, Watanabe *et al.* [60] observed the rate of growth of nanoparticles in plasmas to be higher than the one by Brownian free molecular coagulation of neutral particles. The increase in the coagulation rate relative to that of neutral particles has been attributed to the charge fluctuations of the particles about their mean charge [61, 62]. When the size of the nanoparticles is less than a few nanometers, the mean charge on the nanoparticles is only one elementary negative charge. With charge fluctuations, some of the nanoparticles can be neutral or even positively charged, thus increasing the coagulation of the oppositely charged nanoparticles.

Warthesen and Girshick, developed a one-dimensional (1D) self-consistent model to simulate the spatiotemporal behavior of the nanoparticle-plasma systems for the same conditions as in the experiments of Boufendi and Bouchoule *et al.* [8]. Their model

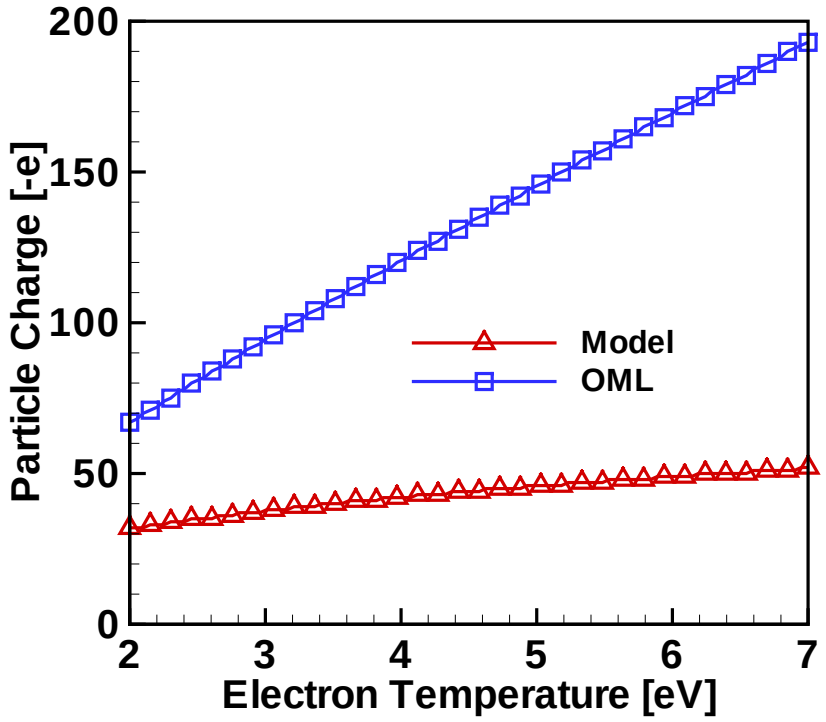

Figure 3.10: Charge against electron temperature for model and OML, Argon plasma, $T_i = 300$ K, $n_e = n_i = 1 \times 10^{16}$ m^{-3}, p = 1 Torr, $R_p = 20$ nm.

showed no noticeable change in the nano-dusty plasma behavior whether coagulation was turned on or off. However, the transmission electron microscopy (TEM) images taken of the nanoparticles deposited in plasma by Boufendi and Bouchoule [63] show large particles comprising of smaller nanoparticles which indicates that coagulation is one of the stages in the growth of nanoparticles in plasmas, at least in plasmas with a very large initial concentration of very small size nanoparticles.

The coagulation model presented here consists of the solution of the general dynamic equation (GDE) using coagulation rates appropriate for a population of charged particles. Instead of the direct solution of the GDE, a sectional model is adopted [64] [65].

The particle distribution function is usually considered in terms of the particle volume

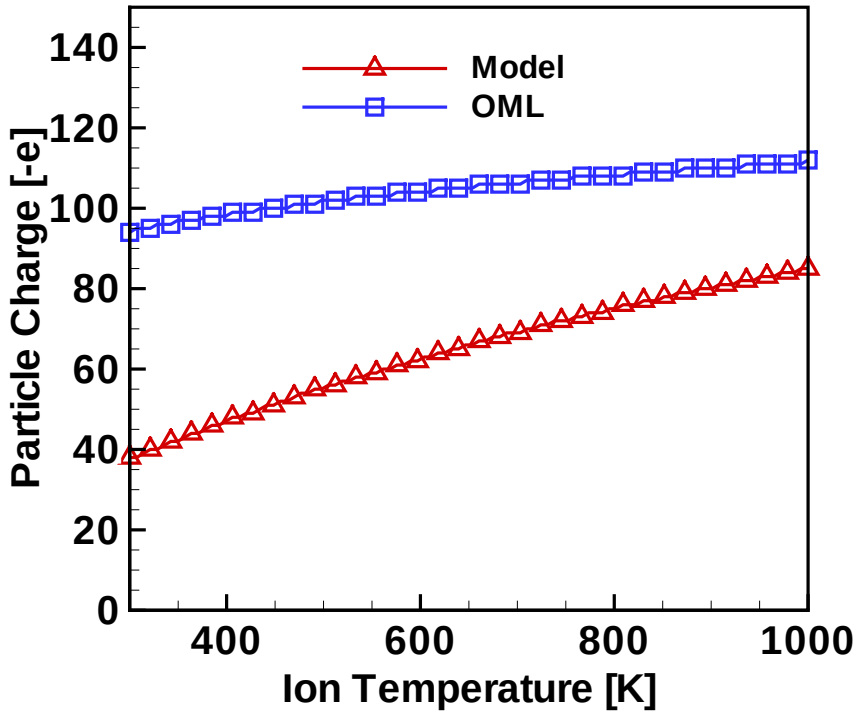

Figure 3.11: Charge against ion temperature for model and OML, Argon plasma, T_e = 3 eV, $n_e = n_i = 1 \times 10^{16}$ m^{-3}, p = 1 Torr, R_p = 20 nm.

v . If $n(v)$ denotes the particle number density in a volume range $(v,\ v + dv)$, the temporal evolution of $n(v)$ is described by the general dynamic equation GDE for an aerosol:

$$\frac{\partial n(v)}{\partial t} = \frac{1}{2}\int_0^v \beta(v', v - v')n(v')n(v - v')dv' - \int_0^\infty \beta(v, v')n(v)n(v')dv' \qquad (3.14)$$

The first term on the right hand side accounts for the change of particles within the volume range $(v,\ v + dv)$ due to coagulation of smaller particles. The second term describes the loss of particles from the same volume element due to coagulation with particles of any volume. $\beta(v', v - v')$ is the frequency for coagulation between two

particles with a volume v and v'. Assuming free molecular regime, β is given by [66]

$$\beta(v,v') = \alpha(v,v')\left(\frac{3}{4\pi}\right)^{1/6}\left(\frac{6k_BT_p}{\rho_p}\right)^{1/2}\left(\frac{1}{v}+\frac{1}{v'}\right)^{1/2}\times(v^{1/3}+v'^{1/3})^2 \tag{3.15}$$

where v and v' are the volumes of the particles interacting, ρ is the density of the particles, and T_p is the temperature of the particles. $\alpha(v,v')$ is a coefficient which describes that the effective cross section for coagulation depends on the charge of both particles:

$$\alpha(v,v') = \sum_{k=-\infty}^{\infty}\sum_{k'=-\infty}^{\infty} F_k(v)F_{k'}(v')Q(k,k',v,v') \tag{3.16}$$

Assuming cross sections given by the OML theory (applied to nanoparticles, not to ions!) yields:

$$\begin{aligned} Q(k,k',v,v') &= \exp\left(-\tfrac{kk'e^2}{4\pi\epsilon_0 R_s k_B T_p}\right), \quad kk' > 0 \\ &= 1-\tfrac{kk'e^2}{4\pi\epsilon_0 R_s k_B T_p}, \qquad kk' \le 0 \end{aligned} \tag{3.17}$$

and $R_s = (3/4\pi)^{1/3}(v^{1/3}+v'^{1/3})$.

In the sectional model, the domain of volume considered is divided on a logarithmic scale into equal sections, resulting in a discretization of the solution for the evolution of particle "bin" sizes. A set of rate equations for each "bin" size is derived. The coagulation frequency appears in integral coefficients, which have to be evaluated only once at the beginning of the calculation if $\alpha(v,v')$ is factored out of the integral. Only the coefficients $\alpha(v,v')$ have to be updated during the coagulation process to account for changes in the plasma conditions and of the particle charge distribution. The charge distribution during the coagulation process has to be determined for particles in each section, since the particle charge distribution depends on the particle radius. In our case, we consider particles between 1 and 10 nm diameter and the volume

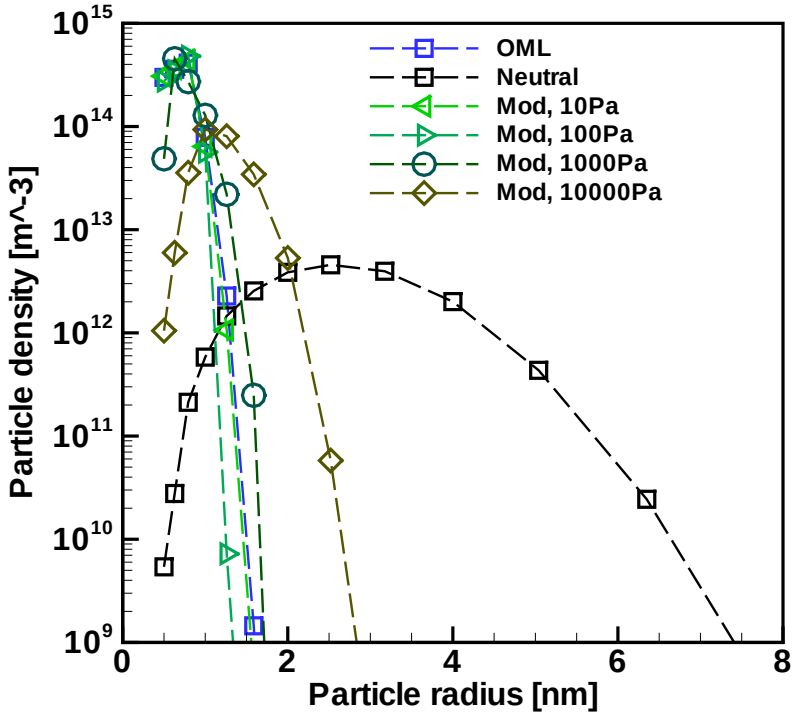

Figure 3.12: Particle size distribution generated from coagulation of $1 \times 10^{15} m^{-3}$, monodisperse (1 nm diameter) particle source in Argon plasma, $T_e = 3eV$, $T_i = 400K$, $n_i = 1 \times 10^{15} m^{-3}$ in 100 s, with the method in [4].

range was divided into 100 sections.

Figure 3.12 shows the result of the simulation over a time of 100 s for both the OML charge distribution and the one based on the charging model developed in this chapter. Neither diverges significantly from the monodisperse size distribution the simulation began with. For a neutrally charged aerosol, also reported in the plot, the situation is different as 100 s are sufficient to see the onset of a polydisperse size distribution. This confirms that nanometer size particles within a plasma do not undergo coagulation and the assumption of free-standing particles within the plasma is satisfied, under the conditions considered here.

3.2.5 Particle heating in a low-pressure argon-silane plasma

Selective nanoparticle heating during plasma synthesis is the result of energetic reactions taking place at the nanoparticle surface. This is a powerful benefit for making plasma synthesis attractive in the production of covalently bonded semiconductor materials that require high temperatures for crystal formation.

To make the reader familiar with this topic a brief literature review is necessary and is presented here.

Mangolini *et al.* and Jurbergs *et al.* in [12, 67] reported the production of crystalline nano-particles for lighting purposes. In their work they demonstrate a simple, single-step, scalable, high-yield synthesis process for luminescent silicon nanocrystals based on a low-pressure non-thermal plasma. Silicon nanocrystals with diameters of less than 5 nm show efficient photoluminescence at room temperature. Such results rely on the ability to produce small, crystalline silicon nano-particles.

A study by Anthony and Kortshagen [68] on producing silicon nanoparticles with different power inputs to the plasma showed a transition from amorphous to crystalline nano-dots above a threshold power level.

In 2006 Morfill and co-workers [69] implemented a model of grain surface temperature in a low-pressure weakly ionized complex plasma, refining it by taking into account the effect of rare ion-neutral collisions in the vicinity of the grain. The ion enhanced current is based on the model by Zobnin and co-workers [40], which, compared with the model used here, does not account for the transition to a hydrodynamic regime at larger pressures. The energy fluxes between plasma and grain surface are taken from Lifshitz [70]: cooling terms are conduction and radiation while heating terms include the recombination energy of electrons and ions on the particle surface and the kinetic energy of electrons and ions reaching the surface of the particle. Furthermore, they use

the blackbody approximation (absorptivity = emissivitiy = 1) for the radiation from the particles, a very rough approximation considering that for such small particles emissivity is expected to be much smaller than one [71].

Graves and co-workers [72] developed a spectroscopic technique to measure the temperature of phosphorescent particles suspended in a low-pressure RF plasma. In the particle energy balance they considered particle heating due to ion impact and ion-electron recombination, while they cosidered for cooling mechanisms radiation and gas conduction. They found particles to be only 75 K hotter than the gas. Questionable assumptions in their work are again the blackbody approximation and an accomodation coefficient which accounts for the fact that neutrals hitting the particle do not have enough time to thermally equilibrate on the surface of the particle. To match experimental results with their model they adjust this accomodation coefficient to a value of about 0.17, quite small. For argon this coefficient should be 0.86 instead [73]. This value is essentially representing the efficiency of thermalization for an argon atom impinging on a heated surface.

An interesting attempt to evaluate the temperature of a particle in a low pressure plasma was made by Kersten and co-workers [74]. A microphysical description of the charging of dust grains in a plasma was presented. The model which is based on plasma-wall interaction processes predicts the dependence of the grain charge on the particle radius and on the particle temperature better than the commonly used assumptions of a spherical capacitor. The thermal balance in Kersten's work takes into account several contributions such as kinetic energy of electrons and ions, ion recombination energy, thermal conduction and radiation. They predict a remarkable increase of the charge carrier flux to the dust grains with increasing pressure, together with a net particle charge reduction. They speculate that the increased particle temperature causes an increasing desorption of the charge carriers, resulting in the

observed weak decrease of the grain charge with pressure.

Another attempt was made by Swinkels and co-workers [75]. In their work the internal temperature of rhodamine B-dyes dust particles 1.2 μm in diameter was measured via a laser induced temperature dependent fluorescence measurement. In argon plasma they find a particle temperature that is RF power dependent but independent of pressure. From their analysis they realize that the main contribution to heating is due to electron-ion recombination while cooling via conduction and radiation are of equal importance.

Particle temperatures up to 450 K were also found by Stoffels *et al.* [76].

Together with the correlation between size and melting temperature [55], some work has been recently done in terms of correlating the onset of crystallization with temperature [77] [56]. Roura *et al.* found that silicon particles of about 60 nm in size crystallize at about 800 C^o. Hirasawa *et al.* instead studied crystallization temperature dependence on Si nanoparticles size using Raman scattering spectroscopy for much smaller size particles. Si nanoparticles synthesized by pulsed laser ablation, and initially amorphous, were annealed at various temperatures while they were suspended in helium background gas, and then were classified by a differential mobility analyzer. After the size classification Si nanoparticles showed a narrow size distribution which enabled investigation of the size dependent crystallization. The temperature threshold for the transition from amorphous to crystalline decreased as the particle size decreased and it is in good agreement with the melting temperature for silicon nanoparticles measured by Goldstein [55] with TEM analysis. The crystallization temperature values for 10, 8, 6 and 4 nm particles were 1273, 1173, 1073, and 773 K respectively, while bulk melting temperature is 1683 K (see Figure 3.1).

In a recent study on silicon nanocrystal formation [13], Bapat found highly regularly cubic-shaped silicon nanocrystals. The cubic shape is believed to be the equilibrium

shape for hydrogen terminated silicon nanocrystals [78]. Using a simple model, only accounting for electron-ion recombination at the particle surface, it was shown that particle temperatures of several hundred Kelvin above the gas temperature could be obtained for realistic plasma conditions.

In a even more recent study Mangolini *et al.* [14] extended that investigations by examining the temperature history of very small nanoparticles for diameters smaller than 10 nm. In the non-steady formulation of the energy balance used by the authors, however, the dependence of the ion current to the particle on pressure was not taken into account, as the OML approach was used. That work was interesting for showing for small particles having small "thermal inertia" the possibility to have large temperature fluctuations due to the stochastic nature of the heating events; in [14], however, the average particle temperature does not depend on the particle size. This is because both the heating and cooling terms are directly proportional to the surface area of the particle, making the average *steady state* particle temperature *size-independent*.

For the heating model used here a steady state particle energy balance for a spherical particle is used:

$$G(T_p, \chi) - L(T_p, \chi) = 0 \tag{3.18}$$

where G is the energy input term to the particle while L is the energy loss term. Both terms comprise different mechanisms that are a function of the particle temperature (T_p), considered uniform over the particle and χ, the fractional hydrogen coverage of the particle surface. Silicon particles produced in silane plasmas have always surface terminations with hydrogen. While each silicon surface atom can be terminated with 1, 2 or 3 hydrogen atoms, here we will assume an average value of two hydrogen atoms per silicon atom. With the introduction of a second equation tracking χ we have a non-linear system of 2 equations that is solved to find both temperature and

hydrogen coverage.

The heat sink term (L) in Equation 3.18 consists of conduction losses to the background gas and hydrogen thermal desorption from the particle surface [79]. Radiative heat losses are found to be much less significant than conduction heat losses given the size of the particle and their expected emissivity.

$$L = \frac{1}{4} n_{gas} (4\pi R_p^2) \sqrt{\frac{8 k_B T_{gas}}{\pi M_{gas}}} \frac{3}{2} k_B \left(T_{particle} - T_{gas}\right) + \frac{e \times 1.69[eV]}{2} \times \Gamma_H^{therm\ desorb} \quad (3.19)$$

The energy necessary for the recombination of H_2 is 1.69 eV and $\Gamma_H^{therm\ desorb}$ is the frequency of H released from the surface of the particle due to thermal desorption.

The reaction mechanism consists of 2 hydrogen atoms bonded to the surface of the particle that can, if the temperature is high enough, create a bond and leave the surface of the particle as a hydrogen molecule. There is a benefit in the form of entropy for the system to do so at high temperatures. For the functional definition of this term, see the first term of the RHS of Equation 3.28. The energy here is divided by 2 to account for the fact that the recombination involves 2 hydrogen atoms.

The generation term G in Equation 3.18 describes the heat released by ion-electron recombination (G_1) at the particle surface and by atomic hydrogen interactions with the particle (G_2) other than thermal desorption.

3.2.5.1 Ion-electron recombination on the particle

Each ion impinging on the particle surface is believed to recombine with an electron with probability 100% and in each recombination events an energy equal to 15.76 $[eV]$ is released. So G_1 is:

$$G_1 = e \times 15.76[eV] \times \frac{I_i(...)}{e} = 15.76[eV] \times I_i(...)\ [j] \quad (3.20)$$

The explanation of the functional dependence of I_i was given in previous sections.

3.2.5.2 Atomic hydrogen interactions with the particle

The collisions with atomic hydrogen can provide different heating mechanisms for the particle depending on whether the hydrogen lands on an open site (Si) or on an occupied site (H-terminated). The thermal flow of H atoms to the particle is:

$$\Gamma_H^{th} = \frac{1}{4} n_H (4\pi R_p^2) \sqrt{\frac{8 k_B T_H}{\pi m_H}} \tag{3.21}$$

T_H is the hydrogen temperature and it is assumed to be equal to the background gas temperature ($T_H = T_{back} = T_i$).

In the case of a hydrogen atom landing on an empty site, the hydrogen will bond with probability 100% and this process will release 3.1 eV, the Si-H bond energy. The first contribution to G_2 is:

$$G_2 = (e \times 3.1\ [eV]) \times \Gamma_H \times (1 - \chi) + ... \tag{3.22}$$

If the H lands on an occupied site, according to [80] there is an 11% probability that the H atom abstracts another H atom to form H_2. In this process, an energy equivalent to the difference between the Si-H bond energy and the H-H bond energy is released ($4.51 - 3.1 = 1.41\ [eV]$) and a H landing site is *freed* in the process. Updating G_2:

$$\begin{aligned} G_2 = {} & (e \times 3.1\ [eV]) \times \Gamma_H^{th} \times (1 - \chi) + \\ & + 0.11 \times (e \times 1.41\ [eV]) \times \Gamma_H \times \chi + ... \end{aligned} \tag{3.23}$$

For the remaining 89% one of two things can happen. The physisorbed H atom can diffuse on the surface of the particle until it reaches an open site. If that happens the energy released is equal to the Si-H bond energy (3.1 $[eV]$) and the count of the open

sites is diminished by one unit. Before finding a suitable open site, often in situations when χ is close to one, there is a possibility that an incoming H atom recombines with the physisorbed H atom *on the surface of the particle* releasing all of the H-H bond energy (4.51 $[eV]$). If this happens the count of open and occupied sites does not change. What is missing to implement this model is the frequency of H physisorbed on the particle diffusing to a dangling bond ($\nu_{H\ diff}$) and the frequency of H physisorbed on the particle surface recombining with an incoming H atom ($\nu_{H-H\ rec}$). With that the final form of the heat generation term due to hydrogen-particle interaction (G_2) takes the form:

$$\begin{aligned} G_2 = &(e \times 3.1\ [eV]) \times \Gamma_H^{th} \times (1-\chi) + \\ &+0.11 \times (e \times 1.41\ [eV]) \times \Gamma_H^{th} \times \chi + \\ &+0.89 \times \Big[e \times\ 3.1\ [eV] \left(\tfrac{\nu_{H\ diff}}{\nu_{H\ diff}+\nu_{H-H\ rec}}\right) + \\ &+ e \times 4.51\ [eV] \left(\tfrac{\nu_{H-H\ rec}}{\nu_{H\ diff}+\nu_{H-H\ rec}}\right)\Big] \times \Gamma_H^{th} \times \chi \end{aligned} \tag{3.24}$$

3.2.5.3 H diffusion frequency on H-terminated surface

According to Valipa *et al.* [81] the diffusion frequency of H on a H-terminated surface is proportional to an Arrhenius term, with a small activation energy of 0.1 $[eV]$, representing the diffusion coefficient divided by the square of the characteristic diffusion length. The diffusion length is assumed to be equal to the H-H average distance between neighboring surface atoms divided by the fraction of *un-passivated* surface sites. If the surface is perfectly passivated the diffusion length goes to infinity and the diffusion frequency goes to zero. Then $\nu_{H\ diff}$ is:

$$\nu_{H\ diff} = \frac{2.27 \times 10^{-8} \exp\left(-\frac{0.1e}{k_B T_{part}}\right)}{\left(\frac{1.48\times10^{-10}}{1-\chi}\right)^2} \tag{3.25}$$

3.2.5.4 H-H recombination on H-terminated surface

The frequency of recombination will be proportional to Γ_H and to the probability that one of such incoming H-atoms lands within a H-H bond distance from the physisorbed H atom, i.e.:

$$\nu_{H-H\ rec} = \frac{\pi(1.48 \times 10^{-10})^2}{4\pi R_p^2} \times \Gamma_H \tag{3.26}$$

With the equations provided in the previous few sections the energy balance is complete and the particle temperature resulting from Equation 3.18 can be calculated if we know the charge state of the particle and the fractional coverage of H on the particle. H-coverage is also a function of the particle temperature since thermal desorption of H-molecules is a strong function of temperature, the abstraction of H-atoms is a function of coverage and the diffusion of physisorbed H to a dangling bond is a function of temperature. It is thereby necessary to write another equation for the balance of absorbed and desorbed H atoms from the surface of the particle: at steady-state H absorption and desorption must equal each other.

3.2.5.5 H-coverage balance

$$\Gamma_H^{in} = \Gamma_H^{out} \tag{3.27}$$

Γ_H^{out} is represented by two processes, the thermal desorption of hydrogen and hydrogen abstracted from the surface by an incoming H atom:

$$\Gamma_H^{out} = 2.2 \times 10^{11} \exp\left(-\frac{1.86e}{k_B T_{part}}\right) \times \#\ occupied\ sites\ + 0.11\ \Gamma_H^{th} \times \chi \tag{3.28}$$

The number of occupied sites is equal to the total number of sites available times the coverage ratio. For the total number of sites available for H-passivation on a silicon

nano-particle of radius R_p the model used in [44] is adopted:

$$\#\ occupied\ sites = \#\ sites \times \chi = 2 \times 24.214 \times (D_p[nm])^{2.0235} \times \chi \tag{3.29}$$

where the 2 accounts for the fact that the formula was developed to evaluate the number of Si atoms facing the surface of the particle and the assumption here is that when passivated each of those atoms carries 2 hydrogen atoms. Processes that increase the number of occupied sites are due to H atoms impinging on a free site, and H atoms impinging on the occupied fraction of the surface, but then are able to migrate to a dangling bond:

$$\Gamma_H^{in} = \Gamma_H^{th} \times \left[(1-\chi) + 0.89\chi\left(\frac{\nu_{H\ diff}}{\nu_{H\ diff} + \nu_{H-H\ rec}}\right)\right] \tag{3.30}$$

The solution of the non-linear system (energy conservation, hydrogen mass conservation):

$$\begin{cases} G - L = 0 \\ \Gamma_H^{in} - \Gamma_H^{out} = 0 \end{cases}$$

gives us the value of the particle temperature and particle fractional H-coverage for a plasma with given parameters.

3.3 Results and Discussion

Figures 3.13 and 3.14 show the effect of ion and hydrogen radical densities on respectively nanoparticle temperature and hydrogen coverage. The simulation applies for a nanoparticle of 10 nm in diameter, in an argon plasma with electron temperature of 3 eV, room temperature for the heavy species (i.e. 300 K), and 200 Pa of pressure. The effect on temperature is fairly straight-forward. Larger densities of ions and radicals provide higher energy fluxes for the particle and result in an average higher

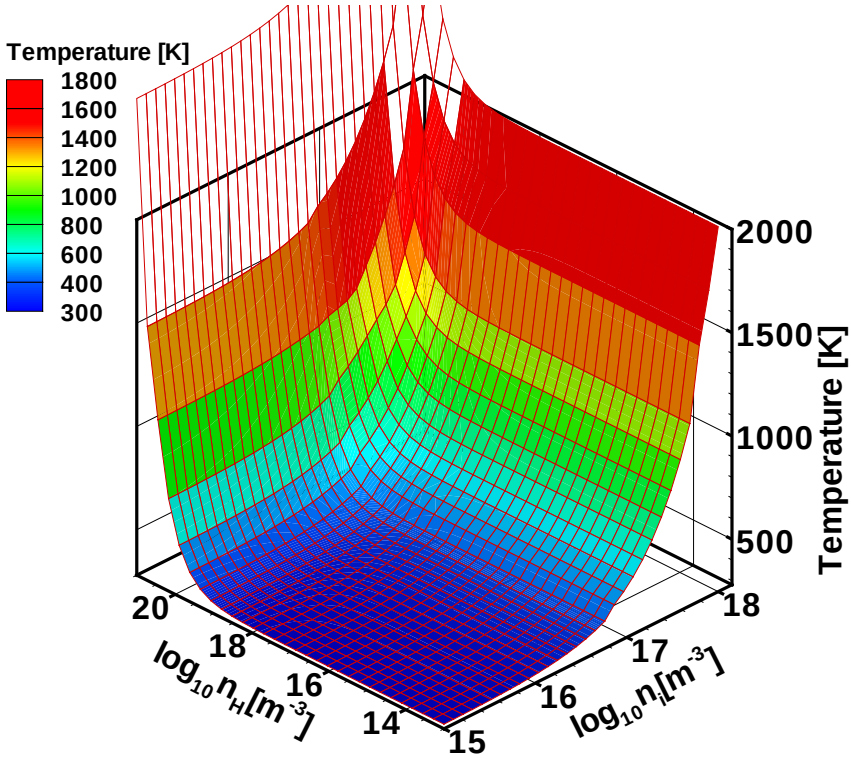

Figure 3.13: Parametric study of the effects of ion density and hydrogen radical density on the temperature of a 10 nm particle (diameter) in argon plasma, T_e= 3 eV, room temperature (300 K) at 200 Pa of pressure. ($n_i = 1 \times 10^{15} - 1 \times 10^{15} m^{-3}$ and $n_H = 1 \times 10^{13} - 1 \times 10^{21} m^{-3}$)

temperature.

For densities that are typical in the experiments, the hydrogen coverage is usually 100%. At large ion densities and high nanoparticle temperatures thermal desorption of hydrogen starts to play a role and the effects on hydrogen coverage show a non-monotonic dependence on hydrogen radical concentration: at low hydrogen radical densities the flux of radical to the surface of the nanoparticle in not sufficient to compensate the desorption, resulting in a deviation from full coverage; at larger hydrogen radical densities, the flux of hydrogen radicals is higher and contributes to enhance temperature and thermal desorption, also resulting in a reduced ion coverage.

In Figure 3.15 results show that since the ion current is not directly proportional to

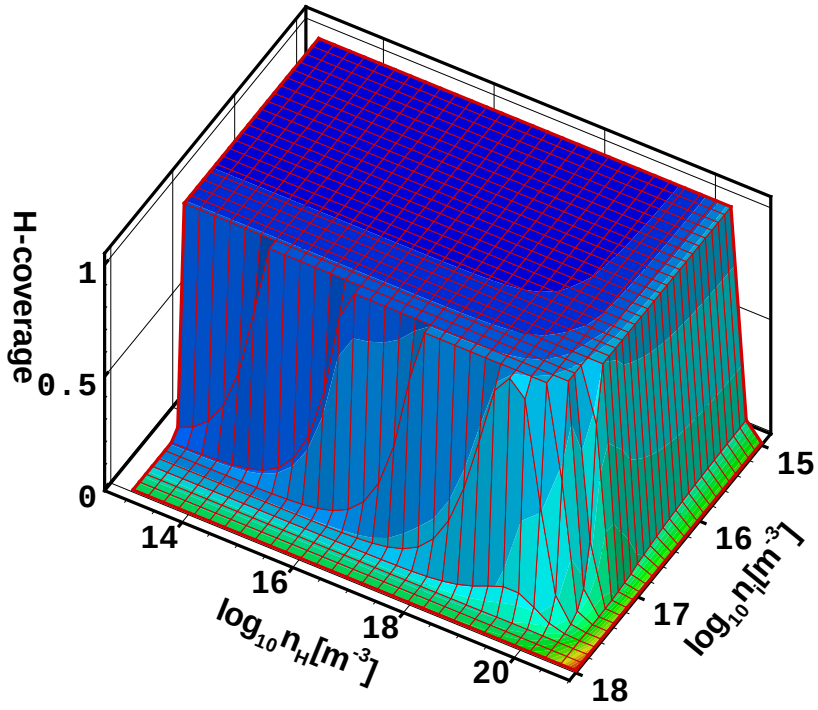

Figure 3.14: Parametric study of the effects of ion density and hydrogen radical density on the hydrogen coverage of a 10 nm particle (diameter) in argon plasma, T_e= 3 eV, room temperature (300 K) at 200 Pa of pressure. ($n_i = 1 \times 10^{15} - 1 \times 10^{15} m^{-3}$ and $n_H = 1 \times 10^{13} - 1 \times 10^{21} m^{-3}$)

the particle surface area for plasmas of moderate pressure (1 Torr here), the overall heating-cooling balance also exhibits a size-dependence.

The charging model and the heating model were also applied to the process used by Anthony *et al.* in [68] to produce nanoparticles from a single-step continuous flow nonthermal plasma. In that experiment argon (between 25 and 100 sccm) and silane (5% in helium, 13.8 sccm) were flown at a pressure of 1.4 Torr through a 10 mm quartz tube while an RF plasma was applied from an electrode surrounding the tube.

Solution of the energy/hydrogen coverage balances required the knowledge of three parameters: ion density, atomic hydrogen density, and electron temperature. The ion density measurement in the discharge has been found using an electrostatic capacitive

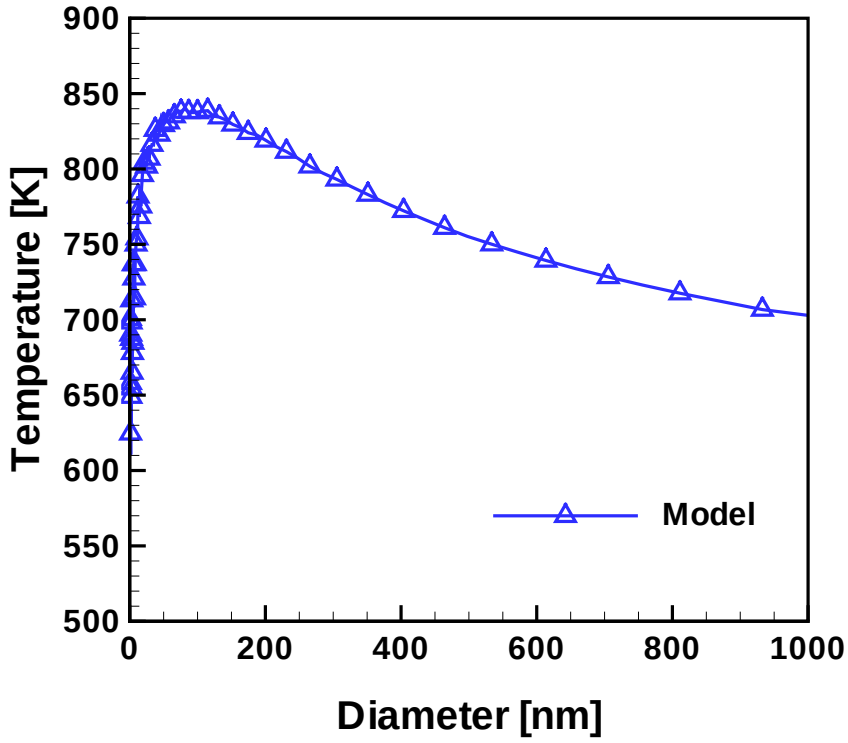

Figure 3.15: Temperature vs. particle diameter, Argon plasma, $T_e = 3\ eV$, $n_e = n_i = 1 \times 10^{16}\ m^{-3}$, $p = 1\ Torr$, $n_H = 2 \times 10^{19}\ m^{-3}$

probe. Details of this technique can be found in [82] and an ion density of $5 \times 10^{10} cm^{-3}$ was measured under the typical conditions used to produce silicon nanocrystals at 50 W of plasma power. A linear dependence between plasma power and ion density is considered in the solution of the particle energy balance for different plasma powers.

For measuring the atomic hydrogen density Mangolini used a corona model interpreting the discharge emission spectrum where the main assumption was that excited states are populated via electron-impact excitation from the ground state and de-populated by radiative de-excitation. Metastable density is negligible and not included in the model based on the results of optical absorption measurements. A density of hydrogen radicals of $2 \times 10^{13}\text{cm}^{-3}$ was measured and it is used regardless of plasma power applied.

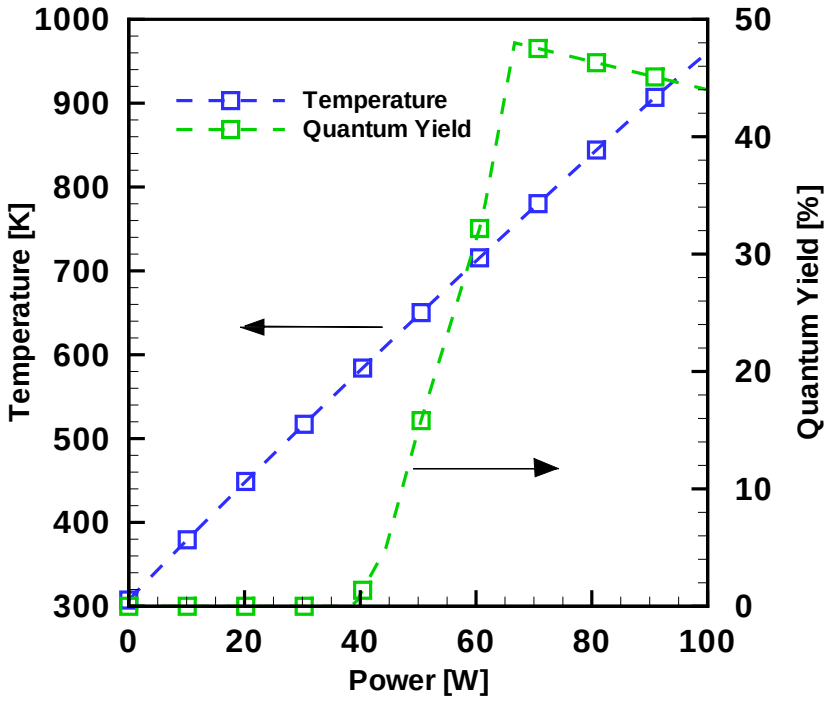

Figure 3.16: Particle temperature (model) and quantum yield (measured) Vs. plasma power in Argon plasma, $T_e = 3eV$, $T_i = 400K$, $n_H = 1.7 \times 10^{19} m^{-3}$, $n_p = 2 \times 10^{14} m^{-3}$.

An electron temperature of 4 eV was used in the computation, in agreement with the value estimated by Mangolini [14]. Ion/background gas/hydrogen radical temperature is 400 K and pressure is 1 Torr (133 Pa).

The crystalline nature of the particle is an indirect proof that particles experience a high temperature while residing in the plasma and it is necessary for the photo-luminescence. This allowed us to correlate a nanoparticle degree of crystallinity to the measurement of their luminescence yield resulting from illuminating the particle samples with a UV-light source.

In Figure 3.16 the blue line shows the result of the heating model while the green line shows the percentage of quantum yield (ratio between the number of photons

emitted by an ensamble of particles and the number of photons impinging on the sample itself). The result clearly shows that particles start to emit only when they are produced at a plasma power such that the heating model predicts the particles to reach a temperature of more than 700 K within the plasma. This is in excellent agreement with what Hirasawa *et al.* [56] presented in their paper about size dependent crystallization of silicon nanoparticles where laser ablated, thermally annealed silicon nanoparticle in the 6-8 nm size range showed full crystallization for a temperature between 700 and 850 K.

3.4 Conclusion

In this chapter we presented a simple model describing the charging, charge distribution, coagulation, and heating of nanoparticles in low-temperature plasmas. The charging model covers a wide range of ion-neutral collisionality from the collisionless OML regime to the highly collisional hydrodynamic regime and is based on the concept of a capture radius for ions. The heating model includes the effects of ion recombination and a series of hydrogen radical interactions on the surface of the particles as well as heat conduction to the background gas atoms. The results show an average charge that is less negative than the OML prediction. While the coagulation rate is not affected by the reduced charging an enhanced ion current to the particles increases the energy exchange between plasma and nanoparticles. As a result the average particle temperature is often hundreds of degrees above room temperature. These temperatures are compatible with morphology changes and nanoparticle crystallization. Results of experiments designed to support the insight given by the theoretical model are also reported. The insight that it is possible to modify the nanoparticles morphology as a function of the power input was further exploited. The next chapter presents results of two experiments that support this.

Chapter 4

Particle Crystallization

4.1 Introduction

In the the previous chapter it was shown that there is some evidence that the structure of the produced silicon particles, amorphous or crystalline, depends on the power input to the plasma. Moreover, a simple model relating power input, ion density, and resulting crystallinity was reported. In this chapter we report two other experiments that were used to directly investigate the effect of plasma properties on the nanoparticles structure.

4.2 Two-steps crystallization

The first experiment presented answers the question as to whether or not crystalline nanoparticle require to be nucleated and grown in a crystalline phase of whether the crystallization can take place in a second step, after the nucleation and growth phases are completed.

For this experiment a "batch-type" reactor is used. The reactor consists of a glass cylinder 150 mm inner diameter and 120 mm tall that features 4 inlet ports placed on the circumference half-way along the height of the cylinder and at 90 ° intervals

radially. There are three 3/8" ports used for gas introduction, pressure measurement and electrostatic diagnostics and a 1" port used for gas outlet. On the outlet port a 1.3 mm orifice is mounted 1.5 inches away from stage where glass slides can be mounted. This stage is used for the collection of nanoparticles produced in the experiments in order to then measure the properties of the produced materials via transmission electron microscopy, x-rays diffractometry and Raman spectroscopy.

The reactor is closed at both extremities by two aluminuum disks that act as powered and grounded electrodes and feature grooves and O-rings that provide an excellent vacuum-sealing of the reactor from the atmospheric environment. The inter-electrode distance coincides with the cylinder height and is hence 120 mm.

Before an experiment is performed the chamber is fully evacuated to its base pressure and then filled with a predetermined composition of gases (flowing 1 sccm of argon and 1 sccm of SiH_4/He) up to a well defined pressure (p=600 mTorr). The chamber is then closed from input and output by valves, the experiments performed and the reacted gases evacuated from the chamber output. The nanoparticles produced are impacted on a glass slide while the residual gases are evacuated, by using an impaction orifice.

To generate the plasma, the signal from a sinusoidal-wave generator is fed to a RF power amplifier, sent through a matching network, and finally to the powered top-electrode. A simple code was written to modulate the amplitude of the initial RF signal in a way to provide power to the reactor in a well-prescribed way:

- for each experiment an initial low-power (5 W) plasma is generated for 10 s. In this initial phase, SiH_4 is broken down and nanoparticles nucleated and grow. The time for this phase was decided based on the requirement of full conversion of silane into nanoparticles (and silicon film on the surface of the

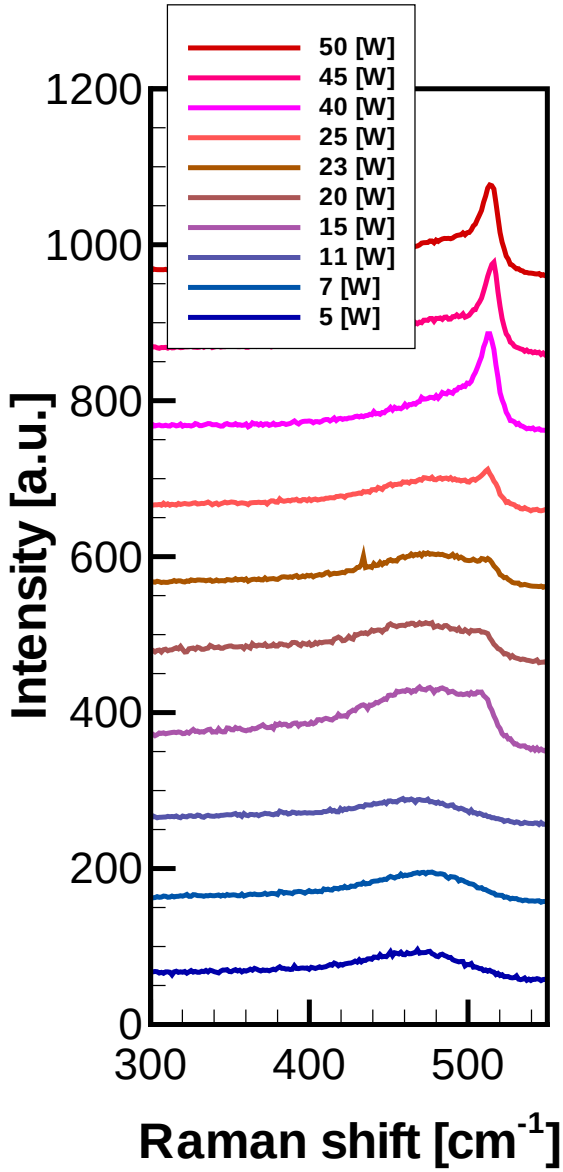

Figure 4.1: Results of Raman spectroscopy measurement for particle produced in the batch reactor.

reactor). Residual gas measurements, for these gas pressure and composition, were performed and showed that silane is in fact fully depleted after 10 s of plasma.

- a high-power phase, with a power coupled varying between 5 and 50 W (applied also for 10 s), followed the initial nucleation and growth phase. The purpose of this phase was to prove that in fact that nanoparticles can be nucleate and grown in one step and crystallized only in a second.

Results of this experiment are shown in Figure 4.1. Raman spectroscopy is used to qualitatively characterize the crystalline content of the samples of nanoparticles collected from a series of experiments in which the only parameter that was changed was the power coupled to the second phase of the plasma application.

It is clear from these results that, in this specific configuration, a power of 20 or more watts is necessary to allow nanoparticles to turn crystalline.

This proves the argument that silicon nanoparticles can be nucleated/grown and crystallized in two different steps.

4.3 Square wave modulated plasma

In this section we describe a method to produce finely intermixed films of amorphous and crystalline silicon nanoparticles with a prescribed crystalline content.

The process is based on the production of nanoparticles in a low-pressure flow-through plasma reactor. The plasma is generated by an amplified radio-frequency signal at 13.56 MHz, whose amplitude is modulated by a square wave with adjustable amplitude, frequency, and duty cycle. An indicative representation of the signal modulating

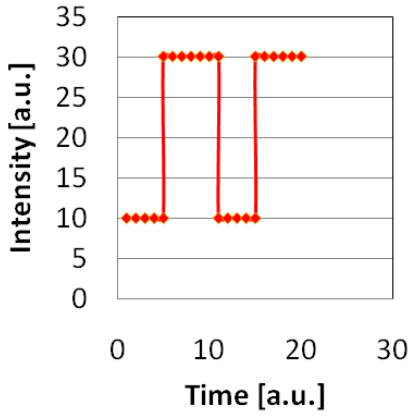

Figure 4.2: Time steps for the modulation

signal is given in Figure 4.2. The process presented is possible if:

$$\tau_{residence} << min[\tau_{SW,up}, \tau_{SW,down}], max[\tau_{SW,up}, \tau_{SW,down}] << \tau_{deposition} \tag{4.1}$$

where $\tau_{residence}$ is the residence time of the flow in the plasma tube, $\tau_{SW,up}$ is the width in time for the high-value in the square wave, while $\tau_{SW,down}$ is the width in time for the low-value in the square wave, and $\tau_{deposition}$ is the overall deposition time for each experiment.

The residence time in the plasma tube is a function of the geometry, flow-rates, and the pressure in the system. For this specific experiment, the typical residence time was about 120 ms.

$\tau_{SW,up}$ and $\tau_{SW,down}$ were set to be above 250 ms, and never exceeded 2,250 ms. Table 4.1 reports the conditions used for the results presented in Figure 4.3.

The major point of the process that makes it a suitable method to produce % resolution amorphous-crystalline composition samples is the fact that the duty cycle of the square wave directly relates to the crystalline content of the resulting film produced.

4.3.1 Experiment details

Silicon nanoparticles were produced through a 1.3 mm (diameter) orifice on a glass slide sitting 1.5" from the orifice. Plasma was obtained in 0.8" (inner diameter) glass tube under a continuous flow of 10 sccm of argon and 8 sccm of SiH_4/He (5%-95%), at a total pressure of 1460 mTorr. The nominal powers coupled to the plasma are 50 W and 200 W, respectively for the low-power/amorphous and high-power/crystalline semi-cycle. Finely intermixed samples with prescribed amorphous/crystalline concentrations are obtained (see Figure 4.3): in Raman spectroscopy the broad peak at 480 cm^{-1} is representative of amorphous silicon while the sharp peak at 515 cm^{-1} is representative of crystalline silicon.

4.3.2 Discussion

While Figure 4.3 indicates clearly that the production of amorphous-crystalline films of nanoparticles is achieved, and that the increase in real crystalline content with nominal crystalline content is monotonic and linear, it is important to point out that even at the 100% nominal crystalline content the "real" crystalline content, calcuted from the fitting of the Raman peaks according to the method presented in [83] reaches only a value of about 66%. This is, however, consistent with the fact that Raman measurement of the crystalline content of a material is a "volume" measurement, hence sensitive to the presence of amorphous shells surrounding the individual nanoparticles. We can have a simple estimate of this effect from the comparison of the average nanoparticle size from the TEM measurements (top of Figure 4.4) with the average crystallite size measurement from the x-ray diffraction measurement (bottom of Figure 4.4). Nanoparticles with average size of 12 nm have an 10.8 nm average crystalline core. This results in an amorphous "shell" with thickness of 0.6 nm, that however accounts for 37% of the volume of the nanoparticle. As a result of this consideration it is clear that the less-than-fully crystalline signature of the Raman spectra is the

Table 4.1: Conditions used to obtain results presented in Figure 4.3.

Experiment	*Pressure [mTorr]*	Nominal Crystallinity	$\tau_{SW,up}$ [ms]	$\tau_{SW,down}$ [ms]
1	1460	0%	0	∞
2	1460	10%	250	2250
3	1460	20%	250	1000
4	1460	30%	300	700
5	1460	40%	400	600
6	1460	50%	500	500
7	1460	60%	600	400
8	1460	70%	700	300
9	1460	80%	1000	250
10	1460	90%	2250	250
11	1460	100%	∞	0

result of size-dependent effects, and that in the 100% nominal crystallinity case, all nanoparticles have a crystalline core.

4.4 Conclusions

In this brief chapter we presented experimental results that show how the power coupled to the plasma and, as a related consequence, the density of ions and reactive species in the plasma, are the parameters that controls the crystallinity of plasma-produced silicon nanoparticles.

A very simple process that allows the production of silicon nanoparticle films with arbitrary amorphous-crystalline composition was develped and presented.

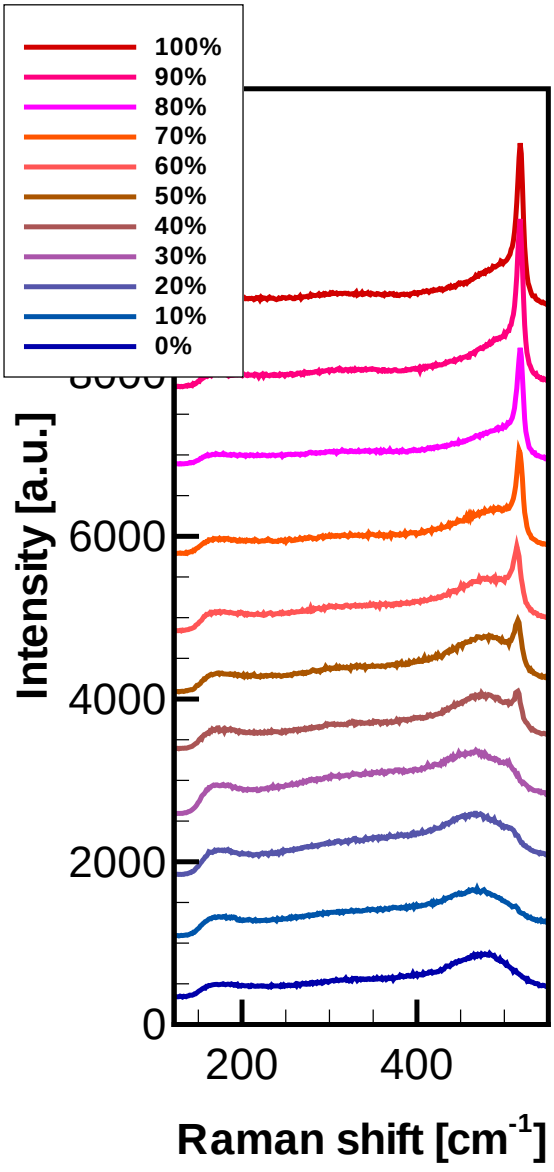

Figure 4.3: Results of Raman spectroscopy measurement for particle films produced with the square-wave modulation method.

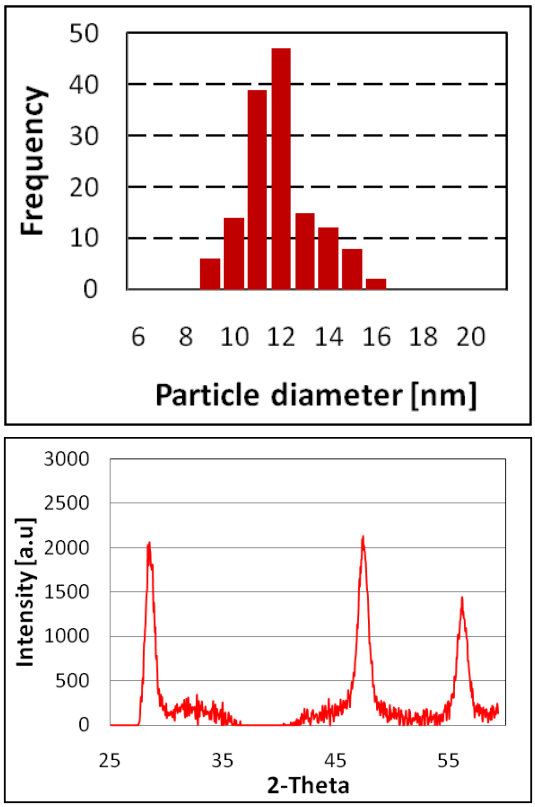

Figure 4.4: Particle size histogram (top) from TEM (transmission electron microscopy). The average particel size is 12 nm. X-ray diffraction spectrum (bottom) of the material produced. The peaks correspond to crystalline silicon and the peak broadening indicates an average crystallite size of 10.8 nm.

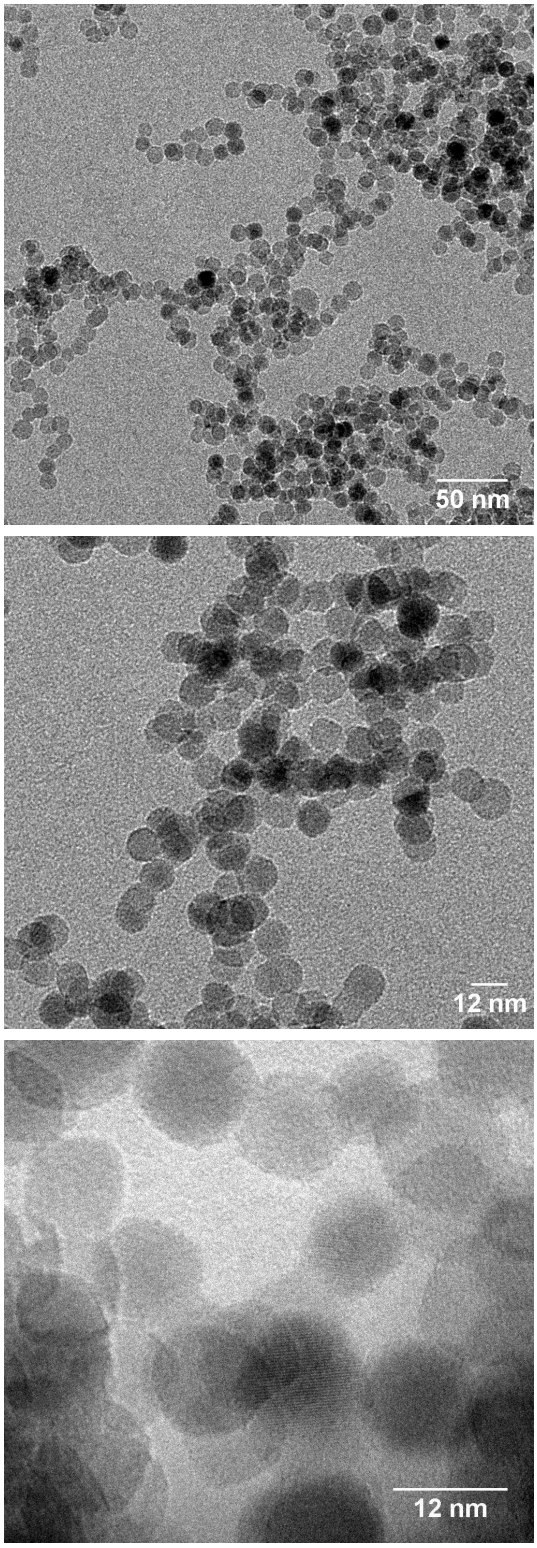

Figure 4.5: Transmission electron microscopy of silicon nanoparticles. The TEM grid was exposed to the flow of nanoparticles for about 1 s. The sparsity of the deposition over this timescale indicates that the films produced comprise alternating sub-monolayers of crystalline and amorphous particles.

Chapter 5

The energy distribution function of ions impinging on nanoparticles in a collisional low-pressure plasma

5.1 Introduction

In this chapter we address the question of how charge-exchange and momentum transfer collisions affect the energy distribution of ions impacting on the nanoparticle surface.

Previous chapters covered the effect of such collisions on the charging of nanoparticles and the implications this has on the energy transfer between plasma and nanoparticles: an enhanced ion flux and the release of ionization energy through ion-electron recombination at the particle surface increase the particle temperature hundreds of degrees above room temperature, at levels that allow crystallization.

The main result of this chapter is to show that not only charge-exchange and momentum trasfer collisions enhance the ion and energy flux to the surface of the particles, but also reduce the momentum and direct kinetic energy transfer to the species present on the surface of the growing particle. This fact can have important repercussions

for the final quality of the nanomaterials produced in low-pressure plasmas as the enhanced heating and reduced surface sputtering resulting from this model are likely to favour the growth of high-quality, low-defect crystalline materials.

Furthermore we believe it is not a coincidence that the experimental methods routinely used to produce nanoparticles from low-pressure plasma operate in a range of pressures (1-10 Torr) where, according to the model developed in this chapter, both heating enhancement and average ion kinetic energy reduction are maximized.

A self-consistent molecular dynamics simulation is used to calculate the ion energy distribution (IED) function of ions impinging on the surface of nanoparticles in low-pressure argon plasmas. The computation includes the effects of resonant charge exchange and elastic collisions between ions and neutrals through a Monte Carlo null-collision method and considers both Maxwellian and non-Maxwellian electron energy distributions. As predicted, results show a strong dependence of the IED on pressure.

5.2 Background

Over the last two decades radio-frequency low-pressure plasmas have been increasingly used as a medium to produce crystalline nanometer-sized semiconductor particles. The unique properties of these plasmas allow for the production of good quality nanocrystals with high yield, high degree of crystallinity and a very narrow size distribution [11, 4, 62, 35]. Dusty low-pressure plasma are complex, non-linear, non-equilibrium systems and the excellent results obtained in nanocrystal synthesis strongly rely on the complex interactions between plasma species (electrons, ions and neutrals) and the nanoparticles. Energetic electrons are capable of initiating the very fast chemical kinetics [84, 63, 85, 19]. At the same time, the mobile electrons are collected on surfaces with a greater efficiency than the colder ions. This results in

nanoparticles carrying on average a negative charge [11, 86, 87, 35, 4]. The unipolar charging of particles in the plasma prevents agglomeration and is crucial for achieving a monodisperse nanocrystal size distribution. Furthermore, the charging contributes to the creation of a local electric field that accelerates ions, increasing their flux towards the surface of the particles. Ions can carry a considerable amount of kinetic energy and, in contrast to neutrals, can enhance or induce processes such as surface species migration, displacement of surface and bulk atoms, and sputtering [88, 89]. The enhancement of the ion flux caused by the electric field and the energy exchange resulting from the ion neutralization at the surface of the particle contribute to heating [76] and favour crystallization [11, 12, 13, 14, 15].

The charging models of nanoparticles in low-pressure plasmas were developed along the lines of probe theories [32] and for a long time collisionless orbital motion limited (OML) theory was considered the state of the art [35, 4, 33, 61]. More recently, work has been done to show that the collisionless assumption made in the orbital motion limited theory is seldom correct for ions [36, 40, 49]. Even when the mean free path of ions is considerably larger than the linearized Debye length, collisions between ions and neutrals from the background gas strongly affect ion collection [34, 37, 38, 49] and the ion energy distribution (IED). While the effect of collisions on charging has now been widely studied, to our knowledge the effects of charge exchange collisions and elastic collisions between ions and neutrals on the shape of the energy distribution function of ions hitting the surface of nanoparticles has not been investigated. Since the synergistic interactions between plasma and surface species enables unique surface reactions and processes and because of the strong interest in the plasma community in understanding the effects of plasma species on the properties of the nanoparticles, this chapter studies the effects of charge-exchange and elastic collisions on the shape of the energy distribution of ions impinging on the surface of nanoparticles in low-to-intermediate pressure plasmas.

Charging models, even when they included the effects of ion-neutral collisions, never considered the effect of non-Maxwellian electron energy distributions (EEDF). It is not satisfactory to assume a Maxwellian EEDF and "a priori" speculate that the deviation from Maxwellian behaviour will not affect the result, while there is convincing evidence that the electron population in these plasmas is not in thermodynamic equilibrium. As a result, in this work both the cases of a Maxwellian and a non-Maxwellian EEDF are adopted and compared. Furthermore Chapter 7 will show that the presence of nanoparticles inherently affects the EEDFs of low-pressure plasmas, since electrons strongly interact with nanoparticles via elastic and inelastic (charging) collisions. As a result it is important to develop models that are capable of self-consistently including all the interactions between nanoparticle, ions, and electrons.

While little or no theoretical work was done in understanting the effects of pressure on the IED of ions hitting nanoparticles, the dusty plasma community is becoming very sensitive to these phenomena. For example it is well understood that the suppression of high energy ion bombardment is essential for the growth of crystalline diamond nanoparticles [90]. Morfill *et al.* reported on the 3D radio frequency chemical vapor deposition of diamond grains where the "substrate" consisted of seed particles levitated in a plasma composed of a mixture of CH_4 and H_2 [91] . They suggest that in high quality CVD diamond growth the impinging ion energy should be minimized; this was achieved by using a plasma chamber equipped with an adaptive rf electrode that creates a "spot" plasma in the region where particles are suspended, preventing their "bare" exposure to the ions streaming in the sheath.

While there are no studies of the effect of pressure and collisions on the IED in nano-dusty plasmas, strong attention has been devoted to the study of the effects of high energy ions on the morphology of amorphous and crystalline silicon thin films.

Van de Sanden's group investigated the effects of different IEDs on the growth and properties of a-Si:H (amorphous hydrogenated silicon) thin films using external rf substrate bias (ERFSB) techniques in a remote $Ar/H_2/SiH_4$ expanding thermal plasma [92, 93]. In their work they were able to distinguish between surface-induced and bulk-induced modifications as a function of the incoming ion energy: low-energy ions activate ion-surface processes that cause Si surface atoms displacement, intermediate-ion energies also cause Si bulk atoms displacement, while high-energy ions provide significant Si atom sputtering. With respect to nanoparticle-plasma interactions, this study suggests that low-energy ions may be important in reducing the defect density, and improving the overall quality of the nanocrystals produced. Since Si surface displacement is shown to be the main process responsible for improvements of the material properties, a significant nanoparticle morphology/growth modification is expected when the ratio of ions to Si atom fluxes towards the surface of the growing nanoparticle is on the order of unity and the average ion energy is smaller than the surface species binding energy, which in Si-Si and Si-H bonds is about 3 eV [94].

Low energy ion-surface interactions can readily result in an energy transfer in the form of a local thermal spike in addition to the release of the ionization energy. Van de Sanden's group proposes that Si surface atom displacement is the only ion-induced process in which the substrate temperature and ion energy are interchangeable. Similarly, we have shown in previous work that the temperature of nanoparticles in plasma is hundreds of degrees above room temperature [14, 15], a consequence of ion-neutralization and other energetic H-radical processes taking place at the surface [76, 14, 80, 79, 15].

Graves *et al.* [95, 96] performed a computational study on the interactions of energetic argon ions with silicon surface atoms using molecular dynamics simulations. In their papers it is shown how the energy and the flux of argon ions to the surface determines

the phase of a silicon substrate: high energy ions are able to destruct the crystalline order and create an amorphous layer whose depth is a function of the ion energy. The crystalline-amorphous interface acts as a phase boundary and upon reducing the energy of the impinging ions the damage caused to the substrate can be reversed as the interface moves towards the surface of the substrate: low energy ions "heal" the damage caused by high energy ions.

As there is now significant interest in understanding the mechanisms that lead to nanocrystal formation in plasmas, it appears imperative to understand the formation of the IED of ions hitting nanoparticles suspended in a plasma. This is the topic of this chapter. The studies presented here are a first step towards understanding the detailed plasma-nanoparticle interactions that lead to the formation of nanocrystals.

5.3 Description of the simulation

In this study, we used a self-consistent molecular dynamics simulation similar to the one developed by Gatti and Kortshagen [49] to investigate the ion energy distribution function of ions reaching the surface of nanoparticles in low-pressure argon plasmas. The electric field and the potential profile around the particle is not prescribed but results from the integration of the Poisson equation over the charge distribution present at each moment in time in the space surrounding the particle. The simulation assumes spherical symmetry around the particle and is one-dimensional. Total energy and angular momentum of each ion are conserved between collisions. For details the reader is referred to ref. [49].

Input parameters to the simulation are the pressure, the diameter of the nanoparticle, the simulation time (sufficient to obtain a good statistics for the IED), the electron temperature or the EEDF in case of a non-Maxwellian plasmas, the ion/electron density (in all cases considered here equal to $1 \times 10^{10} cm^{-3}$), the neutral/ion temperature

(300K or 0.025 eV), the ionic mass (argon), and the charge exchange and elastic collision cross-sections as a function of energy, obtained respectively from [97] and [98]. Based on this initial set of parameters a guess based on OML theory for the particle floating potential is derived. The integration time step is then calculated as the ratio between particle diameter and the maximum ion velocity achievable in a collisionless sheath with the potential predicted by the OML theory: as the nanoparticle is much smaller than the extension of the sheath around it, this definition of the time-step allows for a good resolution of the ion motion in the sheath. The linearized Debye length is calculated and a simulation cell 4 times its size is created using an logarithmically-spaced grid due to the roughly exponential dependence of the potential profile on the radial distance from the particle. At the outer boundary of the simulation domain the particle charge is fully shielded and the electric field is assumed negligible. We assume that ions entering the simulation cell have a Maxwellian energy distribution and the thermal flux and velocity distribution of these ions are calculated, based on ion density, ion temperature, and domain size. The timing with which ions need to be introduced in the simulation cell is also calculated and implemented. The domain is then filled with ions at the prescribed density and initially at room temperature.

For all ions in the simulation domain, a continuously updated record is kept of ion positions, velocities, angular momenti and collision times. The collision times are calculated from the maximum collision frequency as a function of energy. When the simulation time matches the collision time for a given ion, a null-collision Monte Carlo method [99] is adopted to determine the nature of the collision (real or null) and a new collision time is calculated. This approach allows for a collision dynamics that is consistent with the dependence on energy of the collision cross sections: the relative velocity between the ion and a potential neutral collision target is used. In the event of a real collision, the ion velocity and angular momentum are updated: in a charge exchange collision a stochastic neutral velocity and angular momentum are assigned

to the ion, with neutral gas atoms assumed to follow a Maxwellian distribution. In the event of an elastic collision, random collision angles are generated and the new ion properties are calculated, assuming the scattering to be isotropic. These collisions can affect both the electric field around the particle and more generally the energy of ions reaching the surface of the nanoparticle.

An initial guess of the potential profile is made based on a shielded Yukawa potential, that allows for the initial estimate of the electric field around the particle and the acceleration imposed to the initial ion population (resulting from the combination of the electric field and a pseudo-potential component due to the conservation of angular momentum [49, 36]). At the same time, assuming that the nanoparticle has the electric capacitance of spheres, the initial particle charge is calculated. The trajectories of the ions are then integrated in the next time step with a velocity Verlet algorithm [100, 101]. After an initial relaxation time in which the charge on the particle is fixed and ions are accelerated in the prescribed field the simulation switches to a full self-consistent mode. The ions that leave the simulation cell through impacting on the particle surface contribute to the particle charge and their impaction velocities are registered. A histogram of collection frequencies against impact energy is created and updated for each charging event.

Electrons have a much smaller mass and a much larger velocity; it would be impracticle to treat the individual motion of electrons as it is done for the ions. Hence, a continuum approach is adopted for the electron charging. The electron fluxes to the nanoparticle are derived from OML theory both in the case of a Maxwellian and a non-Maxwellian plasma, since electron-neutral collisions are infrequent and not efficient in affecting the nanoparticle charging:

$$\Gamma_{e,Max} = \pi a^2 n_{e,\infty} v_{th,e} \exp\left(\frac{eV_p}{kT_e}\right) \tag{5.1}$$

$$\Gamma_{e,non-Max} = \pi a^2 n_{e,\infty} \int_{-V_p}^{\infty} \left(1 + \frac{V_p}{\epsilon}\right) \sqrt{\frac{2e\epsilon}{m_e}} f_0(\epsilon) \sqrt{\epsilon} d\epsilon \tag{5.2}$$

Here Γ_e is the electron flux, a is the particle radius, $n_{e,\infty}$ the unperturbed electron density, v_{th} the electron thermal velocity, V_p the particle floating potential, T_e the electron temperature, e the elementary charge, k the Boltzmann factor, m_e is the electron mass, f_0 is the electron energy probability function, and ϵ the electron kinetic energy. The charge is updated only when the electron flux integrated over the simulation time reaches integer values, accounting for the quantized nature of the electron charge.

Finally the model calculates the electric field around the particle by integration of the Poisson equation, using a trapezoidal scheme. Boundary conditions for this calculation are the particle floating potential resulting from the charge carried by the particle and a vanishing electric field at the far edge of the simulation cell. The ion density is integrated from the momentary ion distribution while the electron density profile depends directly on the potential profile both in the Maxwellian and non-Maxwellian case:

$$n_{e,Max}(r) = n_{e,\infty} \exp\left(\frac{eV(r)}{kT_e}\right) \tag{5.3}$$

$$n_{e,non-Max}(r) = n_{e,\infty} \int_{-V(r)}^{\infty} f_o(\epsilon) \sqrt{\epsilon} d\epsilon \tag{5.4}$$

Here $V(r)$ is the radial profile of the electric potential. As the electron density and the electric potential depend on each other an iterative approach is adopted to find their self-consistent profiles. The calculations of ion trajectories, collisions, charging and electric field are repeated at every time step until the simulation reaches the maximum simulation time.

Simulations were performed for a range of neutral pressures between 0.01 Pa and

50,000 Pa, for particle sizes ranging from 10 nm to 1 μm in diameter. A parametric study of the effect of electron temperature and reduced electric field was also performed. For the Maxwellian case, electron temperatures between 2 and 6 eV were used while in the case of non-Maxwellian plasmas the electron energy distribution was generated from the solution of the Boltzmann equation provided by the BOLSIG solver [102]. In this Boltzmann solver the angular dependence of the velocity distribution function is expanded for the first two terms in Legendre polynomials while the energy dependence is expanded in finite elements (cubic B-splines)[103]. The reduced electric field (E/n) used in these calculations ranged between 5 and 110 Td (10^{-17} $V\times\text{cm}^2$).

5.4 Results

A comparison between simulations for Maxwellian and non-Maxwellian plasmas suggests that there is not a strong difference between the two. Plasmas with the same "effective" electron temperature show similar behaviours (within a few percents) in terms of particle charging, ion flux and IED. Figure 5.1 reports for a 500 nm particle the IEDFs in the case of Maxwellian or non-Maxwellian plasmas over a pressure range between 1 - 1,000 Pa. The reason for this similar behaviour lies in the similarities between the EEDFs for the Maxwellian and non-Maxwellian case at electron energies below the particle floating potential. In low-pressure argon plasmas the EEDFs strongly deviate from the Maxwellian behaviour at electron energies above the thresholds for inelastic processes (excitation and ionization). These differences would affect processes that require large electron energies but, since Equation 5.4 integrates EEDFs from electron energies equal to or smaller than the absolute value of the negative particle floating potential, differences at higher energies have an overall negligible effect.

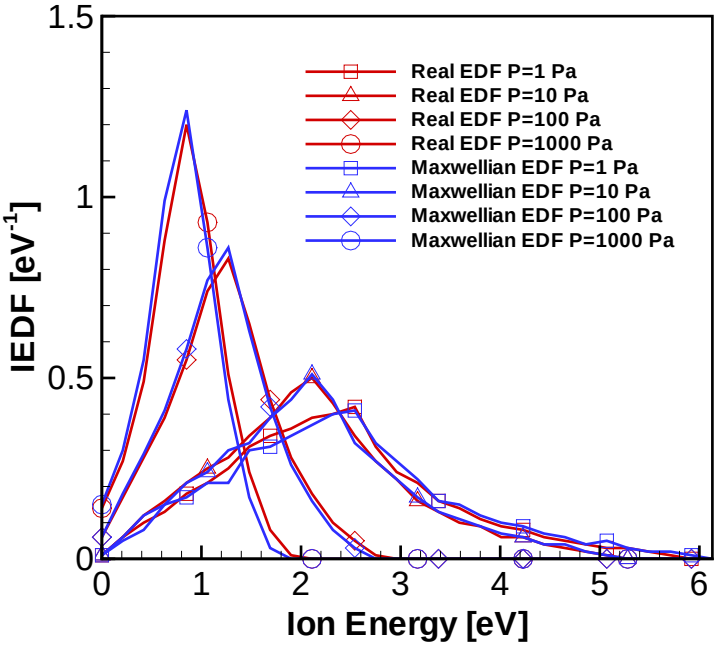

Figure 5.1: Results of simulations for the IED for 500 nm particles, comparing Maxwellian and non-Maxwellian argon plasmas, E/n = 30 Td, $n_i = 1 \times 10^{16}$ m^{-3}, an effective electron temperature of $T_e = 3.79$ eV, pressure range p = 1 Pa-1,000 Pa. The nature of the electron energy distribution (Maxwellian or non-Maxwellian), has negligible effects on the resulting IED.

The effect of charge exchange and elastic collisions between ions and neutrals on the IED, as a function of pressure, is presented in Figure 5.2 for nanoparticles of 500 nm in diameter in a non-Maxwellian argon plasma. It is evident from the results that the pressure plays a major role in the formation o of the IED. For small pressures ($p < 100$ Pa) there is a considerable fraction of ions with energies above the binding energy for Si-Si and Si-H surface species. At larger pressures (100 Pa$< P <$ 1000 Pa) collisions are very effective in reducing the average energy of ions impinging on the nanoparticle. The reason for this is two-fold: the increasing frequency of collisions does not allow ions to gain the maximum energy as determined by the plasma-nanoparticle potential difference in the sheath. Furthermore, collisions frequently involve ions that for their combination of kinetic energy and angular momentum would be destined to miss the particle surface [49]; however, due to charge-exchange collisions these ions reach the

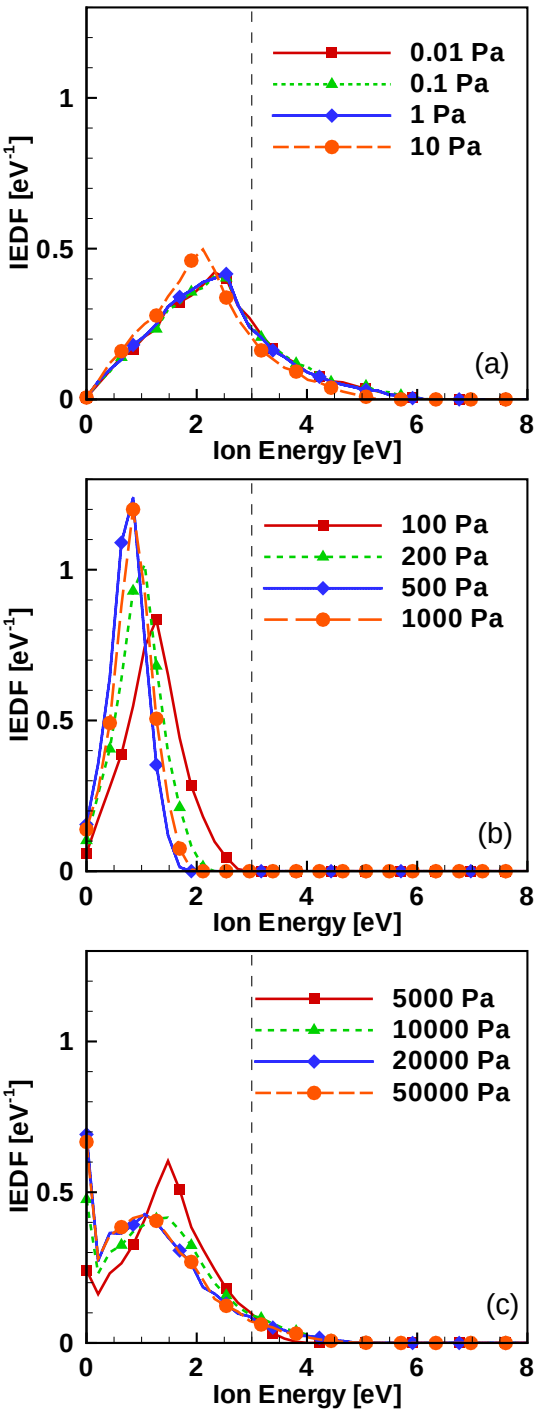

Figure 5.2: Results of simulations for the IED for 500 nm particles in a non-Maxwellian argon plasma, E/n = 30 Td, $n_i = 1 \times 10^{16}$ m^{-3}, an effective electron temperature of $T_e = 3.79$ eV, pressure range p = 0.01 Pa-50,000 Pa. The dotted vertical line at 3 eV is a guide to the eye for the binding energy of Si-Si and Si-H near-surface bonds.

nanoparticle surface. This enhancement of the ion flux contributes to lowering the particle floating potential, resulting in a lower energy available for the ions reaching the particle. At even larger pressures of $1,000$ Pa$< P < 50,000$ Pa a different regime appears: the more frequent collisions significantly reduce the flux of ions to the nanoparticle surface, a phenomenon well known in the hydrodynamic regime of probe theory. This results in a larger particle floating potential and a shift in the average ion energy towards larger energies. A non-negligible fraction of ions undergoes a collision when in very close proximity to the particle surface, resulting in a feature in the IED at the lowest energy value in the histogram. As a result, for this particle size in this pressure range, the mode and average value for the energy in the IED can differ considerably.

Figure 5.3 shows results for the simulation for a particle of 50 nm in diameter, this time for a Maxwellian plasma. In spite of a considerably larger simulation time, the much smaller collection area for the particle and the broader IED due to the higher electron temperature result in a noisy sampling of the IED at low pressures, a consequence of the stochastic nature of charging. As in the case for the 500 nm particle, it is possible to find a range of pressures where the average ion energy is strongly reduced and the ion flux is enhanced, due to the combined effect of collisions and the reduction of the particle floating potential. At smaller particle sizes this range appears at larger pressures of $P \approx 200 - 10,000$ Pa.

Figure 5.4 summarizes the finding reported so far. It shows the average, the mode, and the standard deviation for the IED as well as the predicted flux for the 500 nm and the 50 nm nanoparticle diameter, respectively. It is quite remarkable that in the 50 nm case the flux increases by a factor of 5 while the average energy drops from a value of about 4 eV to a value of 0.2 eV (a 20-fold reduction). It is worth noticing that literature reports of production of the best quality semiconductor nanocrystals from

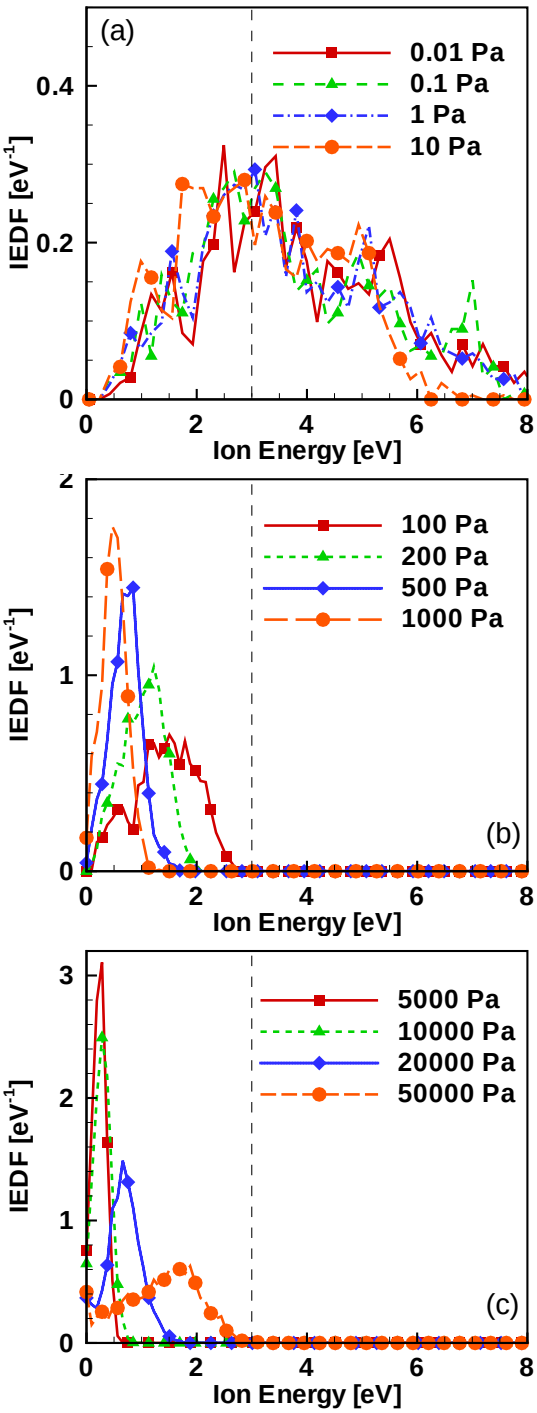

Figure 5.3: Results of simulations of the IED for 50 nm particles in a Maxwellian argon plasma, T_e=6 eV, $n_i = 1 \times 10^{16}$ m^{-3}, pressure range p = 0.01 Pa-50,000 Pa. At low-pressures the rather broad distribution and the small number of charging collisions due to the small size of the particles contribute to the apparent noise.

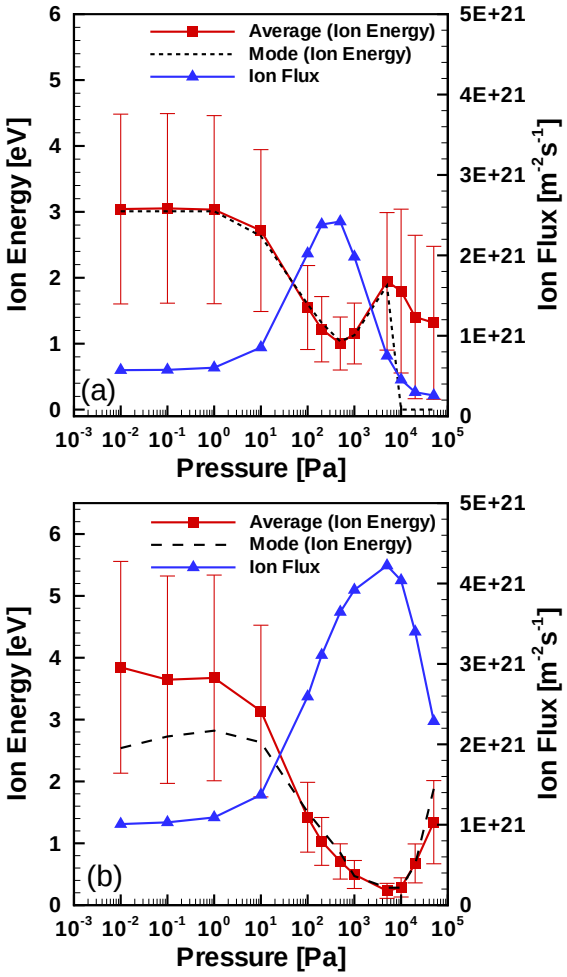

Figure 5.4: Ion flux and the average, the mode and the standard deviation (represented by error bars) for the energy of ions impinging on a 500 nm particle (a) and a 50 nm particle (b). Plasma parameters are as reported in Figures 5.2 and 5.3. Notice the dramatic reduction in both the average ion energy and the standard deviation and the concurrent increase in the total flux taking place in the range of pressures commonly used for the synthesis of nano-crystalline materials in low-pressure dusty plasmas.

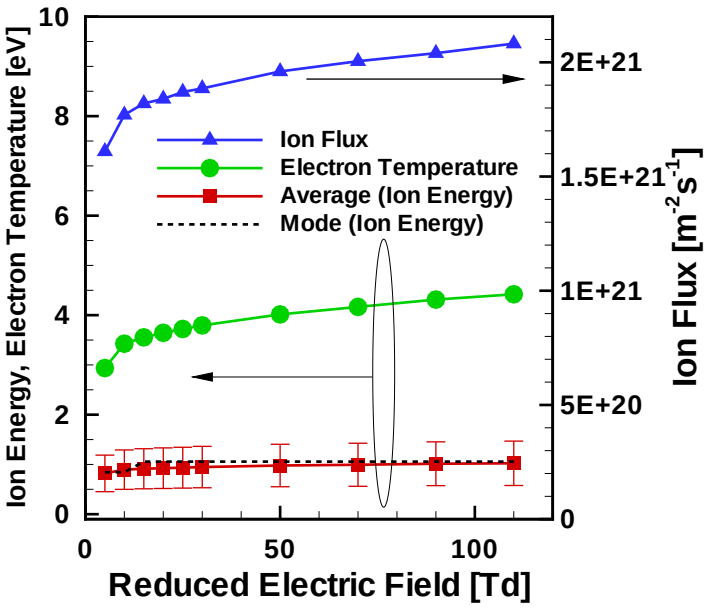

Figure 5.5: Effect of reduced electric field (and effective electron temperature) on the energy of ions impinging on a 500 nm particle in a non -Maxwellian argon plasma at 200 Pa of pressure and an ion density of $n_i = 1 \times 10^{16}$ m^{-3}, in terms of average, mode, and standard deviation for the energy and total ion flux.

low-pressure plasmas use pressures that, according to our present results, coincide with an enhanced ion flux and a reduced ion energy [11, 12, 67].

In Figure 5.5 we report the results of a parametric study on the effects of reduced electric field and the electron energy on the IED. While pressure is easily adjustable in experiments, the electron temperature adjust in a self-consistent manner as determined by parameters such as pressure, plasma composition, reactor geometry, and others. Furthermore, as we see from the results, the modifications of the IED due to changes in the electron temperature are not significative. Larger electron energies provide a slighlty larger ion flux and average ion energy, but the changes are on the order of $\approx 10\%$.

Mangolini *et al.* [12] reported a method for the production of silicon nanoparticles

where the plasma properties were very similar to the ones adopted and investigated in this thesis. It is instructive to compare the flux of energetic ions that we estimate from this simulation with the flux of silicon atoms or elementary silane radicals (e.g. SiH_x, x=1,2,3) that contribute to the nanoparticle growth. Mangolini reported the growth of 6 nm particle in a 7 ms residence-time in the flow-through reactor. Assuming a constant diameter growth rate this yields an average growth rate of about 0.85^{-6} m s^{-1}. One monolayer of silicon atoms $\rho_{Si}^{monolayer}$ contains 7×10^{18} atoms m^{-2} in the [100] direction. As a result the monolayer spacing is $(\rho_{Si}^{monolayer})^{-1/2} = 0.377$ nm. From the growth rate and the monolayer spacing we get to an estimate of the time required to add a layer of Si atoms to a Si particle, which is 4.4×10^{-4} s. The Si atom flux to achieve this growth rate is 7×10^{18} atoms $m^{-2}/4.44 \times 10^{-4}$ s$\approx 1.6 \times 10^{22}$atoms $m^{-2}s^{-1}$. The flux of ions for the same plasma parameters is of the order of 5×10^{21}ions $m^{-2}s^{-1}$. The ratio of the ion to monomer flux is thus ≈ 0.3. This implies that under the conditions considered by Mangolini *et al.* [12] ions can provide a significant role in the reorganization of silicon species newly attached to the nanoparticle surface, which may favor the formation of high quality nanocrystals. A silicon monomer physisorbed or losely bound to the surface of a particle may suffer directly or indirectly through a neighboring atom a collision with a low-energy argon ion. The interaction with the low energy ion may allow the silicon atoms to find an energetically more favourable position on the particle surface leading to the formation of the crystalline phase. It is important that silicon atoms at the surface may experience such an interaction before a new monolayer of silicon atoms is deposited on the surface of the particle. Hence it is reasonable to assume that *under conditions when the silicon growth species and the ion flux are on the same order, the optimal effect of the ions helping with the crystallization of the silicon nanoparticles is achieved.*

5.5 Conclusions

In this chapter, we have presented the results of a molecular dynamics simulation that evaluates the effects of resonant charge exchange and elastic collisions between ions and neutrals on the ion energy distribution function of ions bombarding the surface of nanoparticles in collisional dusty plasmas in argon over a wide pressure range and both for the case of equilibrium and non-equilibrium electron populations. Results show that both the average ion energy and the total ion flux are a strong function of pressure. A minimum in the ion energy and a maximum in the ion flux appear in the same narrow range of pressures (1-10 Torr) that are routinely adopted in the production of high-quality nano-crystalline semiconductors for photovoltaics and micro-electronics applications. Under these conditions, the nanoparticles are hit by a flux of ions, whose energy is too small to break Si-Si bonds at the particle surface. However, these ions may aid the reorganization of silicon atoms at the nanoparticle surface. We find that for conditions typically used for nanocrystal formation, the fluxes of silicon growth species and of ions are on the same order of magnitude, suggesting that ions play an important role in helping Si surface species to achieve the energetically most favorable surface location. We thus suggest that the ion flux hitting the surface of the nanocrystals plays an important role in the crystallization of nanoparticles in plasmas.

Chapter 6

Power Measurement

6.1 Introduction

This chapter addresses the measurement of the exact power coupled to the plasma by measuring the current and the voltage across the plasma cell corrected for the displacement current. The technique employed here follows the indications given in [104] and [105].

In a nutshell, the measurement consists of measuring the waveforms of the voltage drop across (V_{plasma}) and the current through (I_{plasma}) the plasma volume. From these it is possible to extract the different harmonic components, via Fourier transformation of the measured data and express the measurements in terms of effective (or "real") power coupled to the plasma and plasma impedance.

V_{plasma} and I_{plasma} can be quite different from the voltage and current at the point of measurement (position where the probes are physically located): in a parallel-plates capacitively coupled plasma reactor this is primarily due to the inductance between the measurement point and the electrode, and the capacitance between the electrode and the grounded electrode or other grounded surfaces.

Such stray impedances of the reaction chamber have to be measured and character-

ized in order to single out the changes in plasma impedance due to the presence of nanoparticles. A mathematical model has been used to derive the relevant quantities from the measured ones and while such stray impedances are successfully modeled for the reactor geometry used here as a stray capacitance in parallel with an inductance, the results report the plasma impedance to be a series combination of a resistor and a capacitor.

The main result of this experiment is that the plasma impedance becomes larger in modulus and has a more resistive nature due to the presence of the particles. Furthermore, only a small fraction of the power made available by the power amplifier is coupled to the plasma. The rest is dissipated through the matching network, the cables, and through electrode heating.

Impedance measurement is a technique fairly easy to implement, *in-situ* yet non-intrusive and very sensitive even for the smallest particles; these characteristics cannot be found in any other particle diagnostic method, such as laser light scattering, Mie-ellipsometry, in situ/ex situ infrared absorption, Raman spectroscopy, mass spectrometry, SEM/TEM, x-ray diffraction, and optical spectroscopy. Scattering methods in particular do a poor job for very small particle sizes (nanometer range) as the scattered light intensity scales as the sixth power of the particle radius. Thus, more robust, simple and sensitive *in-situ* detection methods are required to monitor the formation of dust particles in the early phase. The semiconductor industry is very sensitive to these needs as it adopted impedance measurements as a qualitative method for detecting the presence of particles.

This chapter is organized as follows: in Section 6.2, the experimental set-up is described. Section 6.3 presents the electrical characterization of the discharge chamber. In Section 6.4 the experimental results of electrical measurements in argon and in $Ar/SiH_4/He$ plasmas are discussed. Finally Section 6.5 concludes the chapter.

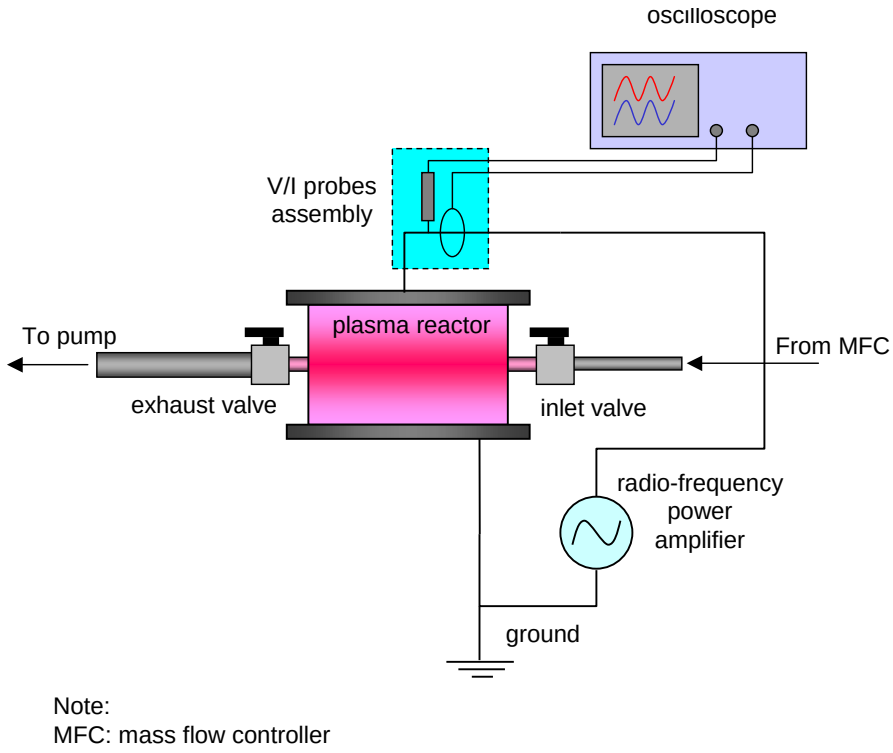

Figure 6.1: Schematic of the apparatus used for the experiments in Chapter 6

6.2 Experimental apparatus

Figure 6.1 shows a schematic of the apparatus used in this experiment. The reactor consists of a glass cylinder 150 mm inner diameter and 120 mm tall that features 4 inlet ports placed on the circumference half-way along the height of the cylinder and at 90 ° intervals radially. There are three 3/8" ports used for gas introduction, pressure measurement and electrostatic diagnostics and a 1" port used for gas outlet. The reactor is closed at both extremities by two aluminuum disks that act as powered and grounded electrodes and feature grooves and O-rings that present a vacuum-seal of the reactor from the atmospheric environment. The inter-electrode distance coincide with the cylinder height and is hence 120 mm.

To prevent the effect of re-circulation and differential residence times in the chamber, measurements are always made without a continuos flow of gas entering the chamber but with a configuration that can be defined "batch reactor": the chamber is fully

evacuated to its base pressure and then filled with a predetermined composition of gases up to a well defined pressure. The chamber is then closed from input and output by valves, the experiments performed and the reacted gases evacuated from the chamber output. While this approach has the great advantage of preventing gas residence times to affect the measurement, it requires extreme care in preventing gas leaks into the low pressure volume as all measurements are strongly affected by contaminations. The pressures investigated are 200, 400, and 600 mTorr and the plasma composition is either pure argon or Ar/He/SiH_4 with relative concentrations of 88.8%/10.5%/0.55%. Voltage and current waveforms are acquired from a custom built module comprising a voltage probe (Tektronix P6138A, bandwitdh: 400MHz, amplification: 100X, max voltage: 300V) and a current probe (Pearson Current Monitor Model 2877, sensitivity: 1V/A, max current 10A). Care was put into minimizing the stray inductance by putting both probes close to each other and close to the powered electrode. The signals from the probes are recorded with a Tektronix TDS 460A oscilloscope. The probes calibration was made against a 50 Ω "dummy" load: first the voltage and current probe readings were calibrated against the output of a function generator. Then the entire acquisition set-up (probes, cables) was calibrated over a wide-frequency range to cancel the effects of propagation delay of signal due to different measuring principles and possibly slightly different lenght of cables employed which can cause a parasitic phase delay. Finally the measuring set-up was connected at the RF electrode connection of the powered electrode. The plasma chamber was then evacuated to base pressure and the measurment of the intrinsic vacuum impedance was done as described in Section 6.3.

All the calibrations performed are included in the Matlab code that was written to perform Fourier transform of the waveform for the main harmonics present and interpret the data. The waveforms are collected at an effective sample rate of 1 GHz, each waveform comprising 2500 points. Sampling rate and number of sample points

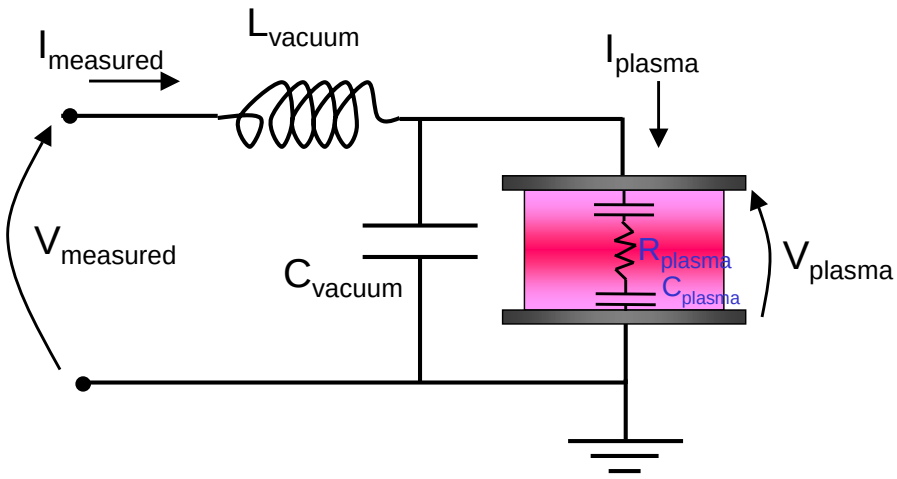

Figure 6.2: Equivalent electrical circuit of plasma chamber and power leads.

are limited by the harware used but allow good resolution in the range of frequencies between 1 and 50 MHz. The waveforms, both in the case of pristine and dusty plasma, are collected 5 sec after the plasma was ignited, allowing for particles to be fully nucleated and grown.

6.3 Equivalent electric circuit and model

A very simple model for the equivalent circuit representing with linear electrical elements the impedance of the system is presented in Figure 6.2. The choice of the geometry simplifies considerably the modeling effort: the choice of a parallel-plate geometry leads to an equivalent capacitance (C_{vacuum}) between powered electrode and ground (which comprises both the grounded electrode and any other grounded surfaces the powered electrode "sees"); the small distance between the point of measurment and the electrode but also the electrodes themselves and the lead between the "grounded" electrode and the real ground result in an equivalent inductance (L_{vacuum}). The plasma impedance itself comprises a capacitive component and a resistive component. Further details about the plasma impedance decomposition and

interpretation are presented in Section 6.4.

Analysis of the circuit shows that the n^{th} harmonic components of the complex plasma voltage $V_{pl,n}$ and current $I_{pl,n}$ are related to the n^{th} harmonic components of the measured complex voltage V_n and I_n by:

$$V_{pl,n} = V_n - j\omega_n L_{vacuum} I_n \tag{6.1}$$

and

$$I_{pl,n} = (1 - \omega_n^2 L_{vacuum} C_{vacuum}) I_n - j\omega_n C_{vacuum} V_n \tag{6.2}$$

where j is the imaginary unit, $\omega_n = n\omega$ and ω is the angular frequency at the fundamental driving frequency ($\omega = 2\pi \times 13.56\ 10^6\ rad/s$)

Most of the measured current is a displacement current, $j\omega_n C_{vacuum} V_n$, caused by the capacitance between the electrode and ground. Consequently calculating the electrode current is quite sensitive to errors in measuring V_n and I_n.

The dissipated power P is calculated from electrode voltage and current using the expression:

$$P = \sum_{n=1}^{6} 1/2 |V_{pl,n}||I_{pl,n}| cos\phi_{pl,n} \approx 1/2 |V_{pl,1}||I_{pl,1}| cos\phi_{pl,1} \tag{6.3}$$

where the product includes the moduli of current and voltage and the cosine of the phase of the voltage with respect to the current for each harmonic. The main contribution is given by the principal harmonic alone.

The values for L_{vacuum} and C_{vacuum} were determined from the measurement of impedance at 12 different frequencies (f=5,6,...,16 MHz), with a low voltage (10 V_{p-p}) signal generator exciting the empty cell (no plasma). The impedance of the empty cell,

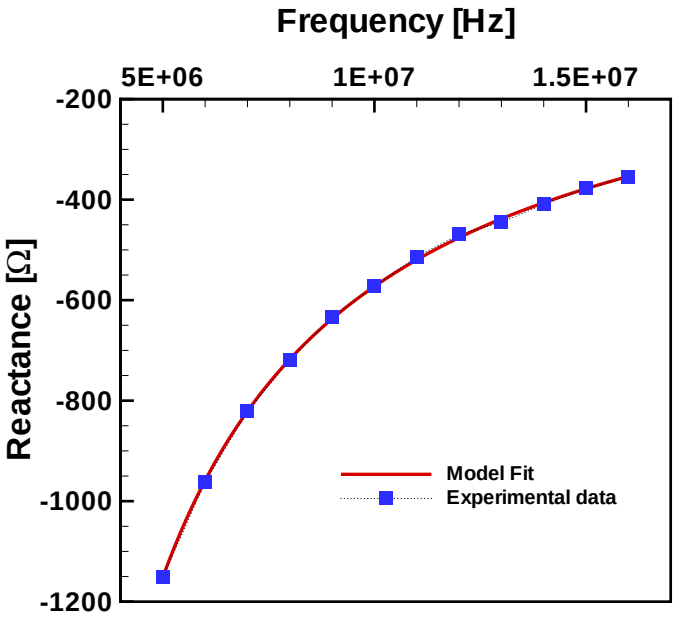

Figure 6.3: Measured vacuum reactances and model fitting as a function of signal frequency. The model assumes 2-components equivalent circuit and fits 66.3 nH vacuum inductance and a 27.6 pF vacuum capacitance.

Table 6.1: Cell Electrical Properties

Property	value	Uncertainty
C	27.6 pF	± 2 pF
L	66.3nH	± 3 nH

according to the model, contains only an imaginary component (reactance) and is:

$$Z_n = V_n/I_n = jn\omega L_{vacuum} + 1/jn\omega C_{vacuum} \tag{6.4}$$

Figure 6.3 reports the measured vacuum reactance and the fit done by the model. The real component was in fact negligible in the measurement and a remarkable agreement with a very small deviation between the measurement and the fit is obtained: since there are only two unknowns (L_{vacuum}, C_{vacuum}) and 12 equations, the system is solved in the ordinary least square sense estimating the linear regression coefficients.

Table 6.1 reports the results of the fitting and the uncertainties resulting from the

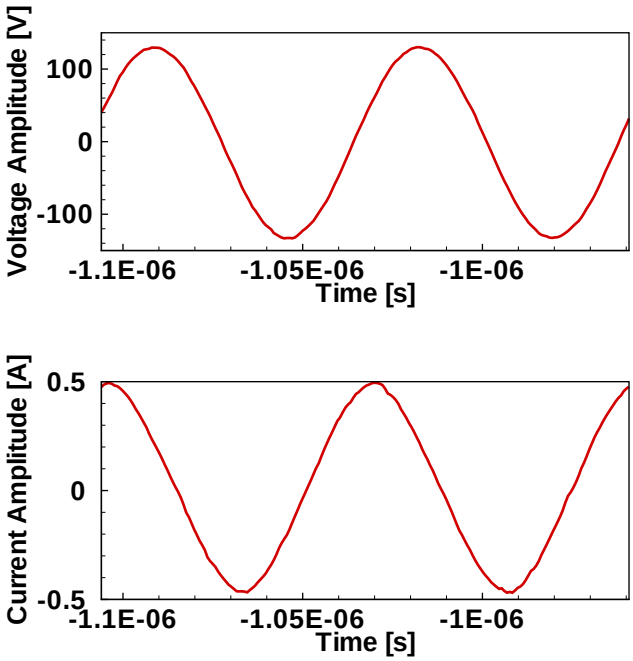

Figure 6.4: Typical voltage and current waveforms

linear regression (standard deviations), but not the uncertainties due to other sources.

With these values it is now possible to interpret I-V waveforms from the plasma and deduce the real plasma current and voltage, subtracting the displacement current and the voltage lost across distributed capacitances and inductances. This allows for a reliable measurement of the power coupled to the plasma.

Results of this measurement are presented in the next section.

6.4 Results

The discharge is operated with the upper electrode powered by a 13.56 MHz power supply (ENI A300), capacitively coupled through an impedance matching network and with the lower electrode grounded. The pressure investigated is in the range between 200 and 600 mTorr. The input power is varied between 20 and 160 W.

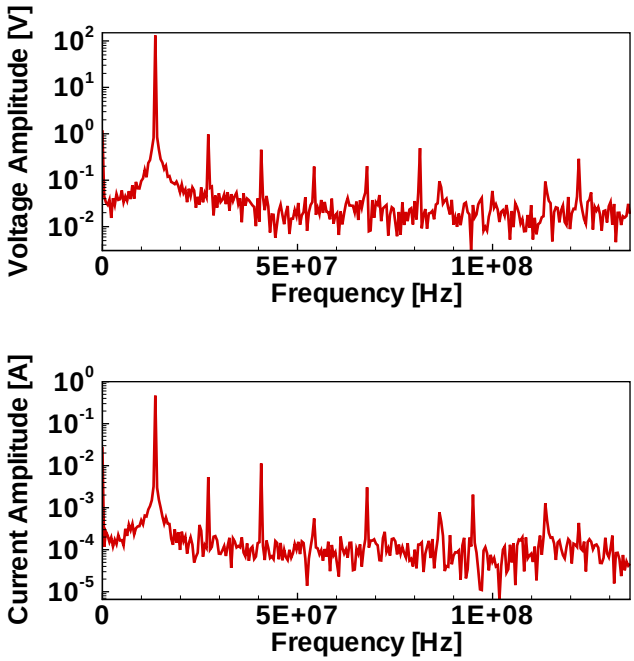

Figure 6.5: Typical voltage and current power spectrum from Fourier decomposition

The plasma reactor is not equipped with automatic systems for controlling the pressure or the matchbox tuning: the matching is kept constant during all the measurements. The pressure adjustment is made by flowing gases at a prescribed composition (only Ar for argon discharge and 4 sccm Ar, 0.5 sccm SiH_4 in He for dusty plasma) into a previously evacuated chamber, closing the downstream valve and then closing the upstream valve when the desired pressure is reached.

Figure 6.4 reports a typical set of collected voltage and current waveforms while Figure 6.5 is the power spectrum of the Fourier transform for that set of waveforms. The Fourier transform of $V_{plasma}(f)$ and $I_{plasma}(f)$ show the presence of higher harmonics up to the sixth. While for power and impedance measurements the only significative contribution is given by the main component at 13.56 MHz, which is 2-3 order of magnitude larger than the others, higher harmonics can contain interesting information about the presence of particles and other plasma characteristics as they arise from

nonlinear effects in the plasma and are not provided by the amplifier or external circuit components: measurements in the empty cell provide in fact a purely sinusoidal signal. During the measurements, as mentioned earlier, the pressure was varied from 200 to 600 mTorr and the power from 20 to 160 W (as displayed on the amplier).

6.4.1 Power measurement

The power provided P differs signicantly from the power P_{abs} absorbed by the plasma (Figure 6.6). On average for the pristine plasma as well as for the dusty plasma the real power coupled to the plasma is about $8-10\%$ of the nominal power provided by the amplifier. The rest is dissipated via heat in the matching network, cables, and electrodes.

6.4.2 Voltage amplitude

Figure 6.7 reports the measurement of the voltage amplitude for the main harmonic for pristine and dusty plasmas. Three conclusions can be drawn from this: (a) the power amplifier is in fact a voltage amplifier and regardless of the current through the plasma a prescribed voltage signal to the power amplifier translates into a given input power at the output of the amplifier and a given voltage amplitude at the powered electrode; (b) voltage does not depend on pressure and it is not affected by the presence of nanoparticles: the two sets of curves do overlap if plotted on the same graph; furthermore (c) electrode voltage scales less-than linearly with input power, as shown from the slope of the line fitting the measured points.

6.4.3 Current amplitude

Figure 6.8 shows the measurement of the current passing through the discharge in terms of the amplitude of the first harmonic. It is worth mentioning that current in the dusty plasma case is 2-5 times smaller than the pristine case at the same voltage-

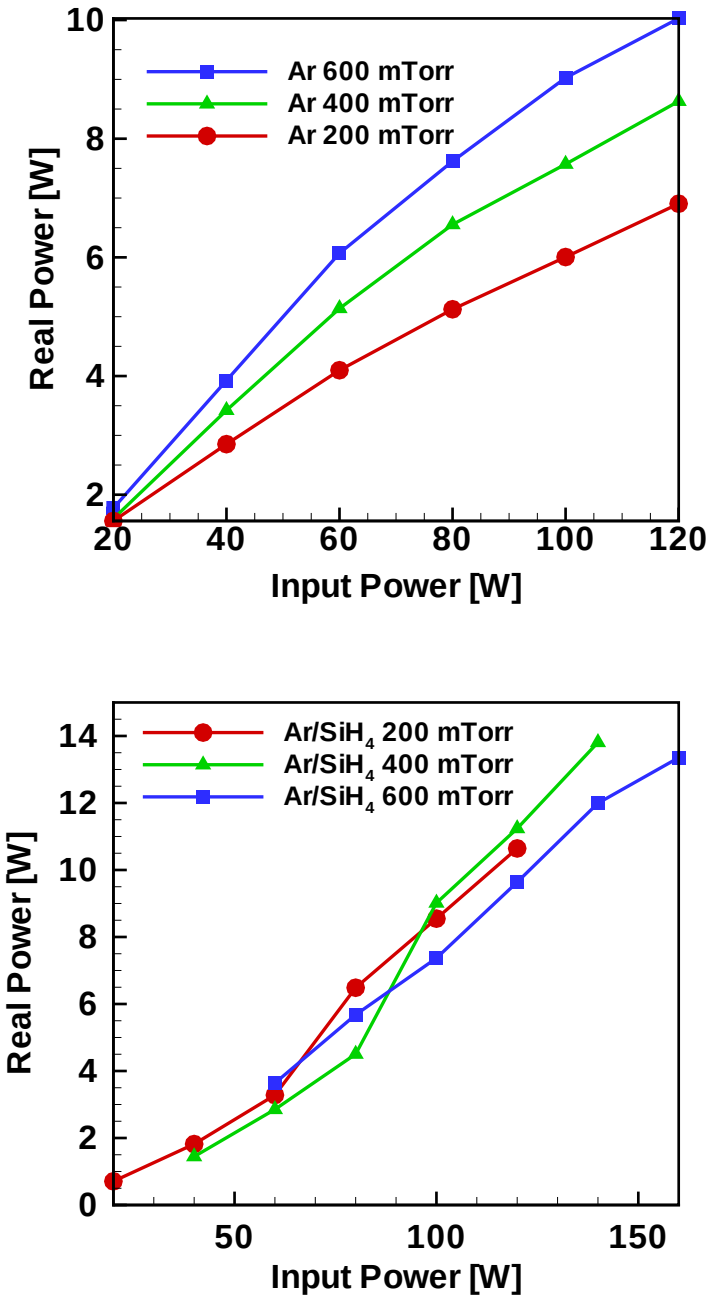

Figure 6.6: Real power coupled to argon (top) and $Ar/SiH_4/He$ (bottom) plasmas, as a function of input power, parametric on pressure

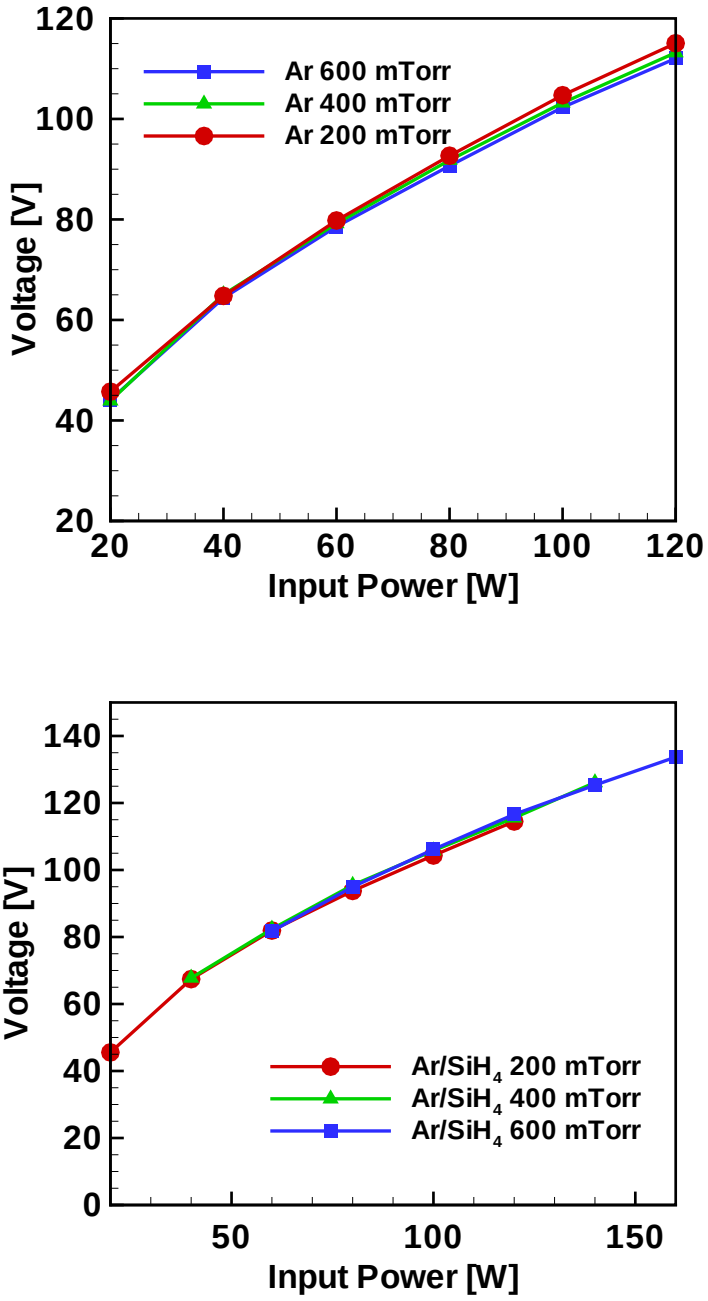

Figure 6.7: Voltage amplitude for argon (top) and $Ar/SiH_4/He$ (bottom) plasmas, as a function of input power, parametric on pressure

input power. Current always increases with coupled power but while in the pristine case current also increases with pressure, in the dusty case we witness a decrease of the current flown for larger pressures. With a larger pressure there is a larger neutral density: larger neutral density increases the electron-neutral collision frequency ($\nu_{e-n} = n_n \sigma_{e-n} < v_e >$, where the LHS (left hand side) contains the neutral density (n_n), the electron-neutral collision cross-section (σ_{e-n}), and the average electron velocity ($< v_e >$)) and contributes to a reduction in the electron current and a more resistive behavior of the plasma. On the other hand a larger neutral density provides potentially a plasma with a larger ion-electron density. This favours larger currents at larger pressures. The prevalence of one effect over the other depends on numerous aspects and most importantly on the pressure range considered. In this case the enhancement of the charged species density probably prevails over the increase in electron-neutral collision frequencies and, for the pristine plasma, current increases with pressure.

For the dusty plasma there is an additional term to be considered: the effect of nanoparticles on the mobility of electrons. A larger neutral pressure for a fixed gas composition provides a larger silane partial pressure and a larger density of nucleated nanoparticles. As it will be shown in Chapter 7, not only do nanoparticles act as a sink for electrons with energy above their floating potential, effectively collecting them and preventing them from conducting current, but also they act as scattering centers for low-energy electrons: the very large elastic scattering cross-section that nanoparticles have for low-energy electrons strongly contributes to reducing the current in dusty plasma as well as giving the plasma a more resistive nature. As a result of these phenomena in the case of silane/argon plasma we see a decrease in current with increasing neutral pressure.

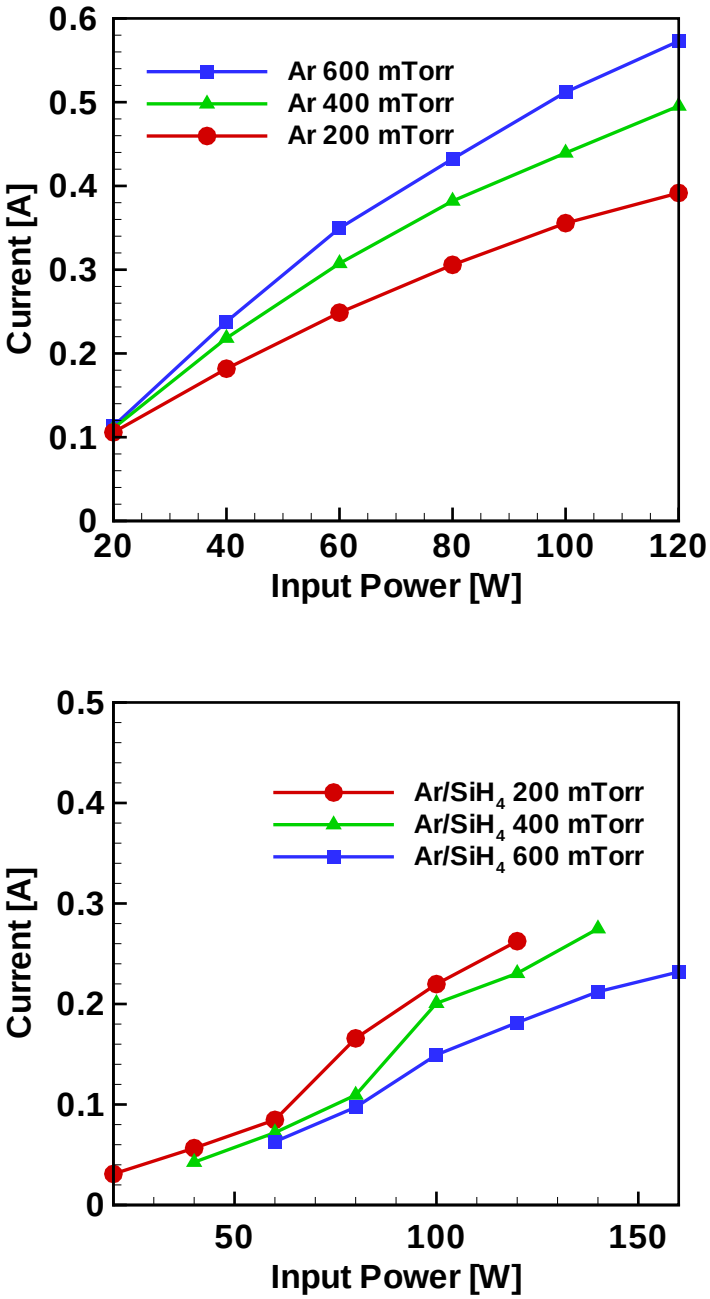

Figure 6.8: Current flowing in argon (top) and $Ar/SiH_4/He$ (bottom) plasmas, as a function of input power, parametric on pressure

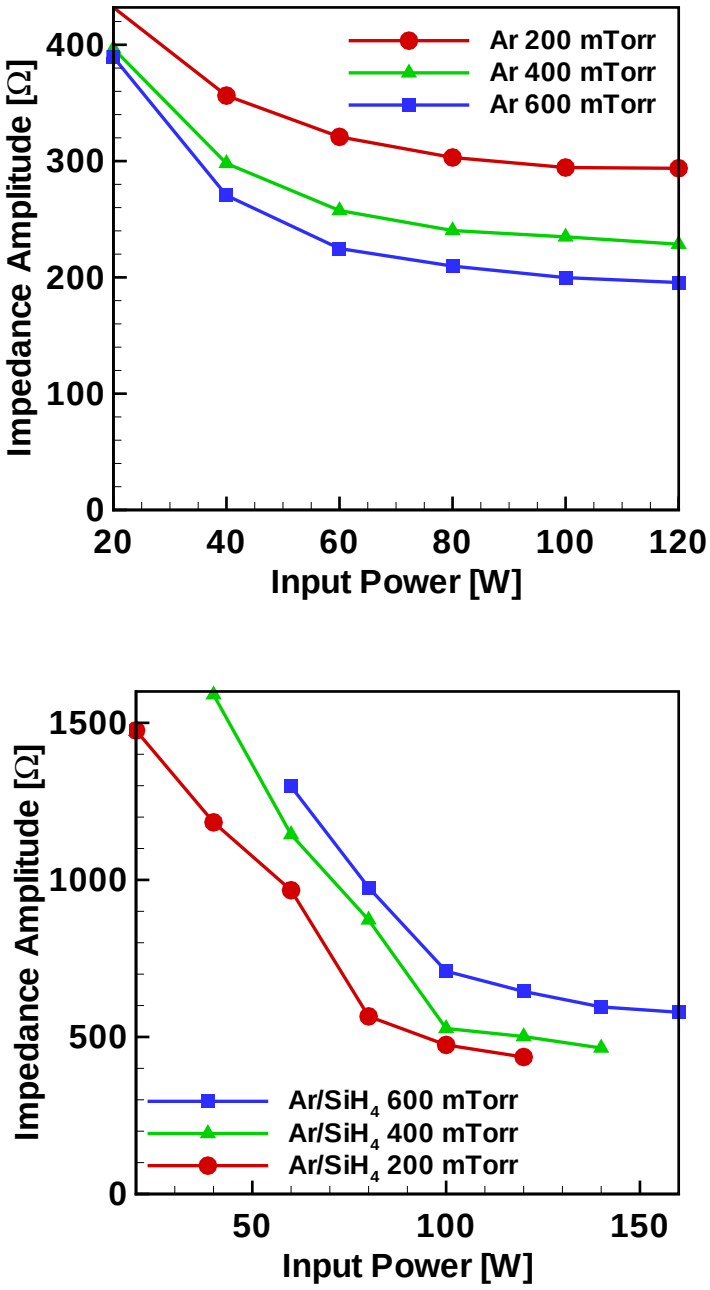

Figure 6.9: Impedance amplitude in argon (top) and $Ar/SiH_4/He$ (bottom) plasmas, as a function of input power, parametric on pressure

6.4.4 Impedance amplitude and phase

Figure 6.9 shows the results for impedance amplitude. While the trends can be explained with the same argument made for the current, it is interesting to notice that the impedance for the dusty plasma case is 2-4 times larger than the pristine case.

As for the phase (Figure 6.10) we notice two things: a more resistive phase (closer to zero) for small powers even in the pristine case, and the strongly more resistive behaviour of dusty plasmas compared to pristine plasmas. Dusty plasmas are also more resistive for larger pressures, a result compatible with the mechanisms described above (electron-neutral and electron-nanoparticle elastic and inelastic collisions).

Finally, Figures 6.11 and 6.12 contain the decomposition of the complex impedance into a resistance (R_{plasma}) and a capacitance (C_{plasma}) according to Godyak *et al.*[106]:

$$R_{plasma} = \frac{V_{plasma}}{I_{plasma}} \cos\phi \tag{6.5}$$

$$C_{plasma} = \frac{V_{plasma}}{I_{plasma}} \frac{1}{\omega \sin\phi} \tag{6.6}$$

where ϕ is simply the phase difference between voltage and current. The capacitance here represents the sheath at the electrodes while the resistance represents the bulk plasma. Although this model is rather simple it can illustrate the physical situations of the discharge quite well.

The capacitance of the plasma increases slightly for higher powers, an effect that can be explained by a transition from a plasma-bulk dominated impedance to a sheath-dominated impedance. The plasma capacitance increases with pressure as well: with decreasing sheath thickness d, as the pressure increases the capacitance of the sheath

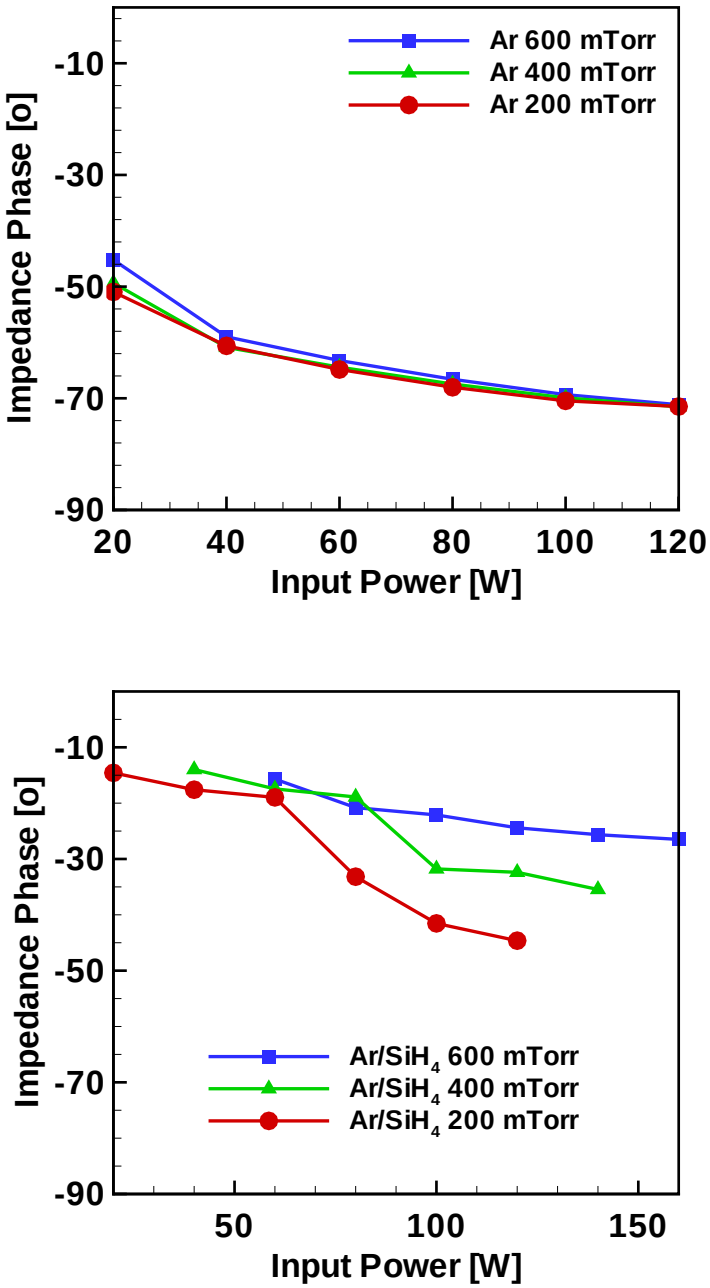

Figure 6.10: Impedance phase in argon (top) and $Ar/SiH_4/He$ (bottom) plasmas, as a function of input power, parametric on pressure

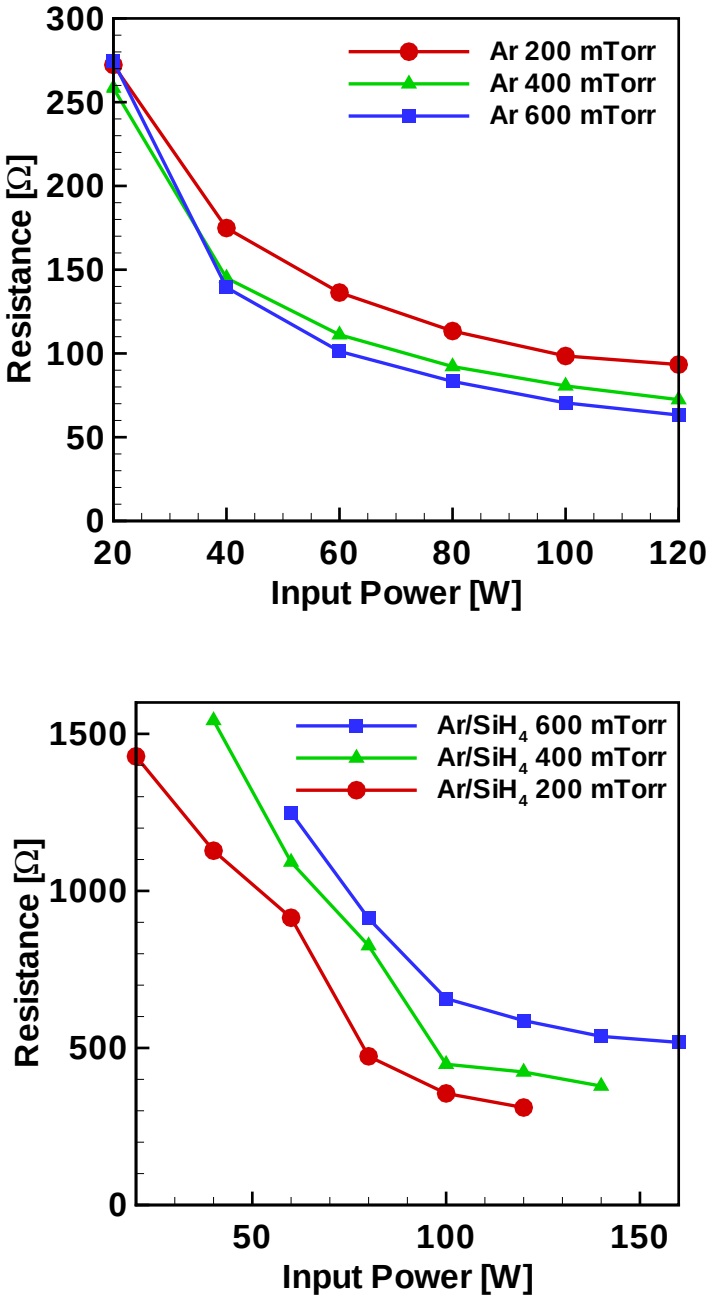

Figure 6.11: Resistance in argon (top) and $Ar/SiH_4/He$ (bottom) plasmas, as a function of input power, parametric on pressure

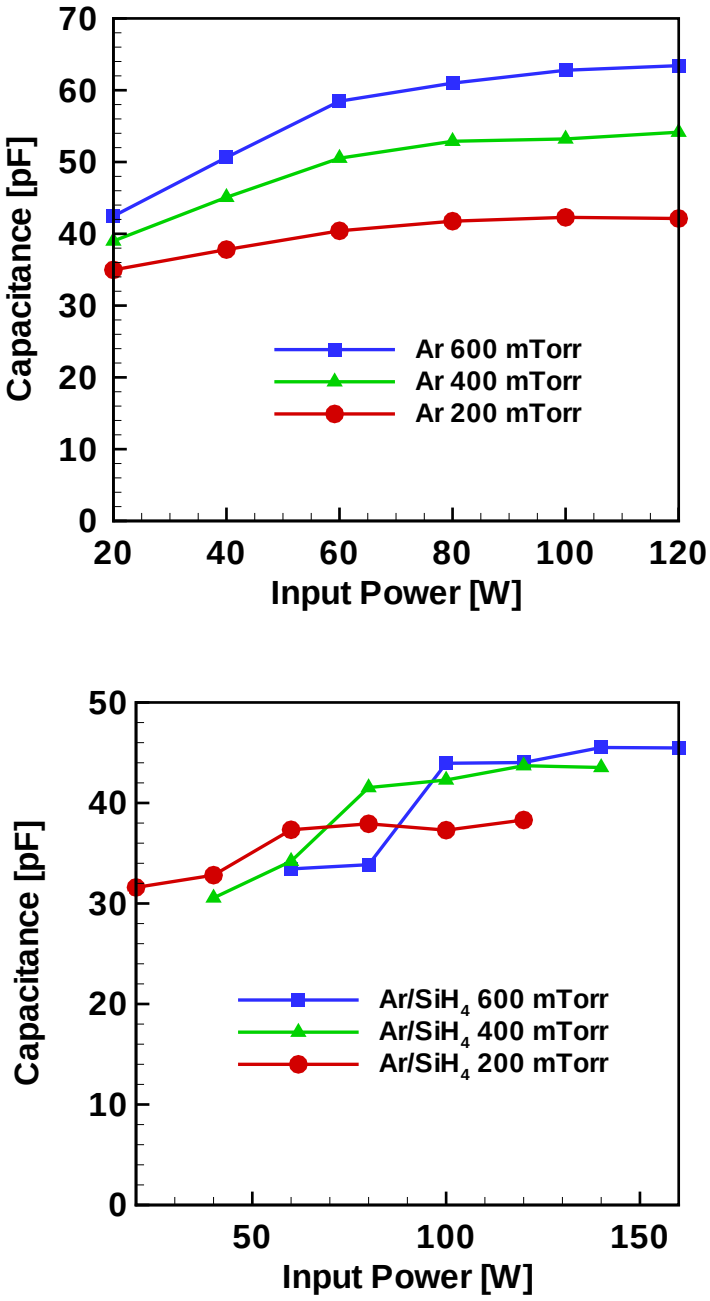

Figure 6.12: Capacitance phase in argon (top) and $Ar/SiH_4/He$ (bottom) plasmas, as a function of input power, parametric on pressure

increases ($C \approx \epsilon_0 \frac{A}{d}$).

The resistance of the plasma also decreases with pressure for pristine plasmas while it increases in the dusty case. This, again, can be easilty explained by the increasing scattering frequency between electrons and nanoparticles ($\nu_{e-nano} = n_{nano}\sigma_{e-n}^{total} < v_e >$, where the LHS contains the nanoparticle density, electron-nanoparticle collision cross-sections, both collection and elastic, and the average electron velocity) due to the decreasing mean free path of the electrons when the nanoparticle density is increased.

6.5 Conclusions

In this chapter, the measurements of electrical properties in capacitively coupled plasmas for pristine and dusty plasmas in a parallel-plate reactor is reported.

In order to extract the electrical properties of the plasma properly an electrical characterization of the discharge chamber was performed. The effects of the stray impedances on the system were related to the components of an equivalent circuit model.

In dust forming discharges a dramatic change in the impedance with respect to the amplitude and phase shift between voltage and current has been observed. The phase shifted into a more resistive region. This indicates a decrease in the electron mobility due to the presence of particles.

This work demonstrates that electrical measurements can be used as an adequate and sensitive tool for the detection of dust particles. It is possible to detect the presence of particles at much smaller size than with other techniques.

Developing a more detailed model together with measurments via Langmuir probe or optical emission spectroscopy would allow to gain more information about plasma quantities, namely the electron density, temperature and anisotropic velocity compo-

nent, allowing for a better and more direct and quantitative understanding of power coupling in radio-frequency low-pressure dusty plasma discharges.

Chapter 7

Self-consistent model for particle charging and evolution of EEDF in a nano-dusty plasma

In a previous chapter a model of nanoparticle charging in low-pressure plasmas was presented. While that model improves previous models for including the effects of ion-neutral charge exchange collisions in proximity of the particle surface there are other assumptions made there that often are not valid. Specifically, an assumption is made about the electron energy distribution in the plasma to be Maxwellian. This simplifying assumption is not realistic in low-pressure plasma.

In this chapter we present a further improvement that develops the current balance to the particle in a form that can fit electron energy distributions different from Maxwellian. Furthermore a solution of the EEDF (electron energy distribution function) is obtained from a self-consistent kinetic model of low-pressure plasmas with nanoparticles based on the expansion in spherical harmonics of the Boltzmann equation and its solution in the two-terms (Lorentz) approximation.

7.1 Introduction

A self-consistent charging model for a 0-D steady-state, low-pressure argon discharge plasmas containing nanoparticles is presented. The model includes a module for evaluating the electron energy distribution function as a result of interactions between ions/electrons and nanoparticles. A set of suitable electron-nanoparticles cross-sections are developed to include elastic (Coulomb) and inelastic (collection) collisions between nanoparticles and electrons.

Moreover, a further improvement of the model includes a particle balance equation and a power balance equation. The solution of the system so formulated is self-consistently matching the creation of new electron-ion pairs to their losses to the surfaces bounding the plasma volume as well as the surfaces of the nanoparticles suspended in the plasma. The electron energy distribution is determined by the solution of the Boltzmann equation, through the use of a Boltzmann solver developed by Kortshagen [107].

The effects of nanoparticles, their size and concentration, and the effect of gas pressure on the electron energy distribution, the "effective" electron temperature, the electron and ion number densities, and the nanoparticle charge are investigated.

The ion flux to the nanoparticles surfaces is accounted for both under the traditional OML approach and the new "collision-enhanced-current" approach that takes into account the effect of charge-exchange collisions in proximity of the surface of the nanoparticles.

Given the complex interactions between electrons, ions, and nanoparticles and their strongly inter-correlated nature it is difficult to draw definitive conclusions on the effect of modyfications to an input parameter on a specific plasma property.

The main result of this chapter is to show that there is a strong effect on the EEDF

as a result of the presence of nanoparticles. Furthermore, while charge and current for nanoparticles are strongly correlated concepts, it is shown here that they play two different roles in the definition of the effects on the EEDFs: the charge carried by a nanoparticle is a "static" variable that affects the energy distribution of electrons only indirectly, by defining a reduction in the free electron density. Quasineutrality, in fact, requires that:

$$n_e = n_i + k\ n_p \tag{7.1}$$

(where k is the charge carried by a nanoparticle in elementary charge units.) The current to a nanoparticle, on the other hand, is a "dynamic" variable: its value affects *the rate* at which electrons are lost through collisions. For situations where the overall flux of charged species to the surface of the particles is enhanced (large particle size and intermediate pressures) a stronger effect of the EEDF is present.

Plasma-grown nanoparticles can dramatically affect the discharge characteristics and the deposition process. For example, existing results show a direct link between the density and charge of the nanoparticles, as well as the electron temperature of the bulk plasma, to the quality of the PECVD fabricated films [108, 109]. For example, in the PECVD of amorphous silicon, device-grade films can only be produced under low nanoparticle density and low electron temperature conditions [110]. In the work of Takai *et al.* electron temperature was measured by an optical-emission spectroscopy method. Results show that electron temperature increases with time after turning on the plasma at a low substrate temperature of $150°C$, while it stays constant at a high substrate temperature of $400°C$. Furthermore electron temperature is drastically reduced when the silane gas is diluted with hydrogen at low substrate temperatures. These results suggest that the electron temperature in silane plasma increases with the presence of nanoparticle, as it is well known that high temperatures and a sufficient concentration of hydrogen are sufficient to delay or avoid the nucleation of

nanoparticles in a silane plasma [44].

The influence of dust particles on discharge properties was investigated in 1991 with the help of particle in cell Monte Carlo simulation by Kushner in 1991 [111] and later with the help of Boltzmann equation for EEDF by Denysenko and Fortov [112, 113]. It was understood that nanoparticles act as an electron and ion sink, and a large concentration of dust particles can have some effects on the plasma properties and on its sustainment conditions. The electron and ion losses on dust particles should be compensated in ionizing collisions, and the average electric field in a discharge should increase in a dusty case compared to a "pristine" plasma case.

7.2 Numerical Model

In this model we assume a low pressure nano-dusty plasma in which the plasma species are electrons, ions, neutrals, and nanoparticles. We assume the nanoparticles to be all of the same size (R_p) and to be uniformly distributed in the reactor volume (V) with a density n_p. Central to this model is again the solution of the nanoparticle floating potential, V_p. This is resulting from the solution of the following non-linear equation:

$$\nu_e(V_p, f_0) = P_{C=0}\nu_i^{OML}(V_p) + P_{C=1}\nu_i^{CE}(R_c(V_p)) + P_{C>1}\nu_i^{HY}(V_p) \tag{7.2}$$

The RHS here is substantially identical to Equation 3.1, with the only difference that we are using here charging rates and not currents. The LHS is different in that it has to accomodate the possibility of the electrons to have a non-Maxwellian energy distribution. f_0 is defined such that $f_0\sqrt{E}dE$ represents the infinitesimal fraction of electrons with an energy between $(E, E + dE)$, and such that $\int_0^\infty f_0\sqrt{E}dE = 1$. The generic expression from electron charging is obtained using the OML approach

without integrating over a specified type of energy distribution [114]:

$$\nu_e(V_p, f_0) = \pi R_p^2 n_e^\infty \int_{-V_p}^{\infty} \left(1 + \frac{V_p}{E}\right) \sqrt{\frac{2eE}{m_e}} f_0(E) \sqrt{E} dE \tag{7.3}$$

Equation 7.2 allows to calculate the charge of a nanoparticle in a plasma with prescribed properties, including an arbitrary electron energy distribution f_0.

The deviation from an ideal Maxwellian behaviour for the electrons are due mainly to two aspects:

- Inelastic collisions between electrons and neutrals that result in excited neutrals and ions. As a result of these effects EEDFs lack high-energy electrons compared to the Maxwellian case.

- Elastic and inelastic collisions between electrons and nanoparticles also affect the EEDF. Elastic collisions in reality have a close to negligible effect on the final distribution. This is due to the fact that, while large cross-section for these processes are possible, their effect is weighted by the ratio of the masses between electron and nanoparticle ($m_e/m_p \approx 0$).

  The inelastic process of electron collection by the nanoparticle, on the other hand, stronlgy affects and in some situations dominates the modifications to the EEDF. Only electrons with an energy above the floating potential of the nanoparticle can be collected. The cross-section for this process is, above the threshold V_p, very large and for large nanoparticle concentrations its collision rate can dominate the RHS of Equation 2.23.

The EEDF are calculated using a Boltzmann equation solver developed by Kortshagen. The Boltzmann equation is solved by expanding the EEDF in spherical harmonics and considering only the first two terms of the expansion (Lorentz approxi-

mation) [115]. This approximation is valid when the isotropic term is larger that the anisotropic one. low to medium pressure plasmas (pL >100 mTorr cm, where p is pressure and L is the plasma size) are certainly good candidates for this approximation [115].

Another approximation made here is to assume a time independent solution. This is valid if the following condition is satisfied [115]:

$$\omega > \nu_e = \frac{2m_e}{m_i}\nu_m + \nu_{ex} + \nu_{ion} \tag{7.4}$$

where ω is the radian excitation frequency of the discharge ($\omega = 2\pi \times 13.56$ MHz), and the terms on the RHS are respectively momentum transfer, excitation, and ionization collision frequencies. This assumption is satisfied "de-facto a-posteriori" by verifiying that Equation 7.4 is valid for all cases investigated.

The background gas investigated here is argon and the argon plasma "chemistry" is included by considering suitable cross-sections for the processes of momentum-transfer (elastic), excitation and ionization (inelastic). The gas cross-sections for this work were taken from the collection made by Phelps [116], and are shown in Figure 7.1.

The cross-sections for electron-nanoparticle interaction were taken from [114], where Khrapak and Morfill investigated the role of the electron drag force in a dusty plasma at fixed electric field.

Elastic collisions between electrons and nanoparticles do not result in the collection of the electron by the particle but in a deviation of its motion from scattering with the massive electrically-charged nanoparticle. The derivation of the cross-section is based on the assumption of a Coulomb-like unshielded potential profile, truncated at a distance λ_{DL} from the surface of the nanoparticle. The resulting cross-section

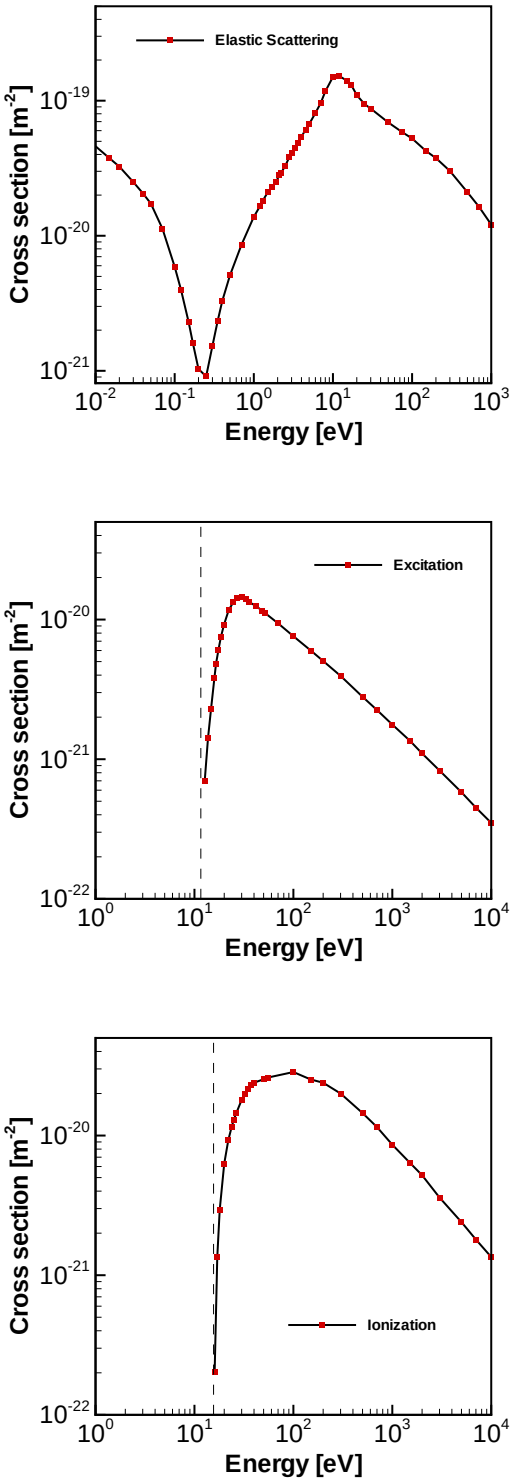

Figure 7.1: Cross-sections for argon for the processes of elastic scattering (momentum transfer), excitation, and ionization. The dashed line is a guide to the eye for the threshold energy levels.

is expressible in a closed format and behaves substantially the same as the non-analytically expressible cross-section derived from a Yukawa potential [114]:

$$\sigma_{elastic}(V_p, E) = 2\pi R_p^2 \left(\frac{V_p}{E}\right)^2 \log\left(\frac{\lambda_{DL}^2 + \left(\frac{V_p}{2E}\right)^2 R_p^2}{\left(1 + \frac{V_p}{E}\right) R_p^2 + \left(\frac{V_p}{2E}\right)^2 R_p^2}\right) \tag{7.5}$$

The inelastic cross-section (collection) is, more simply:

$$\begin{cases} \sigma_{inelastic} = & \pi R_p^2 \left(1 + \frac{V_p}{E}\right) & E > -V_p \\ \sigma_{inelastic} = & 0 & E \leq -V_p \end{cases} \tag{7.6}$$

These cross-sections are a function of both electron energy and nanoparticle floating potential.

The code used to obtain the results that follow, in its simplest form, takes for input the particle size (radius, R_p), the ion density, the ion temperature, the neutral pressure, the nanoparticle density, and the reduced electric field (E/n). Initially an iteration of the Boltzmann solver is performed assuming a "pristine" plasma. This produces a first approximation of the EEDF is the absence of nanoparticles. At this point, a system of 2 equations, Equation 7.2 and 7.1, is solved a first time to estimate the charge on the nanoparticles and the deficit of electron density compared to ion density. Successively, Equations 7.5 and 7.6 are used to generate the cross-sections for electron-nanoparticle interactions. These are added to the cross-section database of the Boltzmann solver, to allow for a second iteration on the solution of the Boltzmann equation that now includes the effect of nanoparticles. A new EEDF is generated, through Equations 7.2 and 7.1, a new estimate of V_p and n_e, new cross-sections and so forth, until the process converges to a solution comprising the EEDF, V_p, and n_e. The iterative process is stopped when the absolute integral difference of the EEDFs from two successive iterations is below a prescribed accuracy.

The same process can be accomplished while including or excluding the effect of charge-exchange collisions between ions and neutrals. A comparison between the two that gives some more insight into the effects on the electron dynamics is given in a later section of the chapter.

7.3 Numerical Results

7.3.1 Effect of nanoparticles on EEDF in argon low-pressure plasmas

In the first part of this section we will look at individual aspects of nanoparticle-plasma interactions and we will derive some direct correlations between the behavior of the EEDF and simple input parameters such as nanoparticle size, concentration, and neutral pressure.

In the second part of this section the model will be extended to include a particle balance and a power balance. That approximation will give a more realistic description of the plasma discharge at the expense of a loss of direct correlation between cause and effect in the results presented.

7.3.2 Effect of nanoparticles concentration

The first effect that is worth investigating regarding the presence of nanoparticles in a plasma is to study how their presence and their concentration affects the properties of the electron energy distribution function. As nanoparticles interact with electrons through elastic and inelastic collisions it is expected to have a stronger and stronger effect on the EEDF as the nanoparticle concentration is increased.

Figure 7.2 reports the results of a study for increasing concentrations of nanoparticles of 500 nm in radius particles for densities ranging from $n_p = 1 \times 10^{10}\mathrm{m}^{-3}$ to $6 \times 10^{13}\mathrm{m}^{-3}$) for a 10 Pa argon plasma with E/n=50 Td and an ion density of $n_i =$

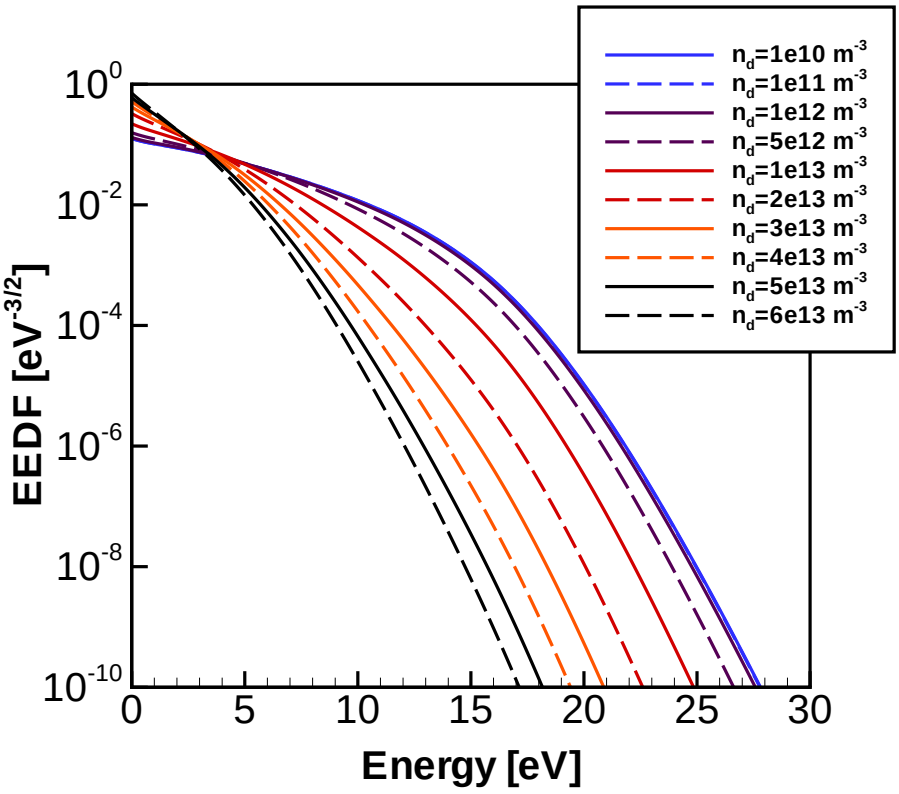

Figure 7.2: EEDF for dusty plasma: R_p=500 nm, $n_p = 1 \times 10^{10}\text{m}^{-3}$ to $6 \times 10^{13}\text{m}^{-3}$, p=10 Pa, E/n=50 Td, $n_i = 1 \times 10^{18}\text{m}^{-3}$

$1 \times 10^{18}\text{m}^{-3}$.

As expected, larger concentrations on nanoparticles cause a reduction in the density of electron in the high-energy tail of the distribution. In the low-nanoparticle-density case it is evident how the EEDF presents the typical "knees" in energy-space in proximity of the thresholds for excitation and ionization processes. By increasing the concentration of nanoparticles the importance of these processes is relatively reduced and a new "knee" above the value of the floating potential ($\approx$ 4 V) for the particle appears. Collection of electrons by nanoparticle becomes the prevalent mechanism of electron-loss in high nanoparticle density dusty plasmas.

7.3.3 Effect of neutral pressure on the EEDF of nanoparticles

Pressure plays an important role in dusty plasmas, more so than in pristine plasmas. It is well known in fact that EEDFs are not affected by different pressures if the reduced electric field is kept constant: by increasing the pressure the density of neutrals is increased resulting in an increased probability of ionizing collisions that sustain the discharge as well as collision that deplete the energetic electrons, (ionization, excitation and momentum transfer). If pressure increases in the same way as the electric field does, the same results are obtained, with the exception of higher order effects.

The presence of nanoparticles breaks this symmetry: they decrease the energy content of the electron population by removing electrons above V_p. Furthermore, even if the nanoparticle density is orders of magnitudes lower than the density of neutral and charged species (ions and electrons), the massive cross-section of nanoparticles results in a strong effect on the EEDFs as pressure is modified.

Results of a parametric investigation of pressure for "pristine" and dusty plasmas are presented in Figure 7.3.

The small effect of pressure on EEDFs for the pristine case is due to the effect of neutral density changes at a constant electron density. Electron-electron collisions play a more important role at low-pressures, where electron-neutral collisions are relatively less frequent. At low-pressures the relatively larger electron density results in a stronger effect of electron-electron collisions in reshaping the EEDFs towards a more Maxwellian distribution, raising slightly the high-energy electron tail.

For dusty plasma the effect of reducing pressure is similar to the effect obtained by increasing the nanoparticle concentration. At low-pressures electron-nanoparticle collisions play relatively a more important role than electron-neutral collisions. As a result the EEDF sees a reduction of the high-energy tail and once again the onset of

a “knee” in proximity of the nanoparticle floating potential.

Figure 7.4 gives the variation of particle floating potential, normalized free electron density, and “effective” electron temperature. Again, the only significative effect of changing the discharge pressure is to affect the discharge electron temperature.

7.3.4 Effect of particle size on the EEDF

To investigate the effect of particle size on EEDFs it is important to realize that larger particles collect more charge. As a result it would be of little interest to run simulations by only changing the particle size, because larger particle would deplete more the electron density than smaller particles at the same density.

Under OML theory, electron temperature and nanoparticle floating potential are proportional:

$$T_e \alpha V_p = \frac{Z}{4\pi\epsilon_0 R_p} \tag{7.7}$$

Furthermore, for quasi-neutrality:

$$n_e = n_i + k\ n_p \tag{7.8}$$

As a result, if nanoparticle did not affect the EEDFs, mantaining a constant $R_p \times n_d$ product would lead to a constant free normalized electron density, while allowing to investigate different nanoparticle sizes. In an attempt to isolate as much as possible the effect of nanoparticle size on the EEDF from other spurious effects, this approach is used.

In this simulation $R_p \times n_d = 1 \times 10^{17}\text{nm/m}^3$, E/n=25 Td and 50 Td and the ion density is $n_i = 1 \times 10^{18}\text{m}^{-3}$, while the background pressure is fixed at 10 Pa and the nanoparticle radius in varied between 1 and 100 nm.

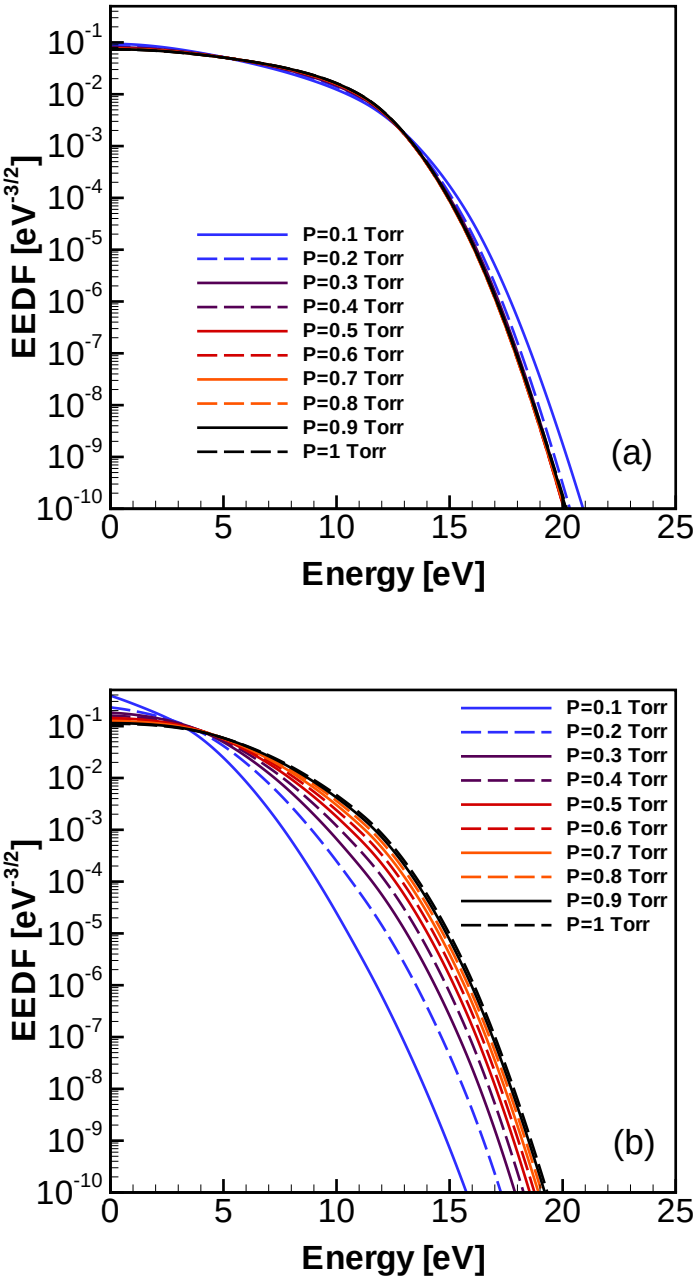

Figure 7.3: Effect of pressure on EEDFs without (a) and with (b) nanoparticles. Plasma properties: E/n= 25 Td, $n_i = 1 \times 10^{17}\mathrm{m}^{-3}$, p=0.1 - 1 Torr. For the nanoparticles (b) $R_p = 1\mu\mathrm{m}$ and $n_d = 5 \times 10^{12}\mathrm{m}^{-3}$

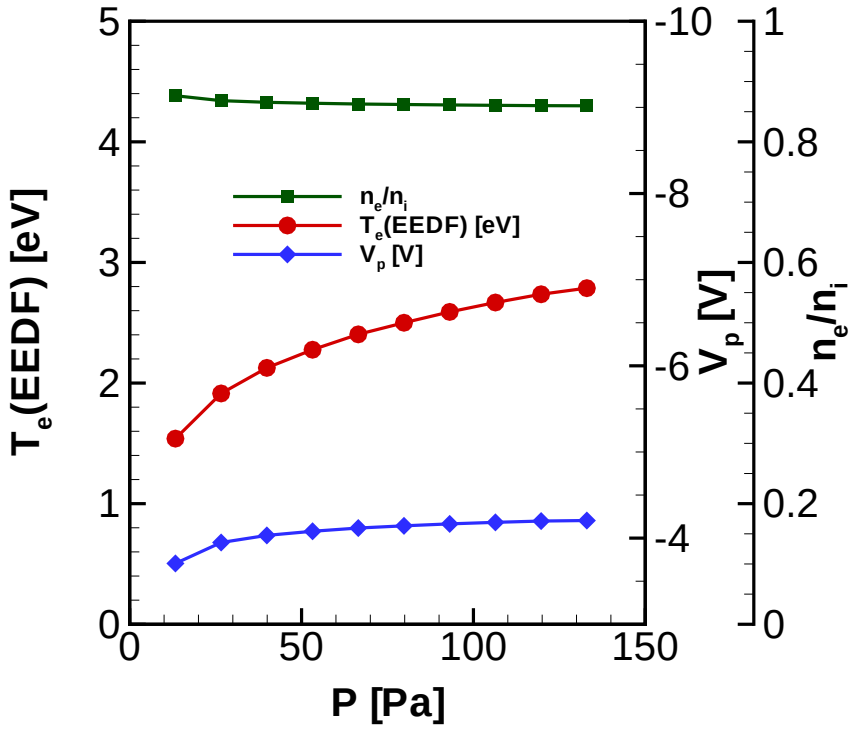

Figure 7.4: Effect of pressure on V_p, n_e/n_i, and T_e. Plasma properties: E/n= 25 Td, $n_i = 1 \times 10^{17}\text{m}^{-3}$, p=0.1 - 1 Torr. For the nanoparticles (b) $R_p = 1\mu$m and $n_d = 5 \times 10^{12}\text{m}^{-3}$.

The results of this parametric study are presented in Figures 7.5 and 7.6. The main insight that we get from this study is the fact that while particle size and particle charge scale semi-linearly, the effect on the EEDF is somewhat linear with particle cross-section (R_p^2) resulting in a stronger influence on EEDF for larger particles and a reduced total fraction of negative charge carried by the particles! This is consistent with the idea that nanoparticle charge represents a "static" variable, that affects the fraction of free electrons available in the discharge, while the electron charging rate, relatively larger for larger particle, is a more direct cause for changes in the EEDF.

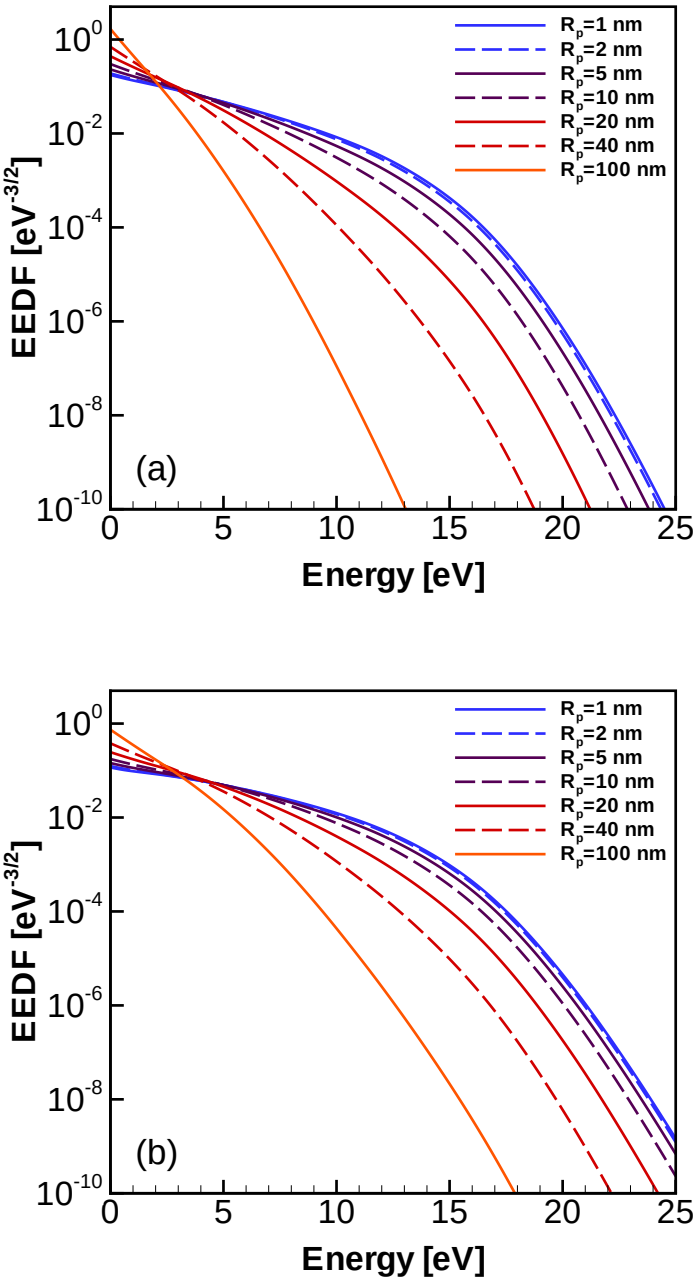

Figure 7.5: Effect of particle size on EEDFs for (a):E/n=25 Td and (b):E/n=50 Td, fixed $n_i = 1 \times 10^{18}\mathrm{m}^{-3}$,$n_e$ based on quasi-neutrality; the plots are parametric with respect to radius for a constant $R_p \times n_d = 1 \times 10^{17}\mathrm{nm/m}^3$. Pressure is 10 Pa.

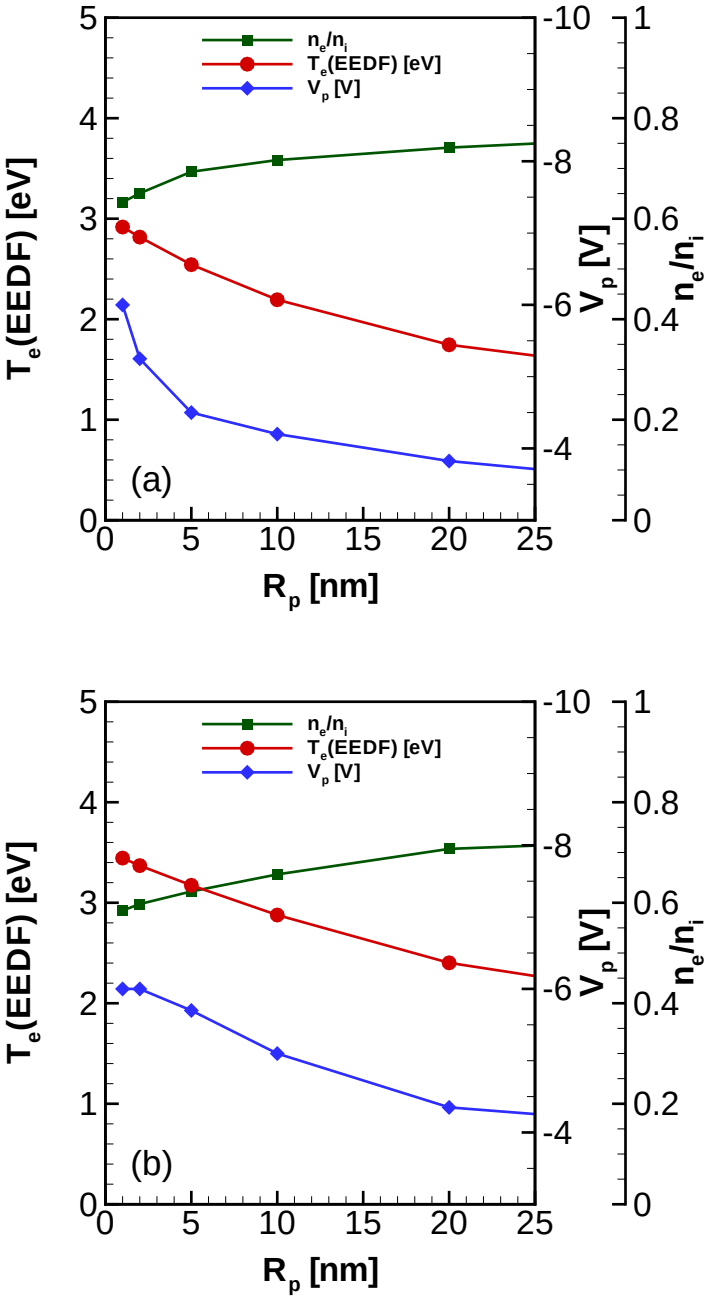

Figure 7.6: Effect of particle size on T_{EEDF}, V_p and n_e/n_i for (a): E/n=25 Td and (b):E/n=50 Td, fixed $n_i = 1 \times 10^{18}\mathrm{m}^{-3}$,$n_e$ based on quasi-neutrality; the plots are parametric with respect to radius for a constant $R_p \times n_p = 1 \times 10^{17}\mathrm{nm/m}^3$, p=10 Pa

7.3.5 Self-consistent effect of nanoparticle density

In the previous sections the effect of nanoparticle size and density and the effect of pressure on the shape of the EEDF for a given value of reduced electric field were investigated. That was done in order to provide some direct correlation between cause and effect. To have a better description of the behaviour of the nanoparticle-plasma system, however, it is necessary to remember that a plasma is "sustained" only when the number of ionizing collisions matches the ion losses. The previous examples did not contain that provision. Furthermore, ion density is not a "natural" input parameter. In laboratory the more direct parameter, that indirectly determines the ion density, is the power coupled to the discharge.

In this section we introduce and add to the model a particle balance that matches ions production to ion losses, and a power balance that allows us to define plasma conditions in a way as close as possible to the one adopted by "experimentalists".

The particle balance equation is:

$$n_i \frac{D_a}{l} A + n_i \nu_{ip} V = n_e \nu_i(EEDF) V \tag{7.9}$$

where all terms where defined before in Chapter 3. The geometry of the reactor investigated is the same that was used before. ν_i is not anymore an approximation based on an assumed Maxwellian distribution, but results from the direct integration of ionization cross-section over the electron energy distribution:

$$\nu_i = n \ \langle \sigma_i(v) v \rangle_{v(EEDF)} \tag{7.10}$$

The power balance is:

$$P_{RF} = n_e(\nu_i E_i + \nu_{ex} E_{ex})V + n_i \frac{D_a}{l} Ae \frac{V_{sh}}{2} + en_e V \frac{2m_e}{m_i} \int_0^\infty \nu_m f_0 E^{3/2} dE + n_p V \int_{-V_p}^\infty E dI_e(E) \tag{7.11}$$

here ν_{ex} is the total excitation frequency for argon, E_i and E_{ex} are the energies associated with the ionization and excitation collisions, V_{sh} is the sheath voltage at the electrodes, (assumed to be 300 V here), and $dI_e(E)$ is the infinitesimal electron current to a nanoparticle comprising only electrons with energy in the range $(E, E + dE)$. Functionally, on the RHS, the first term represent energy loss to ionization and excitation events in the volume of the discharge. The second term represents energy loss through diffusion to the electrodes. The third term represents energy loss through electron-neutral momentum transfer, macroscopically resulting in a gas temperature slightly larger than room temperature.

The last term represents energy loss to the nanoparticles through the collection of electrons. For this contribution, there is an important aspect to keep in mind: an electron with energy $E > -V_p$ loses directly to the nanoparticle an energy equal to $E + V_p$. The residual energy, V_p, is also lost, but from the successive collection of an ion.

The following results include the particle and power balance and provide some insight into the behaviour of a well-defined nano-dusty discharge.

Figures 7.7 and 7.8 contain the results of a calculation for a dusty plasma with 500 nm in diameter particle, as a function of nanoparticle concentration. In that case the power coupled to the plasma was held fixed at 500 W and the pressure was 50 Pa. These are the only parameters that are needed to run the simulation, but are also the parameters that one would control in performing a laboratory experiment. In Figure 7.7 the charge-exchange ion-neutral collision mechanism is present, while in Figure

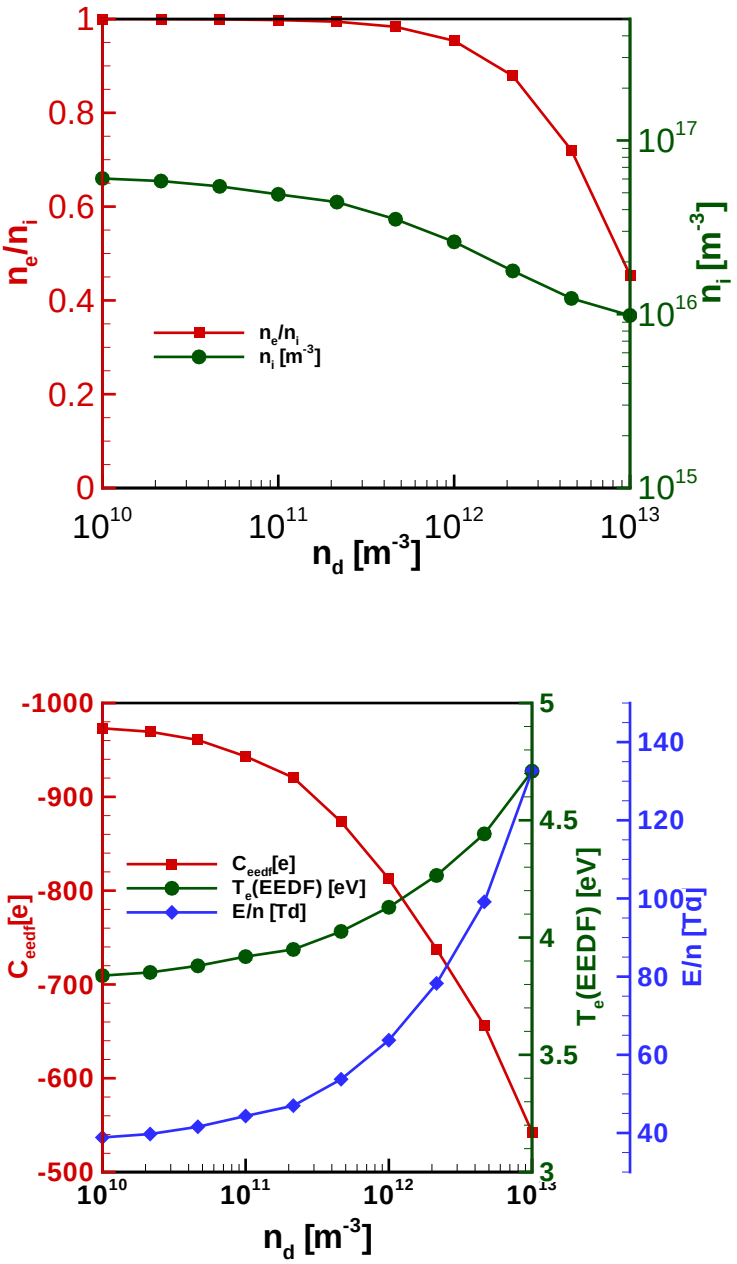

Figure 7.7: Evolution of normalized electron density, ion density, particle charge, "effective" electron temperature, and reduced electric field for a dusty plasma with 500 nm particles, at a pressure of 50 Pa and a power of 500 W, as a function of nanoparticle density, *including* the effect of charge-exchange ion-neutral collisions.

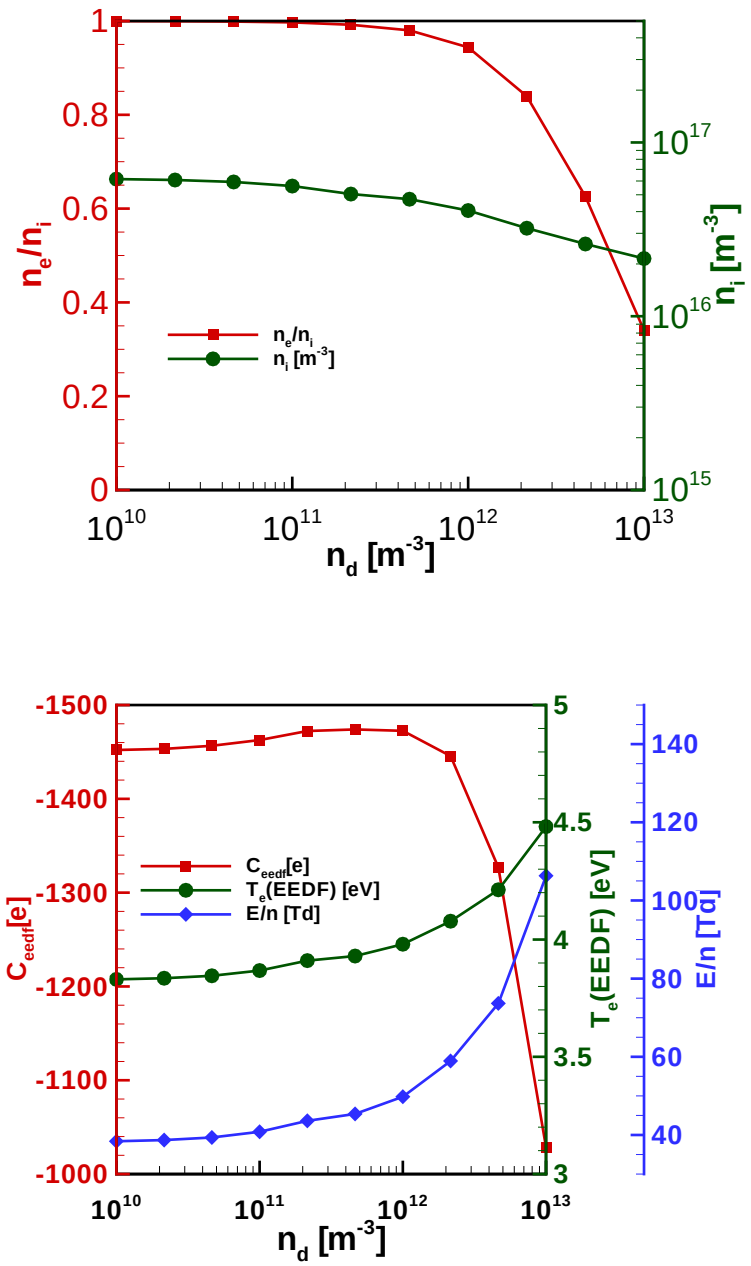

Figure 7.8: Evolution of normalized electron density, ion density, particle charge, "effective" electron temperature, and reduced electric field for a dusty plasma with 500 nm particles, at a pressure of 50 Pa and a power of 500 W, as a function of nanoparticle density, *excluding* the effect of charge-exchange ion-neutral collisions.

7.8, that mechanism is turned off.

Starting our analysis from the OML case (Figure 7.8) we can see that, in a more realistic case, as the nanoparticle concentration is increased, the discharge needs to increase the electric field (and as a consequence the electron temperature) to compensate the increasing ion losses to the surface of the particle. Because of the increase in the electron temperature, there is a range of particle densities that sees an increase of the average particle charge carried by the particles. In this region the fraction of electrons carried by particles is still negligible compared to the free electron density, while there is a slight reduction in the ion density resulting from the need to sustain the discharge at a fixed power and at higher electric fields.

At larger particle concentrations the fraction of electrons carried by the nanoparticles becomes relevant. The reduction of free electron density compared to ion density, result in a reduction of the average particle charge, while the ion density continues to decrease.

In Figure 7.7 show the results for the same case, with the additional effect of charge-exchange ion-neutral collisions in the ion current to the nanoparticle. There are a few additional effects present in the results that are unambigously due to this. First and foremost the average charge carried by the particle is much reduced, even at low nanoparticle concentrations. As the nanoparticle concentration is increased once again the discharge as to adjust the electric field to compensate for the additional ion losses to the surface of the nanoparticles. However this increase in the electric field and in the electron temperature does not cause an initial increase in the charge carried by the particle as in the OML case: even if the electron density carried by particles is still negligible compared to the free electron density, we witness a reduction in the charge.

To understand this we have to look at the behaviour of the ion density. As larger

concentration of nanoparticles are loaded in the reactor, the ion density needs to be reduced, for a fixed input power. This reduction in the ion density results in the increase of the linearized Debye length. This results in a larger "capture" radius, a larger flux of ions and electrons to the surface of the particle and it is ultimately the cause for the reduction in the particle charge. Furthermore the enhancement of the currents to the particles causes a stronger increase in the electric field and electron temperature and the increased ion losses call for a smaller ion density available at larger values of nanoparticle density, compared to the OML case.

7.4 Conclusions

A model for argon dusty plasma has been presented in this chapter. The model allows to calculate the electron EDF, the electron "effective" temperature, ion and electron densities, and the nanoparticle charge as a function of discharge pressure and power input.

Changes in particle size, particle density and neutral pressure were investigated and the effects that these have on the resulting EEDFs were reported and discussed.

The behaviour of a realistic approximation of the plasma-nanoparticle system was investigated with and without the effects due to charge-exchange ion-neutral collisions. These collisions are shown to play an important role, not only for the charge of the nanoparticles, but also in determining the other plasma parameters because of their ability to enhance the interactions and more specifically ion losses to the surface of the nanoparticles.

Chapter 8

Conclusion

8.1 Conclusions

In summary, the role of ion-neutral collisions in enhancing the ion current to nanoparticles and lowering the absolute value of their floating potential in a dusty plasma was investigated. An analytical model that includes the effects of such collisions was developed and the effect this has on the particle charge and temperature was developed. Results show charge distribution much less negative than the OML prediction and particle temperatures that reach levels able to favour crystallization of silicon semiconductor nanoparticles.

Experiments show the control over the nanoparticle morphology as a function of the power coupled to the discharge. The ability to produce silicon nanoparticle films with a prescribed amorphous-crystalline content is proven.

The measurement of the power and impedance of the plasma and the effects of nanoparticles on this was carried out. Nanoparticles are shown to strongly affect the electrical nature of the discharge, providing a considerably more resistive nature to it.

The energy distribution of ions impinging on the surface of nanoparticles was also in-

vestigated, via a molecular dynamic approach. Charge-exchange ion-neutral collisions are shown to play a major role also on this type of interactions between plasma and nanoparticles, as the resulting IEDFs show a considerable reduction of the energy of impinging ions for pressure that are typical in the plasma-synthesis of nanoparticles. Some considerations on the consequences this can have on the quality of the material produced and the effects on the plasma-nanoparticle surface chemistry are presented.

Finally, a self-consistent model for the derivation of the EEDFs in dusty plasma is presented. Results show that in a fully self-consistent simulation, plasma adjusts to the presence of nanoparticles by increasing the electric field, in order to enhance ionization and compensate for additional losses of ions due to the presence of nanoparticle.

Bibliography

[1] http://en.wikipedia.org/wiki/Plasma_(physics).

[2] Uwe Kortshagen, Rebecca Anthony, Ryan Gresback, Zachary Holman, Rebekah Ligman, Chin-Yi Liu, Lorenzo Mangolini, and Stephen A. Campbell. Plasma synthesis of group iv quantum dots for luminescence and photovoltaic applications. *Pure Appl. Chem.*, 80:1901–1908, 2008.

[3] X D Pi, R W Liptak, J Deneen Nowak, N P Wells, C B Carter, S A Campbell, and U Kortshagen. Air-stable full-visible-spectrum emission from silicon nanocrystals synthesized by an all-gas-phase plasma approach. *Nanotechnology*, 19(24):245603, 2008.

[4] U. Kortshagen and U. Bhandarkar. Modeling of particulate coagulation in low pressure plasmas. *Phys. Rev. E*, 60(1):887–898, Jul 1999.

[5] H. Thomas, G.E. Morfill, V. Demmel, J. Goree, B. Feuerbacher, and D. Mohlmann. Plasma crystal: Coulomb crystallization in a dusty plasma. *Phys. Rev. Lett.*, 73(5):652–655, 1994.

[6] Mihly Hornyi. Charged dust dynamics in the solar system. *Annual Review of Astronomy and Astrophysics*, 34(1):383–418, 1996.

[7] L. Boufendi, A. Plain, J.P. Bloundeau, A. Bouchoule, C. Laure, and M. Toogood. Measurements of particle size kinetics from nanometer to micrometer scale in a low-pressure argon-silane radio-frequency discharge. *Appl. Phys. Lett.*, 60:169–171, 1992.

[8] A. Bouchoule and L. Boufendi. Particulate formation and dusty plasma behavior in argon-silane rf discharge. *Plasma Sources Sci. Technol.*, 2:204–13, 1993.

[9] A. Bouchoule, A. Plain, L. Boufendi, J.P. Bloundeau, and C. Laure. Particle generation and behavior in a silane-argon low-pressure discharge under continuous or pulsed radio-frequency excitation. *J. Appl. Phys.*, 70:1991–2000, 1991.

[10] P. Belenguer, J.P. Blondeau, L. Boufendi, M. Toogood, A. Plain, A. Bouchoule, C. Laure, and J.P. Boeuf. Numerical and experimental diagnostics of rf discharges in pure and dusty argon. *Phys. Rev. A*, 46:7923–7933, 1992.

[11] Uwe Kortshagen. Nonthermal plasma synthesis of semiconductor nanocrystals. *Journal of Physics D: Applied Physics*, 42:113001, 2009.

[12] L. Mangolini, E. Thimsen, and U. Kortshagen. High-yield plasma synthesis of luminescent silicon nanocrystals. *Nano Letters*, 5(4):655–659, 2005.

[13] Ameya Bapat, Curtis Anderson, Christopher R Perrey, C Barry Carter, Stephen A Campbell, and Uwe Kortshagen. Plasma synthesis of single-crystal silicon nanoparticles for novel electronic device applications. *Plasma Physics and Controlled Fusion*, 46(12B):B97–B109, 2004.

[14] Lorenzo Mangolini and Uwe Kortshagen. Selective nanoparticle heating: another form of nonequilibrium in dusty plasmas. *Phys. Rev E*, 79:026405, 2009.

[15] F. Galli and U.R. Kortshagen. Charging, coagulation, and heating model of nanoparticles in a low-pressure plasma accounting for ion and neutral collisions. *Plasma Science, IEEE Transactions on*, 38(4):803 –809, 2010.

[16] M.A. Reed, R.T. Bate, K. Bradshaw, W.M. Duncan, W.R. Frensley, J.W. Lee, and H.D. Shih. Spatial quantization in GaAs-AlGaAs multiple quantum dots. *J. Vac. Sci. Technol. B*, 4:358–60, 1986.

[17] S. Schmitt-Rink, D.A.B. Miller, and D.S. Chemla. Theory of the linear and nonlinear optical properties of semiconductor microcrystallites. *Physical Review B*, 35:8113–25, 1987.

[18] C.B. Murray, D.J. Norris, and M.G. Bawendi. Synthesis and characterization of nearly monodisperse CdE (E=S, Se, Te) semiconductor nanocrystallites. *J. Am. Chem. Soc.*, 115:8706–8715, 1993.

[19] U V Bhandarkar, M T Swihart, S L Girshick, and U R Kortshagen. Modelling of silicon hydride clustering in a low-pressure silane plasma. *Journal of Physics D: Applied Physics*, 33(21):2731, 2000.

[20] P. Roca i Cabarrocas, A Fontcuberta i Morral, S Lebib, and Y. Poissant. Plasma production of nanocrystalline silicon particles and polymorphous silicon thin films for large-area electronic devices. *Pure and Applied Chemistry*, 74:359–367, 2002.

[21] Curtis M. Anderson. *Enhanced Crystallization of Amorphous Silicon Thin Films Using Embedded Silicon Nanocrystals*. PhD thesis, University of Minnesota, 2008.

[22] K. Nishiguchi and S. Oda. Electron transport in a single silicon quantum structure using a vertical silicon probe. *J. Appl. Phys.*, 88:418690, 2000.

[23] Y. Fu, M. Willander, A. Dutta, and S. Oda. Carrier conduction in a si-nanocrystal-based single-electron transistor: I. effect of gate bias. *Superlatt. Microstruct.*, 28:17787, 2000.

[24] S Banerjee, S Huang, T Yamanaka, and S Oda. Evidence of storing and erasing of electrons in a nanocrystalline-si based memory device at 77 K. *J. Vac. Sci. Technol. B*, 20:11358, 2002.

[25] Yongping Ding, Ying Dong, A. Bapat, J.D. Nowak, C.B. Carter, U.R. Kortshagen, and S.A. Campbell. Single nanoparticle semiconductor devices. *Electron Devices, IEEE Transactions on*, 53(10):2525–2531, Oct. 2006.

[26] G. J. Snyder and E. S. Toberer. Complex thermoelectric materials. *Nature Mater.*, 7:10514, 2008.

[27] A. Gallagher. Model of particle growth in silane discharges. *Phys. Rev. E*, 62:2690–706, 2000.

[28] L. Ravi and S. L. Girshick. Coagulation of nanoparticles in a plasma. *Physical Review E*, 79:026408, 2009.

[29] L. Ravi and S. L. Girshick. Modeling the spatiotemporal evolution of a nanodusty plasma. *IEEE Transactions on Plasma Science*, 36:1022–1023, 2008.

[30] S. L. Girshick and S. J. Warthesen. Nanoparticles and plasmas. *Pure and Applied Chemistry*.

[31] S. J. Warthesen, U. Kortshagen, and S. L. Girshick. Numerical simulation of nanoparticle transport during plasma-enhanced chemical vapor deposition. *IEEE Transactions on Plasma Science*, 33:398–399, 2005.

[32] Ira B. Bernstein and Irving N. Rabinowitz. Theory of electrostatic probes in a low-density plasma. *Physics of Fluids*, 2:112–121, 1959.

[33] J. E. Allen, B. M. Annaratone, and U. de Angelis. On the orbital motion limited theory for a small body at floating potential in a maxwellian plasma. *Journal of Plasma Physics*, 63:299–309, 2000.

[34] J. Goree. Ion trapping by a charged dust grain in a plasma. *Phys. Rev. Lett.*, 69(2):277–280, Jul 1992.

[35] V.A. Schweigert and I.V. Schweigert. Coagulation in low-temperature plasmas. *J. Phys. D: Appl. Phys.*, 29:655, 1996.

[36] A. V. Zobnin, A. P. Nefedov, V. A. Sinelshchikov, and V. E. Fortov. On the charge of dust particles in a low-pressure gas discharge plasma. *Journal of Experimental and Theoretical Physics*, 91(3):483–487, 2000.

[37] Martin Lampe, Valeriy Gavrishchaka, Gurudas Ganguli, and Glenn Joyce. Effect of trapped ions on shielding of a charged spherical object in a plasma. *Physics Review Letters*, 86(23):5278–5281, 2001.

[38] Martin Lampe, Rajiv Goswami, Zoltan Sternovsky, Scott Robertson, Valeriy Gavrishchaka, Gurudas Ganguli, and Glenn Joyce. Trapped ion effect on shielding, current flow, and charging of a small object in a plasma. *Physics of Plasmas*, 10(5):1500–1513, 2003.

[39] S. Ratynskaia, S. Khrapak, A. Zobnin, M. H. Thoma, M. Kretschmer, A. Usachev, V. Yaroshenko, R. A. Quinn, G. E. Morfill, O. Petrov, and V. Fortov. Experimental determination of dust-particle charge in a discharge plasma at elevated pressures. *Physics Review Letters*, 93(8):085001, 2004.

[40] S. A. Khrapak, S. V. Ratynskaia, A. V. Zobnin, A. D. Usachev, V. V. Yaroshenko, M. H. Thoma, M. Kretschmer, H. Hofner, G. E. Morfill, O. F. Petrov, and V. E. Fortov. Particle charge in the bulk of gas discharges. *Physical Review E (Statistical, Nonlinear, and Soft Matter Physics)*, 72(1):016406–016415, 2005.

[41] S. A. Khrapak, G. E. Morfill, A. G. Khrapak, and L. G. D'yachkov. Charging properties of a dust grain in collisional plasmas. *Physics of Plasmas*, 13(5):052114–052118, 2006.

[42] L. G. D'yachkov, A. G. Khrapak, S. A. Khrapak, and G. E. Morfill. Model of grain charging in collisional plasmas accounting for collisionless layer. *Physics of Plasmas*, 14(4):042102–042107, 2007.

[43] Marco Gatti. Particle charging in ionized environments. Master's thesis, University of Minnesota, 2007.

[44] Andrey Bouchoule, editor. *Dusty Plasmas: Physics, Chemistry, and Technological Impact in Plasma Processing*. Wiley-New York, 1999.

[45] Robert N. Varney. Mean free paths, ion drift velocities, and the poisson distribution. *American Journal of Physics*, 39:534–538, May 1971.

[46] C. Bohm and J. Perrin. Spatially resolved optical emission and electrical properties of sih4 rf discharges at 13.56 mhz in a symmetric parallel-plate configuration. *Journal of Physics D: Applied Physics*, 24:865–881, 1991.

[47] Y.P. Raizer, M. N. Shneider, and N.A. Yatsenko. *Radio-Frequency Capacitive Discharges*. CRC Press, 1995.

[48] M.A. Lieberman and A.J. Lichtenberg. *Principles of Plasma Discharges and Materials Processing*. Wiley, 2005.

[49] M. Gatti and U. R. Kortshagen. Analytical model of particle charging in plasmas over a wide range of collisionality. *Physics review E*, 78:046402, 2008.

[50] P. Roca i Cabarrocas, P. Gay, and A. Hadjadj. Experimental evidence for nanoparticle deposition in continuous argon–silane plasmas: Effects of silicon nanoparticles on film properties. *J.Vac.Sci.Tech. A*, 14(2):655–659, 1996.

[51] Y. Ding, Y. Dong, A. Bapat, J.D. Nowak, C.B. Carter, U. Kortshagen, and S.A. Campbell. Single nanoparticle semiconductor devices. *IEEE Trans. Elect. Dev.*, 53(10):2525–2531, 2006.

[52] L. Mangolini, D. Jurbergs, E. Rogojina, and U. Kortshagen. Plasma synthesis and liquid-phase surface passivation of brightly luminescent si nanocrystals. *J.Lumin.*, 121(2):327 – 334, 2006.

[53] A. Bapat, M. Gatti, Y.-P. Ding, S.A. Campbell, and U. Kortshagen. A plasma process for the synthesis of cubic-shaped silicon nanocrystals for nanoelectronic devices. *J.Phys.D*, 40(8):2247–2257, 2007.

[54] L. Mangolini, D. Jurbergs, E. Rogojina, and U. Kortshagen. High efficiency photoluminescence from silicon nanocrystals prepared by plasma synthesis and organic surface passivation. *Phys.Stat. Sol. C*, 3(11):3975–3978, 2006.

[55] A.N.Goldstein. The melting of silicon nanocrystals: Submicron thin-film structures derived from nanocrystal precursors. *Applied Physics A*, 62:33–37, 1996.

[56] Makoto Hirasawa, Takaaki Orii, and Takafumi Seto. Size-dependent crystallization of si nanoparticles. *Applied Physics Letters*, 88(9):093119–093121, 2006.

[57] C M Ferreira and J Loureiro. Electron energy distributions and excitation rates in high-frequency argon discharges. *Journal of Physics D: Applied Physics*, 16(12):2471, 1983.

[58] U Kortshagen, N D Gibson, and J E Lawler. On the eh mode transition in rf inductive discharges. *J. Phys. D: Appl. Phys.*, 29:1224–1236, 1996.

[59] C. Courteille, C. Hollenstein, and J. Dorier et al. Particle agglomeration study in rf silane plasmas: In situ study by polarization-sensitive laser light scattering. *J. Appl. Phys.*, 80:2069–78, 1996.

[60] Y. Watanabe, M. Shiratani, H. Kawasaki, and et al. Growth processes of particles in high frequency silane plasmas. *Journal of Vacuum Science Technology A*, 14:540–5, 1996.

[61] Themis Matsoukas, Marc Russell, and Matthew Smith. Stochastic charge fluctuations in dusty plasmas. *J. Vac. Sci. Tech. A*, 14:624–630, 1996.

[62] Themis Matsoukas. The coagulation rate of charged aerosols in ionized gases. *Journal of Colloid and Interface Science*, 187:474 – 483, 1997.

[63] L Boufendi and A Bouchoule. Particle nucleation and growth in a low-pressure argon-silane discharge. *Plasma Sources Science and Technology*, 3:262, 1994.

[64] Fred Gelbard, Yoram Tambour, and John H. Seinfeld. Sectional representations for simulating aerosol dynamics. *Journal of Colloid and Interface Science*, 76:541–556, 1980.

[65] James D. Landgrebe and Sotiris E. Pratsinis. A discrete-sectional model for particulate production by gas-phase chemical reaction and aerosol coagulation in the free-molecular regime. *Journal of Colloid and Interface Science*, 139:63–86, 1990.

[66] K. W. Lee, H. Chen, and J. A. Gieske. *Aerosol. Sci. Technol.*, 3:53, 1984.

[67] David Jurbergs, Elena Rogojina, Lorenzo Mangolini, and Uwe Kortshagen. Silicon nanocrystals with ensemble quantum yields exceeding 60%. *Applied Physics Letters*, 88(23):233116–233118, 2006.

[68] R. Anthony and U. Kortshagen. Photoluminescence quantum yields of amorphous and crystalline silicon nanoparticles. *Phys. Rev. B*, 80(11):115407, 2009.

[69] S. A. Khrapak and G. E. Morfill. Grain surface temperature in noble gas discharges: Refined analytical model. *Physics of Plasmas*, 13(10):104506–104509, 2006.

[70] E.M. Lifshitz and L.P. Pitaevsky. *Physical Kinetics*. Pergamon, 1981.

[71] H.C.van de Hulst. *Light scattering by small particles*. Dover, 1957.

[72] J. E. Daugherty and D. B. Graves. Particulate temperature in radio frequency glow discharges. *39th National Symposium of the American Vacuum Society*, 11(4):1126–1131, 1993.

[73] Knudsen M. The molecular heat conductivity of gases and the accommodation coefficient. *Annalen der Physik*, pages 593–656, 1911.

[74] G. M. W. Kroesen H. Kersten, H. Deutsch. Charging of micro-particles in plasma-dust interaction. *International Journal of Mass Spectrometry*, 233(1-3):51–60, 2004.

[75] GHPM Swinkels, H Kersten, H Deutsch, and GMW Kroesen. Microcalorimetry of dust particles in a radio-frequency plasma. *Journal of Applied Physics*, 88(4):1747–1755, 2000.

[76] E Stoffels, W W Stoffels, H Kersten, G H P M Swinkels, and G M W Kroesen. Surface processes of dust particles in low pressure plasmas. *Physica Scripta*, T89:168–172, 2001.

[77] P. Roura, J. Farjas, A. Pinyol, and E. Bertran. The crystallization temperature of silicon nanoparticles. *Nanotechnology*, 18(17):175705–175708, 2007.

[78] A. Barnard and P. Zapol. A model for the phase stability of arbitrary nanoparticles as a function of size and shape. *J. Chem. Phys.*, 121:427683, 2004.

[79] Kumar Sinniah, Michael G. Sherman, Lisa B. Lewis, W. Henry Weinberg, Jr. John T. Yates, and Kenneth C. Janda. Hydrogen desorption from the monohydride phase on si(100). *The Journal of Chemical Physics*, 92(9):5700–5711, 1990.

[80] D. D. Koleske, S. M. Gates, and B. Jackson. Atomic h abstraction of surface h on si: An eley–rideal mechanism? *The Journal of Chemical Physics*, 101(4):3301–3309, 1994.

[81] Mayur S. Valipa and Dimitrios Maroudas. Atomistic analysis of the mechanism of hydrogen diffusion in plasma-deposited amorphous silicon thin films. *Applied Physics Letters*, 87(26):261911–261913, 2005.

[82] Braithwaite N.St, Booth J.P., and Cunge G. A novel electrostatic probe method for ion flux measurements. *Plasma Sources Science and Technology*, page 677, 1996.

[83] M. Ledinsky, A. Vetushka, J. Stuchlik, T. Mates, A. Fejfar, J. Kocka, and J. Stepanek. Crystallinity of the mixed phase silicon thin films by raman spectroscopy. *Journal of Non-Crystalline Solids*, 354:2253–2256, 2008.

[84] Y Watanabe. Formation and behaviour of nano/micro-particles in low pressure plasmas. *Journal of Physics D: Applied Physics*, 39(19):R329, 2006.

[85] Upendra Bhandarkar, Uwe Kortshagen, and Steven L Girshick. Numerical study of the effect of gas temperature on the time for onset of particle nucleation in argonsilane low-pressure plasmas. *Journal of Physics D: Applied Physics*, 36(12):1399, 2003.

[86] J Goree. Charging of particles in a plasma. *Plasma Sources Science and Technology*, 3(3):400, 1994.

[87] Themis Matsoukas and Marc Russell. Particle charging in low-pressure plasmas. *Journal of Applied Physics*, 77(9):4285–4292, 1995.

[88] H. R. Kaufman and J. M. E. Harper. Ion doses for low-energy ion-assist applications. *Journal of Vacuum Science Technology A: Vacuum, Surfaces, and Films*, 22(1):221–4, 2004.

[89] T. Takagi. Ion–surface interactions during thin film deposition. *Journal of Vacuum Science Technology A: Vacuum, Surfaces, and Films*, 2(2):382–8, 1984.

[90] S Shimizu, B M Annarone, T Shimizu, W Jacob, H Thomas, and G E Morfill. Environment with reduced ion bombardment energy for levitated particles in an rf plasma. *Plasma Sources Science Technology*, 17:035014, 2008.

[91] T. Shimizu, W. Jacob, H. Thomas, G. Morfill, T. Abe, Y. Watanabe, and N. Sato. Particle growth in hydrogen-methane plasmas. *Thin Solid Films*, 506-507:652–5, 2006.

[92] A H M Smets, W M M Kessels, and M C M van de Sanden. The effect of ion-surface and ion-bulk interactions during hydrogenated amorphous silicon deposition. *Journal of Applied Physics*, 102:073523, 2007.

[93] P M Gevers, J J H Gielis, H C W Beijerinck, M C M van de Sanden, and W M M Kessels. Amorphization of si(100) by ar+ ion bombardment studies with spectroscopic and time-resolved second-harmonic generation. *J. Vac. Sci. Technol. A*, 28:293–301, 2010.

[94] T.V. Herak, T.T. Chau, S.R. Mejia, P.K. Shufflebotham, J.J. Schellenberg, H.C. Card, K.C. Kao, and R.D. McLeod. Effects of substrate bias on structure and properties of a-si:h films deposited by ecr microwave plasmas. *Journal of Non Crystalline Solids*, 97-8:277–80, 1987.

[95] D B Graves and D H Humbird. Controlling surface in plasma processing: role of ions via molecular dynamics simulations of surface chemistry. *Plasma Sources Science Technology*, 11:A191–5, 2002.

[96] D B Graves and D H Humbird. Ion-induced damage and annealing of silicon. molecular dynamics simulations. *Pure Appl. Chem.*, 74:419–22, 2002.

[97] I. Popescu-Iovitzu and N. J. Ionescu-Pallas. On resonant charge transfer for positive ions. *Proc. Phys. Soc.*, 75:5, 1959.

[98] A. V. Phelps. Cross sections and swarm coefficients for nitrogen ions and neutrals in n2 and argon ions and neutrals in ar for energies from 0.1 ev to 10 kev. *.J. Phys. Chem. Ref. Data*, 20:557, 1990.

[99] U. Kortshagen, J. G. Parker, and J. E. Lawler. Comparison of monte carlo simulations and nonlocal calculations of the electron distribution function in a positive column plasma. *Phys. Rev. E*, 54:6746–61, 1996.

[100] L. Verlet. Computer experiments on classical fluids. i. thermodynamical properties of lennard-jones molecules. *Phys. Rev.*, 159:98, 1967.

[101] L. Verlet. Computer experiments on classical fluids. ii. equilibrium correlation functions. *Phys. Rev.*, 165:201–14, 1968.

[102] http://www.siglo-kinema.com/bolsig.htm.

[103] L. C. Pitchford, S. V. ONeil, and Jr J. R. Rumble. Extended boltzmann analysis of electron swarms expriments. *Physical Review A*, 23:294–304, 1981.

[104] P. J. Hargis Jr, K. E. Greenberg, P. A. Miller, J. B. Gerardo, J. R. Torczynski, M. E. Riley, G. A. Hebner, J. R. Roberts, J. K. Olthoff, J. R. Whetstone, R. J. Van Brunt, M. A. Sobolewski, H. M. Anderson, M. P. Splichal, J. L. Mock, P. Bletzinger, A. Garscadden, R. A. Gottscho, G. Selwyn, M. Dalvie, J. E. Heidenreich, Jeffery W. Butterbaugh, M. L. Brake, M. L. Passow, J. Pender, A. Lujan, M. E. Elta, D. B. Graves, H. H. Sawin, M. J. Kushner, J. T. Verdeyen, R. Horwath, and T. R. Turner. The gaseous electronics conference radio-frequency reference cell: A defined parallel-plate radio-frequency system for experimental and theoretical studies of plasma-processing discharges. *Review of Scientific Instruments*, 65:140–154, 1994.

[105] J-C Schauer, S Hong, and J Winter. Electrical measurements in dusty plasmas as a detection method for the early phase of particle formation. *Plasma Sources Science Technology*, 13:635–45, 2004.

[106] V A Godyak, R B Piejak, and B M Alexandrovich. Electrical characteristics of parallel-plate rf discharges in argon. *IEEE Tran. Plasma Sci.*, 16:660–76, 1991.

[107] U Kortshagen, H Schluter, and A Shivarova. Determination of electron energy distribution functions in surface wave produced plasmas. i. modelling. *Journal of Physics D: Applied Physics*, 24(9):1571–1584, 1991.

[108] Lafa Boufendi and Andr Bouchoule. Industrial developments of scientific insights in dusty plasmas. *Plasma Sources Science and Technology*, 11(3A):A211, 2002.

[109] Ch Hollenstein. The physics and chemistry of dusty plasmas. *Plasma Physics and Controlled Fusion*, 42(10):R93, 2000.

[110] M. Takai, T. Nishimoto, M. Kondo, and A. Matsuda. Effect of higher-silane formation on electron temperature in a silane glow-discharge plasma. *Appl. Phys. Lett.*, 77:2828, 2000.

[111] M. J. McCaughey and Mark J.Kushner. A model for particulate contaminated glow discharges. *Journal of Applied Physics*, 69:6952–61, 1991.

[112] I. Denysenko, M. Y. Yu, K. Ostrikov, and A. Smolyakov. Spatially averaged model of complex-plasma discharge with self-consistent electron energy distribution. *Phys. Rev. E*, 70(4):046403, 2004.

[113] G. I. Sukhinin, A. V. Fedoseev, S. N. Antipov, O. F. Petrov, and V. E. Fortov. Influence of dust particle concentration on plasma parameters in dc discharge. *Contrib. Plasma Phys.*, 49(10):781–785, 2009.

[114] S. A. Khrapak and G. E. Morfill. Dusty plasmas in a constant electric eld: Role of the electron drag force. *Phys. Rev. E*, 69:066411, 2004.

[115] U Kortshagen. Electron and ion distribution functions in rf and microwave plasmas. *Plasma Sources Science and Technology*, 4(2):172, 1995.

[116] http://jila.colorado.edu/~avp/collision_data/electronneutral/ELECTRON.TXT.